Title
Energy-Efficient Integrated Neural Interfaces for Retinal Prostheses

Permalink
https://escholarship.org/uc/item/7c53f10q

Author
Akinin, Abraham

Publication Date
2020

Peer reviewed|Thesis/dissertation

UNIVERSITY OF CALIFORNIA SAN DIEGO

Energy-Efficient Integrated Neural Interfaces for Retinal Prostheses

A dissertation submitted in partial satisfaction of the
requirements for the degree
Doctor of Philosophy

in

Bioengineering

by

Abraham Akinin

Committee in charge:

     Professor Gert Cauwenberghs, Chair
     Professor Todd P. Coleman
     Professor William R. Freeman
     Professor Vikash Gilja
     Professor Patrick P. Mercier
     Professor Gabriel A. Silva

2020

The dissertation of Abraham Akinin is approved, and it is acceptable in quality and form for publication on microfilm and electronically:

_____

_____

_____

_____

_____

Chair

University of California San Diego

2020

DEDICATION

To Wen, my loving wife.

You are my hope and inspiration.

EPIGRAPH

Life and death appeared to me ideal bounds, which I should first break through, and pour a

torrent of light into our dark world.

—Frankenstein *by Mary Shelley*

TABLE OF CONTENTS

LIST OF FIGURES

LIST OF TABLES

ACKNOWLEDGEMENTS

From their inception, research in the fields of electronics and the nervous system have been intricately linked. The *spark* that enables life has inspired discoveries inconceivable even to the author of Frankenstein: brain machine interfaces, sensory restoration, and the mechanisms of neural information storage and processing. I am fortunate to have met Professor Gert Cauwenberghs, my advisor, who has shared his passion for bioelectronics and allowed me to work on these exciting problems by building my own integrated circuits. So I can't thank him enough for working with me to devise a retina prosthesis which may one day bring light to many dark worlds. Without a doubt, he is the wisest, most patient, and most creative person I have ever met. His dedication and insight have helped me turn insurmountable challenges into beautifully flowing solutions. I have learned a great deal from his drive, positive attitude, and sense of humor. I hope to always treat those interested in learning as kindly as he has treated me.

I would also like to sincerely thank professor Patrick Mercier, whose invaluable advice, brilliant technical insight, and passion for teaching have become an enduring source of inspiration. I extend my gratitude to the other professors in my committee: Todd Coleman, William Freeman, Vikash Gilja, and Gabriel Silva. Their support and collaboration in many exciting projects at the frontiers of biomedical engineering are deeply valued.

My time at UCSD has been defined by amazing interactions with my colleagues. In particular, I would like to thank my mentors Chul Kim and Christoph Maier who

Alexander Williams, and Joshua Yang. I also appreciate the chance to reach myriad students by leading discussions, and office hours in the Principles of Bioinstrumentation Design course.

I commend Jan Lenington and Luis Palacios for their kind assistance in administrative and IT issues.

I am deeply thankful to all my colleagues at Nanovision Biosciences for their support and collaboration on the road to cure blindness: Dirk-Uwe Bartsch, Brandon Bosse, Sue Bauchner, Prof. Lingyun Cheng, Samir Damle, Kristyn Huffman, Sandy Rios, Yu-Hsin Liu, Prof. Yu-Hwa Lo, Prof. Nicholas Oesch, Hiren Thacker, Scott Thorogood, and Yi Jing.

I'm indebted to early influences who encouraged me and shared their excitement in science: Prof. Fotios Andreopoulos (my undergraduate research advisor), Prof. Michael Gaines (and the FGLSAMP), David Buncher, and Jose Pardo.

I can't forget to acknowledge here the indispensable role my friends outside the lab played in my life. They made the paradise that is San Diego, an even more amazing place. I especially want to thank Jason Caffrey, Eythan Familier, Evan Kriminger, Armando Lanzi, Michael Richter, Eugene Sato, Meir Shachar, and Kevin Vincent for their advise, commiseration, and technical sense of humor during the course of our PhDs.

I am truly blessed for my family and their zealous effort to educate and nurture me. I am thankful for my grandparents David (Z"L), Simi (Z"L), Abraham (Z"L), and Lucy whose stories and vast knowledge first made me marvel about the world. I greatly admire my adventurous, and enterprising brothers: David, Samuel, and Arie, who unrelentingly cared for me, called, and even traveled to visit me from the other side of the planet. I

appreciate my parents-in-law for their warmth and kindness. I would be nothing without the love of my wonderful parents, Reina and Ysaac. My mother armed me with the tools to succeed in life. My father transmitted his passion for problem solving (in quad ruled paper) and brought our family to this great country.

Finally, I am most grateful for my adoring wife Wen Li, to whom this thesis is dedicated. She supported me in every possible way while lovingly and selflessly encouraging all my dreams. I am deeply moved by her patience and understanding through all the sacrifices and dimmer periods of my research. In addition to all the happy moments we have shared together, I am thankful for our son Isaac Liang Akinin Li whose radiant smile and ceaseless wonder puts everything in perspective.

Samir Damle, Abraham Akinin, Yi Jing, Dirk-Uwe Bartsch, Lingyun Cheng, Nicholas Oesch, Yu-Hwa Lo, Gert Cauwenberghs, and William R. Freeman. "In vivo photovoltaic performance of a silicon nanowire photodiode–based retinal prosthesis." *Investigative ophthalmology & visual science* 59, no. 15 (2018): 5885-5892. The author is one of the primary authors and investigators of this work.

2010	B.S. in Biomedical Engineering, Physics, University of Miami
2017	M.S. in Bioengineering, University of California San Diego
2020	Ph.D. in Bioengineering, University of California San Diego

PUBLICATIONS

1. **Abraham Akinin**, Akshay Paul, Jun Wang, Alessio P. Buccino, and Gert Cauwenberghs. "Biopotential measurements and electrodes." *Neural Engineering*, Bin He, Ed., Springer. 2020 (*in print*).

2. Yasufumi Sakai, Bruno U Pedroni, Siddharth Joshi, Satoshi Tanabe, **Abraham Akinin**, and Gert Cauwenberghs. "Dropout and dropconnect for reliable neuromorphic inference under communication constraints in network connectivity." *IEEE Journal on Emerging and Selected Topics in Circuits and Systems (JETCAS)*, 9(4):658-667, 2019.

3. Akshay Paul, **Abraham Akinin**, Min S Lee, Matthew Kleffner, Stephen R Deiss, Gert Cauwenberghs. "Integrated In-Ear Device for Auditory Health Assessment" 2019 41st Annual International Conference of the IEEE Engineering in Medicine and Biology Society (EMBC):56-59, 2019.

4. Chul Kim, Jiwoong Park, Sohmyung Ha, **Abraham Akinin**, Rajkumar Kubendran, Patrick P Mercier, and Gert Cauwenberghs. "A 3 mm × 3 mm Fully Integrated Wireless Power Receiver and Neural Interface System-on-Chip." *IEEE Transactions on Biomedical Circuits and Systems (TBioCAS)*, 13(6):1736-1746, 2019.

5. Yasufumi Sakai, Bruno U Pedroni, Siddharth Joshi, **Abraham Akinin**, and Gert Cauwenberghs. "DropOut and DropConnect for reliable neuromorphic inference under energy and bandwidth constraints in network connectivity," *2019 IEEE International Conference on Artificial Intelligence Circuits and Systems (AICAS)*:76-80, 2019.

6. Brandon Bosse, Samir Damle, **Abraham Akinin**, Yi Jing, Dirk-Uwe Bartsch, Lingyun Cheng, Nicholas Oesch, Yu-Hwa Lo, Gert Cauwenberghs, and William R Freeman. "In vivo photovoltaic performance of a silicon nanowire photodiode–based retinal prosthesis." *Investigative ophthalmology & visual science*, 59(15):5885-5892, 2018.

7. Chul Kim, Gert Cauwenberghs, Patrick P Mercier, Sohmyung Ha, Jiwoong Park, and **Abraham Akinin**. "Resonant regulating rectifier with an integrated antenna." US Patent App. 15/736,239. 2018.

8. Sohmyung Ha, Gert Cauwenberghs, Chul Kim, Jiwoong Park, Patrick P Mercier, **Abraham Akinin**, Hui Wang, and Christoph H Maier. "Radio frequency powered adiabatic stimulation with energy replenishment." US Patent App. 15/736,252. 2018.

9. Jun Wang, Theodore Yu, **Abraham Akinin**, Gert Cauwenberghs, and Frédéric D Broccard. "Neuromorphic synapses with reconfigurable voltage-gated dynamics for biohybrid neural circuits." *2017 IEEE Biomedical Circuits and Systems Conference (BioCAS)*:1-4, 2017.

10. Jiwoong Park, Chul Kim, **Abraham Akinin**, Sohmyung Ha, Gert Cauwenberghs, and Patrick P Mercier."Wireless powering of mm-scale fully-on-chip neural interfaces." *2017 IEEE Biomedical Circuits and Systems Conference (BioCAS)*:1-4, 2017.

11. Jun Wang, Daniel Breen, **Abraham Akinin**, Frédéric Broccard, Henry DI Abarbanel, and Gert Cauwenberghs. "Assimilation of biophysical neuronal dynamics in neuromorphic VLSI." *IEEE Transactions on Biomedical Circuits and Systems (TBioCAS)*, 11(6):1258-1270, 2017.

12. Chul Kim, Sohmyung Ha, Jiwoong Park, **Abraham Akinin**, Patrick P Mercier, and Gert Cauwenberghs. "A 144-MHz fully integrated resonant regulating rectifier with hybrid pulse modulation for mm-sized implants." *IEEE Journal of Solid-State Circuits(JSSC)*, 52(11):3043-3055, 2017.

13. Chul Kim, Sohmyung Ha, **Abraham Akinin**, Jiwoong Park, Rajkumar Kubendran, Hui Wang, Patrick P Mercier, and Gert Cauwenberghs. "Design of miniaturized wireless power receivers for mm-sized implants" *2017 IEEE Custom Integrated Circuits Conference (CICC)*:1-8, 2017.

14. Brandon Bosse, Samir Damle, **Abraham Akinin**, Dirk-Uwe G Bartsch, Lingyun Cheng, Yi Jing, and William R Freeman. "In vivo acute and chronic evaluation of a nanowire based subretinal prosthesis." *Investigative Ophthalmology & Visual Science*,58(8):4191-4191, 2017.

15. Jun Wang, Daniel Breen, **Abraham Akinin**, Henry DI Abarbanel, and Gert Cauwenberghs. "Data assimilation of membrane dynamics and channel kinetics with a neuromorphic integrated circuit." *2016 IEEE Biomedical Circuits and Systems Conference (BioCAS)*:584-587, 2016.

16. Chul Kim, Jiwoong Park, **Abraham Akinin**, Sohmyung Ha, Rajkumar Kubendran, Hui Wang, Patrick P Mercier, and Gert Cauwenberghs. "A fully integrated 144 MHz wireless-power-receiver-on-chip with an adaptive buck-boost regulating rectifier and low-loss h-tree signal distribution." *2016 IEEE Symposium on VLSI Circuits (VLSI-Circuits)*:1-2, 2016.

17. Sohmyung Ha, Massoud L Khraiche, **Abraham Akinin**, Yi Jing, Samir Damle, Yanjing Kuang, Sue Bauchner, Yu-Hwa Lo, William R Freeman, Gabriel A Silva, and Gert Cauwenberghs."Towards high-resolution retinal prostheses with direct optical addressing and inductive telemetry."*Journal of Neural Engineering(JNE)*, 13(5):056008, 2016.

18. Sohmyung Ha, **Abraham Akinin**, Jiwoong Park, Chul Kim, Hui Wang, Christoph Maier, Patrick P Mercier, and Gert Cauwenberghs."Silicon-integrated high-density electrocortical interfaces." *Proceedings of the IEEE*, 105(1):11-33, 2016.

19. Chul Kim, Sohmyung Ha, Jiwoong Park, **Abraham Akinin**, Patrick P Mercier, and Gert Cauwenberghs. "A 144MHz integrated resonant regulating rectifier with hybrid pulse modulation." *2015 Symposium on VLSI Circuits (VLSI Circuits)*:C284-C285, 2015.

20. Sohmyung Ha, **Abraham Akinin**, Jiwoong Park, Chul Kim, Hui Wang, Christoph Maier, Gert Cauwenberghs, and Patrick P Mercier. "A 16-channel wireless neural interfacing SoC with RF-powered energy-replenishing adiabatic stimulation." *2015 Symposium on VLSI Circuits (VLSI Circuits)*:C106-C107, 2015.

21. Chul Kim, Siddharth Joshi, Chris Thomas, Sohmyung Ha, **Abraham Akinin**, Lawrence Larson, and Gert Cauwenberghs. "A CMOS 4-channel MIMO baseband receiver with 65dB harmonic rejection over 48MHz and 50dB spatial signal separation over 3MHz at 1.3 mW."*2015 Symposium on VLSI Circuits (VLSI Circuits)*:C304-C305, 2015.

22. **Abraham Akinin**, Nikhil Govil, Howard Poizner, and Gert Cauwenberghs. "Frequency domain identification of proprioceptive evoked potentials in compliant kinematic experiments" *2015 7th International IEEE/EMBS Conference on Neural Engineering (NER)*:807-811, 2015.

23. **Abraham Akinin**, Joshua Yang, Alexander Williams, Andrew Lee, Pedram Pourhosseini, Arnost Fronek, and Gert Cauwenberghs. "Continuous wave ultrasonic Doppler tonometry."*2014 IEEE Biomedical Circuits and Systems Conference (BioCAS)* 2014.

24. Masayoshi Furukawa, Shigeo Wada, Akinori Ueno, **Abraham Akinin**, and Gert Cauwenberghs. "High gamma band activity in noninvasively measured EEG preceding anti-saccade initiation" *2014 IEEE International Symposium on Medical Measurements and Applications (MeMeA)*:1-5, 2014.

25. Sohmyung Ha, Chul Kim, Yu M Chi, **Abraham Akinin**, Christoph Maier, Akinori Ueno, and Gert Cauwenberghs. "Integrated circuits and electrode interfaces for noninvasive physiological monitoring", *IEEE Transactions on Biomedical Engineering(TBME)*, 61(5):1522-1537, 2014.

26. Massoud Khraice, Sharif El Emam, **Abraham Akinin**, Gert Cauwenberghs, William Freeman, and Gabriel A Silva. "Visual evoked potential characterization of rabbit animal model for retinal prosthesis research." *2013 35th Annual International Conference of the IEEE Engineering in Medicine and Biology Society (EMBC)*:3539-3542, 2013.

27. Nikhil Govil, **Abraham Akinin**, Samuel Ward, Joseph Snider, Markus Plank, Gert Cauwenberghs, and Howard Poizner. "The role of proprioceptive feedback in parkinsonian resting tremor." *2013 35th Annual International Conference of the IEEE Engineering in Medicine and Biology Society (EMBC)*:4969-4972, 2013.

ABSTRACT OF THE DISSERTATION

Energy-Efficient Integrated Neural Interfaces for Retinal Prostheses

by

Abraham Akinin

Doctor of Philosophy in Bioengineering

University of California San Diego, 2020

Professor Gert Cauwenberghs, Chair

Advances in neural engineering are enabling targeted neural recording and stimulation towards high-resolution brain computer interfaces. High-throughput bidirectional communication to the brain is paramount to reach translational impact with neural prostheses. Useful vision restoration through microelectronic retinal prosthesis implants continues to be a difficult challenge despite commendable attempts. Achieving practical control of thousands and millions of electrode channels calls for architectural advances to improve the scalability of biopotential recording, power, wireless communications, and biocompatible in-

terconnect. This dissertation presents an interdisciplinary approach towards high-resolution retinal prostheses that overcomes these challenges. The requirements and interactions between biopotential recording circuits and electrodes are formulated in the context of neural recording. Next, a resonant inductive power transfer link for retinal prostheses is designed and validated. The effect of ocular movements on the efficiency of power transfer is demonstrated in a constructed phantom frame. Subsequently, a novel integrated circuit is designed and fabricated to provide highly energy-efficient power delivery and waveform control to drive a nanowire-based microphotodiode subretinal electrode array. Energy efficiency and scalability of the power and communication link is accomplished through external control over global stimulation waveform parameters. Efficiency improvements derive from two main approaches: adiabatic unregulated power delivery to the stimulator, and duty cycling of the external transmitter. Global charge metering and calibration minimize the required data transmission and system operating frequency for bidirectional communication and charge-balanced stimulation. The dissertation concludes with *in vivo* validation of the nanowire microelectrode array transducer in rabbits using the principle of synchronous detection of cerebral cortex visual evoked biopotential signals. The various components of this dissertation present a *full-stack* development of a system to remediate blindness and advance the field of neural interfaces.

Chapter 1

Outline

This dissertation focuses on the design, implementation, and validation of closed-loop neural interfaces toward high resolution retinal prostheses. To this end, we explore novel developments in neural recording, neural stimulation, inductive wireless power and data transmission, as well as *in vivo* neuroscience methodology for validating sensory restoration. The interdisciplinary nature of *neural interface and neural prostheses* present several major challenges that can only be overcome through a concerted effort engaging design engineers, electrophysiologists, and clinical practitioners. A brief outline of the dissertation, describing the contributions of each chapter, follows below.

Chapter 2 presents an overview of the general setting of the dissertation, reviewing biopotentials, measurement systems and electrodes in the field of neural engineering. Neural biopotentials are electrical signals generated by the cells of the nervous system. Recording and monitoring the aggregate or individual behavior of neurons yields information about the brain and the peripheral nervous system frequently used in clinical and research settings.

Many different modalities of recording neural biopotentials have been developed.

Chapter 3 discusses the design and validation of a wireless power system for the retinal prosthesis implant that is the main subject of the dissertation. Inductive wireless power transfer empowers microelectronic systems to be implanted in spatially constrained anatomic areas. Due to the need to deliver therapeutic or diagnostic function to sensitive areas, such as the eye, batteries become impractical for reasons of thermal and mechanical safety. In this paper we discuss the requirements and optimization techniques to power an intraocular implant through an inductive coil in the surface of the eye. We design and characterize transmitting and receiving inductive coils. Subsequently, through the use of a custom 3D printed mechanical test frame, we characterize the power transfer efficiency at the appropriate geometric parameters. Furthermore, the effect of misalignment, axial displacement, and rotation due to saccadic movements is quantified in air and through a fragment of animal tissue.

Chapter 4 presents a highly energy-efficient wireless stimulator integrated circuit that provides full functionality of power delivery and waveform control for the retinal prosthesis implant, interfacing with a subretinal microphotodiode transducer. We overcome the traditional limitations of excessive power consumption and bulky unscalable multichannel transocular cables through global voltage biasing of an optically-modulated nanowire-based microelectrode array. Several power saving strategies: adiabatic control of the implantable system's power supply, outsourcing auxiliary functions to the external system, and duty cycling the transmitter are implemented. Circuits are optimized to operate at wide supply range (0.5-3.3V) to avoid power conversion losses. Bidirectional telemetry and power are

transmitted over a single inductive link to control pulse timing and charge balance of the stimulator. The biphasic stimulator implements charge metering with a series capacitor as well as additional calibration phases to account for link uncertainty during eye rotations.

Chapter 5 describes *in vivo* validation of the subretinal microphotodiode transducer, demonstrating retinal prosthesis functionality through illumination induced, electrically evoked potentials in visual cortex. This study was conducted to evaluate the efficacy of optically driving the subretinal prosthesis to produce visual cortex activation via electrical stimulation of the retina. We measured electrically evoked potential responses (EEPs) in rabbit visual cortex in response to illumination of the subretinal nanowire prosthesis with pulsed 852 nm infrared light. We compared the EEP responses to visually evoked potential responses (VEPs) to pulsed 532 nm visible light (positive control) and pulsed 852 nm infrared light (negative control). Activating the devices with IR light produced EEP responses with a significantly higher trough-to-peak amplitude (54.17 ± 33.4 μV) than infrared (IR) light alone (24.07 ± 22.1 μV) or background cortical activity (23.22 ± 17.2 μV). EEP latencies were significantly faster than focal VEP latencies. Focal VEPs produced significantly higher amplitudes ($94.88 \pm 43.3\mu$V) than EEPs. We also demonstrated how an electrode placed on the cornea can be used as a non-invasive method to monitor the function of the implant. These results show that subretinal electrical stimulation with nanowire electrodes can elicit electrically evoked potentials in the visual cortex, providing evidence for the viability of a subretinal nanowire prosthetic approach for vision restoration.

Chapter 6 concludes by summarizing the developments toward improvements in neural interfaces and retinal prostheses, including an outlook on future developments.

Chapter 2

Biopotential Measurements and Electrodes

2.1   Background

The ionic currents that traverse the cell membrane of neurons give rise to biopotentials. These electrical signals can be recorded with specialized instrumentation in order to assess physiological function, conduct neuroscience research, and even provide a novel medium of communication through brain-computer interfaces (BCI). Biopotentials can be recorded from different locations in the body, according to the organ or system targetted for examination. Fig. 2.1 shows the location of various signals of interest to neural engineering.

Aside from the diversity of locations and anatomical structures that can be recorded, these signals also vary significantly in their spatiotemporal properties. Spatial resolution is generally dependent on the distance between the electrodes and the target measurement

ExG	Electrographic Modality	Measurement Target
EEG	Electroencephalography	Brain
ERG	Electroretinography	Retina
EMG	Electromyography	Skelletal Muscle
ENG	Electroneurography	Peripheral Nerve
EGG	Electrogastrography	Stomach & Intestines
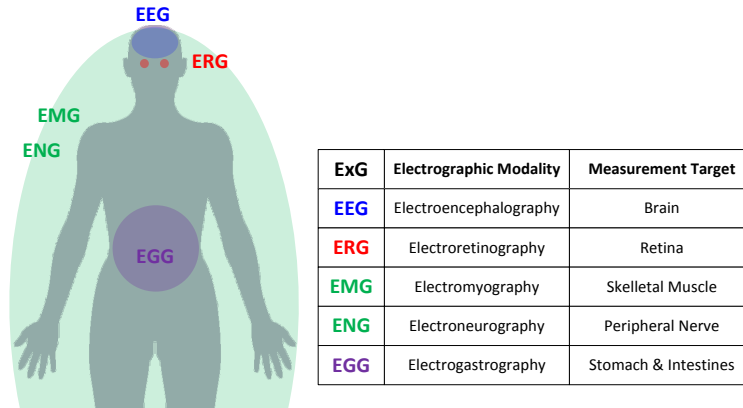
Figure 2.1: Anatomical regions of sources of biopotentials of various modalities measured in neural engineering.

source, as well as the spatial diversity of average electrical activity in the electrode's vicinity. Electroencephalography (EEG), which registers the collective dynamics of neuronal activity over large regions in the brain as electrical fields through volume conduction in extracellular space, is generally measured on and around the scalp with electrode arrays that exceed 1 cm pitch. At these distances, biopotential signals from the brain have a bandwidth below 100 Hz. Electrocorticography (ECoG) is a related modality to EEG which measures these brain biopotentials directly on the surface of the cerebral cortex. Although it is surgically invasive, the decreased distance from the neural sources allows ECoG to distinguish faster and smaller nuclei of brain activity, at higher spatial and temporal resolutions. Currently in translational development, microelectrocortigography (μECoG) records brain biopotentials with sub-millimeter pitch, high density electrode arrays. At these even smaller distances, μECoG can resolve even smaller and faster brain signals. The downside to decreasing the spacing of the electrodes in order to fit more channels, is increased difficulty in covering large areas of the brain.
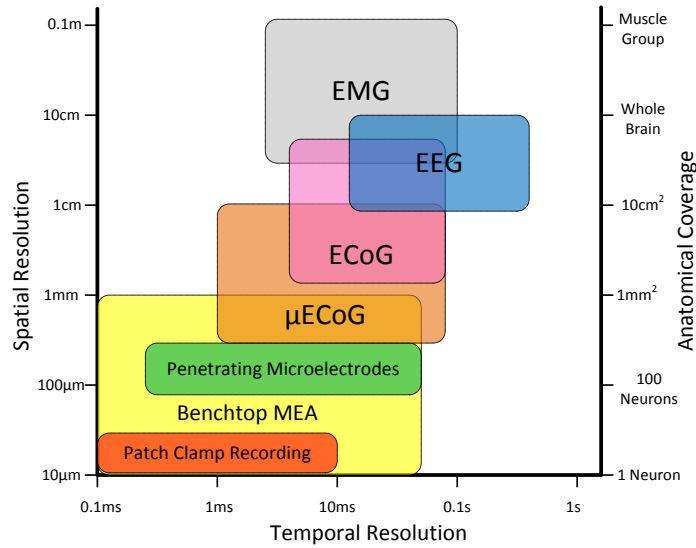
Figure 2.2: Spatiotemporal characteristics of neural biopotential signals

Following this trend towards finer, cellular-scale resolution, electrode arrays can be placed on the cortex with penetrating shanks that minimize the distance to cortical neurons. A complementary realm of neural engineering pursues *in vitro* studies using benchtop experimental setups with brain slices or neural cultures measuring electrical potentials at and below cellular scale through fine-pitch multielectrode arrays (MEAs). Further, intracellular potentials can be recorded through glass pipette patch clamp electrodes inserted through the cell membrane. Fig. 2.2 compares the scale, coverage, and temporal resolution of these modalities. Ranging from whole-body recordings of electromyography (EMG), measuring the activation of whole muscle groups, to sub-cellular patch clamp recordings of single-unit activity, biopotential signals span many orders of magnitude in spatial and temporal scale and thus require diverse specialized instrumentation.

The design methodology for a successful medical neuroengineering device is tightly coupled to a set of well defined design objectives. For example, the device may require monitoring the brain of a patient with epilepsy, during surgery, through a flexible electrode array to localize a seizure inducing nucleus. Once the objectives in the application setting are clearly defined, it becomes relatively straightforward to determine the specific engineering requirements. A system-level description can usually be formulated with a block diagram describing the major components required towards realization in hardware. Fig. 2.3 shows an example block diagram of a typical neural instrument. Neural biopotentials are sensed through a specialized electrode and an analog front-end (AFE), which contains amplifiers and analog signal processing circuits conditioning the signal for subsequent digitization by an analog-to-digital converter (ADC). Digital signal processing (DSP) may then be used to further condition the signal, or extract relevant physiological information. The digital output data stream can then be logged for local storage or wirelessly transmitted for further external processing. Other relevant and indispensable blocks include power management including possible provisions for power harvesting directly from environmental sources such as RF incident power and body heat.

Increasingly, neural instruments include neurofeedback capabilities, in which the signals obtained from the sensors are locally processed to modulate neural activity and function. As such, the instrument will apply electrical or other modulatory signals to biological tissue in order to restore lost function, or prevent a pathological condition. When a medical device applies electrical excitation, or neuromodulation, depending on information derived from recorded biopotentials it is known as a closed-loop neuroprosthesis.
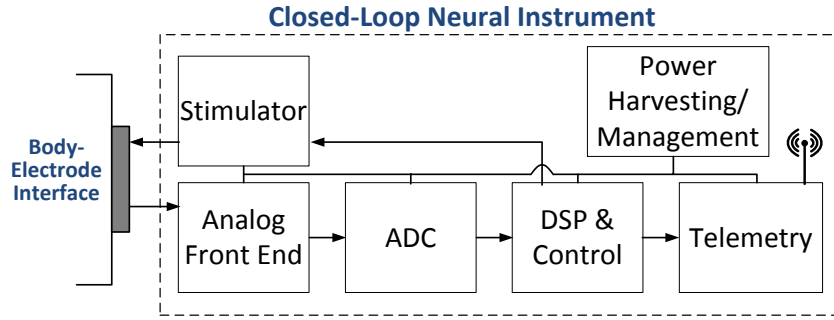
Figure 2.3: Generic block diagram of a wireless closed-loop neural instrument that performs biopotential recording and stimulation of electrically active tissue.

Having determined a system architecture it becomes possible to consider the specific requirements of the component subsystems. In this chapter we will consider the electrode and AFE requirements while keeping in mind their effect on the rest of the system.

2.2   Electrodes for Neural Interfaces

An electrode is a component of an electrical circuit that interfaces with non-metallic media. They are the primary component in a biopotential recording or stimulation instrument. In a recording application, the electrode couples galvanically to capture the local field potential. In a stimulating application, the electrode sources current through ionic transport to affect the local electric fields. Given their roles, the dimensions, geometry, and composition are of utmost importance to design requirements. Signal degradation due to inferior electrode design or placement is unlikely to be ameliorated by design improvements in blocks further down the signal chain. In this section we discuss the properties and models of electrodes as they relate to biopotential measurement and current stimulation.

2.2.1 Electrode Properties and Modeling

It is conceptually helpful to consider the behavior of an electrode by representing its electrochemical function as an ensemble of classical lumped circuit elements. Through this abstraction we may determine how they affect the signal as it transduces onto the measurement circuit. Standard linear circuit and signal analysis techniques can then be used for experimental characterization of an electrode, including its polarization properties as a function of the material, and its impedance and noise properties as a function of frequency.

2.2.1.1 Electrode-Electrolyte Double-Layer Interface

The electrode-electrolyte interface serves as an intermediary between the electronic charge transport in metallic conductors, and the ionic charge transport in the aqueous medium of the electrolyte. On the electrolyte side, a double layer of ions forms in response to a buildup of electrical potential. The first layer is composed of ions that are chemically *adsorbed* onto the electrode surface while the following layer has free ions electrostatically attracted to the surface charge. This looser second layer is also influenced by thermal motion in the solution, and as such is known as the *diffuse layer*. Fig. 2.4 shows two main electrode-electrolyte models using lumped elements. Although more refined models exist that take into account more detailed physics of double layers, these two examples suffice to explain the general behavior of electrodes.

2.2.1.2 Impedance

Two main types of electrodes can be distinguished, based on their intrinsic impedance properties.

Polarizable, non-Faradaic electrodes have a mostly capacitive interface to the electrolyte as shown in Fig. 2.4(a). Here C_H denotes the surface charge, or the *Helmholtz layer*. As this capacitor is in series with the rest of the circuit it blocks the flow of DC currents. In series, the diffuse layer behaves as a parallel capacitance and resistance pair. The capacitance C_D is related to the how much charge can be accumulated in the diffuse layer, and the resistance R_D to the work required by the ions to move through the solution. Further, the bulk of the solution also presents a series resistance R_S, dependent on geometry, size, and distance of the electrodes.

Non-polarizable, Faradaic electrodes permit charge to flow from electronic currents in the metallic section of the circuit, to ionic currents throughout the solution. Charge transfer between electrons and ions occurs as part of the chemical processes of reduction and oxidation. An example of a non-polarizable electrode widely used for non-invasive electrophysiology directly over the skin is the Ag/AgCl (silver/silver chloride) electrode, in which a layer of silver chloride over the silver bulk of the electrode provides a buffer for direct charge transfer through redox-based one-to-one exchange of electrons on the electrode side, and chloride ions (Cl^-) on the electrolyte side of the AgCl layer. In Fig. 2.4(b) the entire double layer capacitance is represented by C_d, while dissipative

elements R_{ct} and Z_W occur in parallel. R_{ct} is the *charge transfer resistance* and it relates to the kinetics of redox reactions at the electrode surface. Z_W is the *Warburg impedance* which is a constant phase element (with phase $+45°$) is related to the frequency dependent diffusion of charged particles in the solution. In Faradaic electrodes, we must also consider the contribution from the bulk of the solution separating electrodes from each other.

2.2.1.3 Half-Cell Potential

As the result of the exchange between ionic and electronic charge at the electrode-electrolyte interface through the electrochemical redox (reduction-oxidation) reactions at thermal equilibrium, complementary charge builds up on both sides of the interface. This space charge gives rise to a potential difference, termed the half-cell potential, which is specific to the metallic element in the electrode being reduced to its ionic equivalent in the electrolyte (e.g., Ag and Ag^+). In an electrochemical cell, the overall potential between electrodes in a shared electrolyte medium is the total potential resulting as the difference between two half-cell potentials. Hence for accurate and reproducible biopotential measurement it is advisable to use the same electrode type for both the signal and the reference electrodes, eliminating an important source of electrode voltage offset.

2.2.1.4 Noise

Thermal noise as stochastic fluctuations in ion transport naturally arise from random-walk interactions between the various electrochemical compounds at thermal equilibrium. The square magnitude of thermal voltage noise in the electrode is proportional

to temperature, electrode resistance, and spectral bandwidth: $\overline{v_n^2} = 4kTR\Delta f$. Other important source of noise include $1/f$ noise, with square magnitude inversely proportional to frequency, primarily due to random fluctuations in mass transport at the electrical double layer [47].

2.2.1.5 Water Window and Current Transfer Capacity

An important consideration in the electrode voltage range for electrodes used in electrical stimulation is the electrolysis breakdown of water molecules into oxygen and hydrogen gas above a critical voltage threshold, which depends on the electrode material. These gases as byproducts of the electrolysis are detrimental to tissue survival and electrode longevity. To avoid water breakdown, voltage limiters are usually included in the control circuits driving the electrodes. The water window puts a practical limit on the specific current transfer capacity of a given electrode depending on geometry, surface roughness, and material [21].

2.2.2 Volume Conduction for Electrical Recording and Stimulation

The electric potentials induced by neural activity and recorded by an electrode in the extracellular space, or generated by the electrodes when used for stimulation can be, in a first approximation, modeled analytically using *volume conduction theory* [82]. Considering a quasistatic approximation of Maxwell's equations and assuming a conductive, isotropic, homogeneous, linear, and infinite medium, the electric potential ϕ_{ex} (*ex* stands
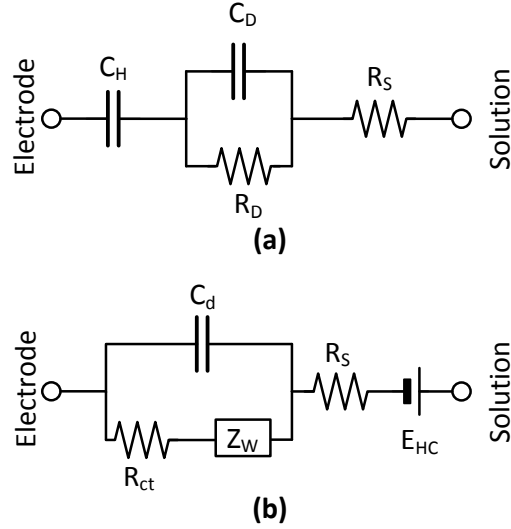
Figure 2.4: Lumped-element circuit model of the electrode-electrolyte interface. (a) Polarizable, non-Faradaic electrode. (b) Non-polarizable, Faradaic electrode.

for *extracellular*) generated by a point current source $I_s(t)$ (monopolar current source) at a position r_s can be computed at any point r (except for r_s) as [62]:

$$\phi_{ex}(\boldsymbol{r}, t) = \frac{I_s(t)}{4\pi\sigma \mid \boldsymbol{r} - \boldsymbol{r_s} \mid} \tag{2.1}$$

where σ is the conductivity of the medium, and the ground reference ($\phi_{ex} = 0$) is assumed *far away* from the current. The extracellular conductivity of neural tissue is typically in the order of 0.3 S/m, but this varies depending on brain regions *in vivo*, or in slice or culture conditions *in vitro*. Importantly, Eq. 2.1 applies both to modeling the electric potential measured on the electrodes due to currents emanating from electrically active cells for recording, and to modeling the effect of stimulating currents from the electrodes on extracellular fields surrounding the cells.

When neurons are active, ionic currents flow in and out of their membranes. The dynamics of a neuron can be computed using the *cable equation* [50,95]. From the solution of this equation, one can calculate the *transmembrane* currents of different parts of the neuron. Owing to the linear nature of volume conduction in the extracellular medium, the electric potential generated by each of these currents $I_i(t)$ is simply summed to arrive at the electric potential at an electrode location $\boldsymbol{r_e}$ (Fig. 2.5 (a)):

$$\phi_{ex}(\boldsymbol{r_e}, t) = \frac{1}{4\pi\sigma} \sum_i \frac{I_i(t)}{|\boldsymbol{r_e} - \boldsymbol{r_i}|}. \tag{2.2}$$

In the general case of bipolar recording, where a second electrode at position $\boldsymbol{r_{ref}}$ is used rather than a distant electrode for the reference, the differential potential between the electrodes becomes:

$$\phi_{diff} = \phi_{ex}(\boldsymbol{r_e}, t) - \phi_{ex}(\boldsymbol{r_{ref}}, t) = \frac{1}{4\pi\sigma} \sum_i \left[\frac{I_i(t)}{|\boldsymbol{r_e} - \boldsymbol{r_i}|} - \frac{I_i(t)}{|\boldsymbol{r_{ref}} - \boldsymbol{r_i}|} \right]. \tag{2.3}$$

Conversely, the electrical potential that arises from electrical stimulation is derived from Eq. 2.1 by considering an electrode at position r_e with a stimulating current I_e. The extracellular potential at position r reads (Fig. 2.5 (b)):

$$\phi_{ex}(\boldsymbol{r}, t) = \frac{I_e(t)}{4\pi\sigma \, |\boldsymbol{r} - \boldsymbol{r_e}|}. \tag{2.4}$$

Stimulating currents can be also applied in a bipolar fashion to increase the selectivity of stimulation. If two electrodes are used to deliver opposing currents, then they make up a *dipolar* current source. Considering the positive current source $+I_e$ at position $\boldsymbol{r_+}$ and the negative source $-I_e$ at position $\boldsymbol{r_-}$, we can define the current dipole moment $\boldsymbol{p}$ as [43,82]:

$$\boldsymbol{p} = I_e(\boldsymbol{r_+} - \boldsymbol{r_-}) = I_e\boldsymbol{d} \tag{2.5}$$

14
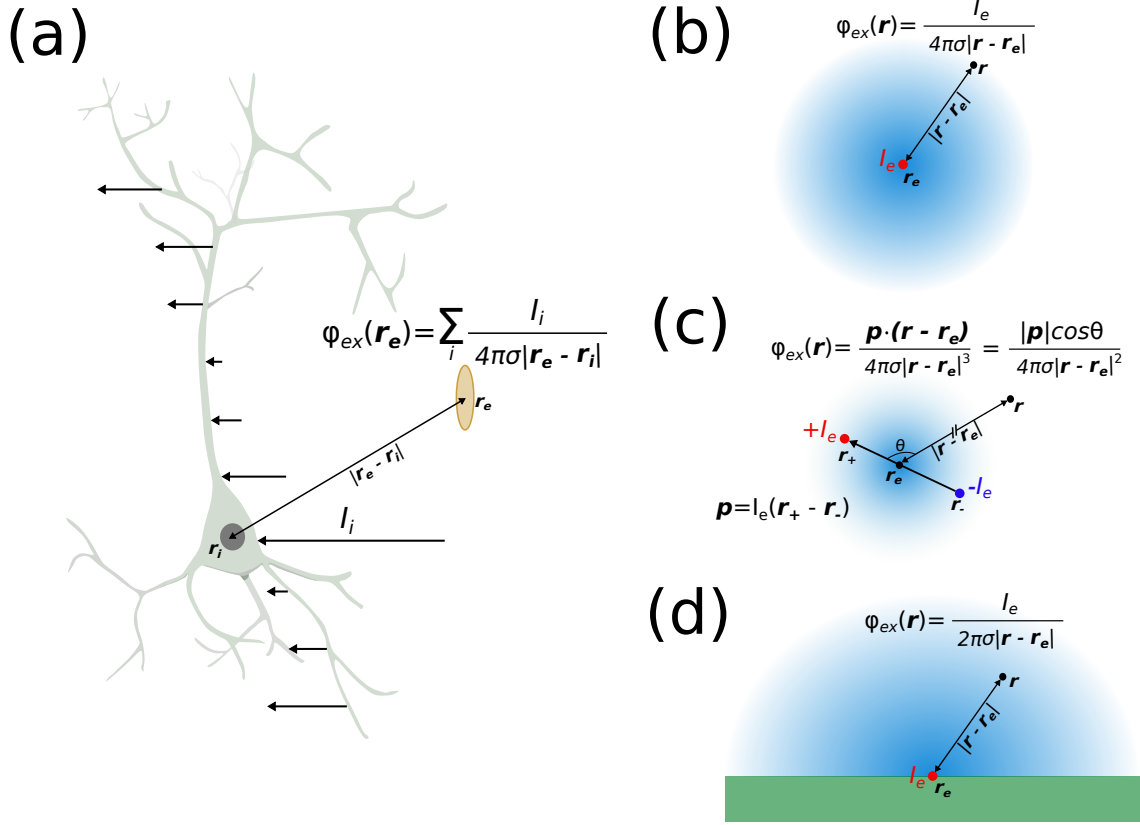
Figure 2.5: (a) Modeling electric potential generated by a neuron. The contribution of transmembrane currents of the neuron are summed at the electrode location [18]. (b) Modeling electric potential from a monopolar current source. (c) Modeling electric potential from a dipolar current source. (d) Modeling electric potential from a stimulating current of a planar device using the *Method of Images* [79].

where $\boldsymbol{d}$ is the vector between the positive and the negative current locations. Defining the middle point of this vector as $\boldsymbol{r_e}$ (Fig. 2.5 (c)), the extracellular potential generated by the current dipole can be approximated as:

$$\phi_{ex}(\boldsymbol{r}, t) \approx \frac{\boldsymbol{p}(t)(\boldsymbol{r} - \boldsymbol{r_e})}{4\pi\sigma \mid \boldsymbol{r} - \boldsymbol{r_e} \mid^3} = \frac{I_e(t)\, d\, cos(\theta)}{4\pi\sigma \mid \boldsymbol{r} - \boldsymbol{r_e} \mid^2} \tag{2.6}$$

where we defined d as the distance between the current sources and θ as the angle between $\boldsymbol{p}$ and $(\boldsymbol{r} - \boldsymbol{r_e})$. This approximation is valid when the distance $\mid \boldsymbol{r} - \boldsymbol{r_e} \mid$ is substantially

more than $3d$ [82]. For closer distances, the two currents should be summed separately as two opposing monopolar sources.

So far we have assumed that the medium surrounding the electrodes is homogeneous and isotropic, but these assumptions are not usually fully satisfied. Considering, for example, microelectrode arrays for *in vitro* recording [5, 32], one can clearly observe that the assumption of homogeneity is not satisfied, as cell cultures or brain slices are mounted *on top* of the electrodes plane. In this case, the potential generated by a monopolar current source is obtained directly by the *Method of Images* (MoI - Fig. 2.5 (d)) [79]:

$$\phi_{ex}(\boldsymbol{r}, t) = \frac{I_e(t)}{2\pi\sigma \mid \boldsymbol{r} - \boldsymbol{r_e} \mid} \tag{2.7}$$

Eq. 2.7 differs from Eq. 2.1 only in the scalar that multiplies the denominator, making the potential twice as large in the latter case, as current can only flow in the semi-space facing the electrode plane. The MoI can also be extended to account for several plane interfaces with different conductivities, for example a brain slice mounted on a micro-electrode array and placed in a saline solution, or an epidural ECoG electrode facing the dura mater, the arachnoid, the CSF, and subsequently the pia and cortical tissue (see Fig. 2.9 (b)).

So far we have also considered the electrode as a single point in space ($\boldsymbol{r_e}$). However, electrodes are not points and they have a finite size. A simple way to include the spatial extent of the electrode in the calculation of the electric field generated by a current is called the *disk approximation* [62]. Considering for example an electrode injecting a current $I_e(t)$ in the tissue, one can randomly draw N points belonging to the electrode surface (r_{e_i}) and and split the stimulating current into small contributions (owing to the linearity

assumption). The electric potentials can then be approximated as:

$$\phi_{ex}(\boldsymbol{r}, t) = \sum_{e=1}^{N} \frac{I_e(t)/N}{2\pi\sigma \mid \boldsymbol{r} - \boldsymbol{r_{e_i}} \mid}. \tag{2.8}$$

The same approach can be used when computing the electric potential generated by neural activity at the electrode locations.

The above-described formulations rely on several assumptions. First of all the conductivity of the medium is assumed to be scalar, hence neglecting capacitive properties of the tissue. This assumptions seems however to be well justified for relevant frequencies in extracellular recordings [62, 82].

Second, the medium is assumed to be isotropic, but this assumption is harder to relax. In the neural tissue, in fact, the presence of oriented pyramidal cells makes conductivity anisotropic [35]. Anisotropy in the tissue can be accounted for with analytical solutions [43, 79].

Finally, the extracellular milieu is assumed to be homogeneous (without discontinuities) and infinite. This is clearly a stronger assumption, considering that in order to measure the electric potentials generated by the neurons, we insert a probe in their vicinity. As mentioned above, for planar electrode arrays one can use the *Method of Images*. For more complicated cases, numerical solutions, such as finite element methods (FEM), can be used. FEM approaches are popular to predict the response of stimulation in the spinal cord [12, 69] or to study the effect of complex probe geometries [11].

2.3 Circuit Techniques for Neural Interfaces

Electrical circuit theory provides a useful tool to evaluate and design the systems that acquire and transduce biopotential signals. Once the characteristics of the biopotential signal are understood and the intended acquisition precision is determined, the requirements for the electrode, AFE, ADC, and DSP can be derived. Although the electrode is the first component in the signal path, and is of critical importance, system design is not generally focused on optimizing electrode geometry and composition. Custom electrode design and optimization require access to specialized fabrication tools and facilities, and the design itself is largely constrained by the available geometry of the physiological recording space. In contrast, AFE design has many more design parameters that can be adjusted and specialized tools for simulation.

2.3.1 Analog Front Ends

Biopotential signals vary in their characteristics across the neuroengineering modalities of interest. Fig. 2.2 details the spatiotemporal resolution of different neural interfaces. Additionally, we may also consider the amplitude of these signals to vary, as electrodes are located a finite distance away from biopotential sources and average all surrounding electrical activity. It thus becomes a crucial part of the system's design, to use an AFE that is appropriate to the signal characteristics. The role of the AFE is to amplify the very small biopotential signals with low noise generation, while filtering out interference and other irrelevant signals.

2.3.1.1   Operational Amplifiers

Operational Amplifiers (opamps) are high-gain active circuits that can amplify the voltage difference between two input terminals. When they are connected in negative feedback either directly, or through some impedance network, they are able to replicate any analog operation (i.e. addition, subtraction, multiplication by a constant, and even non-linear transformations). Using the dynamic properties of capacitors enables frequency domain filtering, such as *low-pass*, *band-pass*, and *high-pass* filters to selectively resolve low, intermediate, and high frequency content in the signal, respectively. A simplified analysis of circuits containing opamps with negative feedback can be accomplished by making the following two assumptions:

1. The voltage drop across the input terminals is zero: $V^+ = V^-$; and

2. The opamp itself has infinie input impedance: $I_{IN} = 0$.

Armed with these two simplifying assumptions, and verifying the opamp is operating within its linear regime of design specifications (input/output voltage range, output current, bandwidth), the behavior of an AFE can be estimated by the standard *node analysis* technique, specifying Kirchhoff's current law (KCL) at each voltage node in the circuit except at the output of the opamp. The loss of this latter specification is however compensated by the extra specifications of the above simplifying opamp assumptions, ensuring an equal number of equations and unknowns in the circuit analysis.

Fig. 2.6 shows some common configurations of opamp circuits. Figures 2.6 (a) and (b) both implement pseudo-differential single-ended amplifiers with a single output
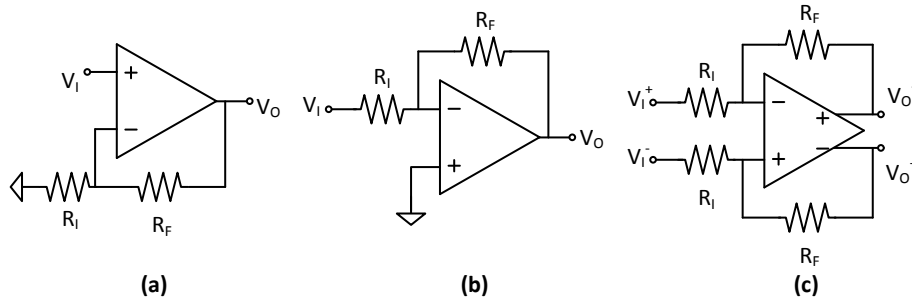
Figure 2.6: Types of operational amplifier configurations: (a) pseudo-differential non-inverting amplifier, (b) pseudo-differential inverting amplifier, and (c) fully differential amplifier.

referenced to a common ground; while Fig. 2.6 (c) implements a fully differential amplifier producing a differential output for a differential input signal.

A non-inverting operational amplifier is one type of configuration for the opamp providing positive amplification, where the signal input is connected to the positive input terminal and a resistive divider provides feedback to the negative terminal. Fig. 2.6(a) depicts the non-inverting amplifier. By applying the analysis technique detailed above we can derive the output as:

$$V_O = (1 + \frac{R_F}{R_I}) V_I \tag{2.9}$$

with positive gain strictly greater than unity. A main advantage of this topology is the (ideally) infinite input impedance it presents, as current does not flow into the opamp input terminals. One specific use of this circuit is as a unity gain buffer, where R_F is zero as a short and R_I is omitted as an open circuit, providing impedance buffering of a sensitive high-impedance voltage node.

The inverting amplifier is another widely used configuration for the opamp producing negative amplification, where the signal input is connected to the negative input terminal through a resistor while another resistor provides feedback to the negative terminal. Analyzing the circuit in Fig. 2.6(b) we obtain the output as:

$$V_O = -\frac{R_F}{R_I} V_I \tag{2.10}$$

with negative gain, the magnitude of which ranges anywhere between zero and infinity by adjusting R_F relative to R_I. One drawback of the inverting topology is that the input impedance, $Z_{IN} = R_{IN}$, is considerably low (kiloohms to megaohms) for any practically realizable resistance at high gain settings. This is undesirable for use in a biopotential recording AFE as electrodes have high impedances and may therefore attenuate the signal. The remedy commonly employed is to precede the inverting amplified by a voltage buffering amplifier such as the non-inverting amplifier.

The fully differential amplifier relies on a different kind of opamp which produces dynamically balanced differential voltage outputs amplifying the differential input. This is advantageous to reject common-mode noise and power supply interference. Fig. 2.6(c) shows how the dual differential outputs in this amplifier can provide negative feedback to both input terminals and thus present a balanced input impedance at both terminals. The differential mode gain of the fully differential amplifier is:

$$V_O = V_O^+ - V_O^- = \frac{R_F}{R_I} \left(V_I^+ - V_I^- \right) \tag{2.11}$$

Notice that although the output expression does not contain an explicit negative sign, the input and output polarities of the amplifier topology are flipped. Thus, we may consider this amplifier to be the differential form of the inverting amplifier in Fig. 2.6(b). It is not possible to configure a fully differential amplifier in a non-inverting mode equivalent to Fig. 2.6(a). For this reason, its input impedance is limited by the input resistors R_I. On the other hand, as the signal is encoded differentially between two terminals, the maximum signal output swing range is doubled.

2.3.1.2   Instrumentation Amplifiers

Instrumentation Amplifiers (IA) are used to measure small differential signals, while rejecting common mode levels. Another requirement of IA is high input impedance, to avoid attenuating signals from sensors with high output impedance. This requirement is fundamental in biopotential recording as electrodes frequently present very large impedance due to their small size or imperfect contact. Aside from attenuating the signal of interest, low input impedance greatly decreases the system's common-mode rejection ratio (CMRR), which is a measure of how well the instrument is able to reject common-mode noise and interference, equal at both terminals and hence zero by purely differential measurement. These and other important metrics are described in Section 2.4. Various strategies for improving IAs have been devised. Many of these specifically for the purpose of better recording biopotential signals. Fig. 2.7 showcases several alternative solution strategies to recording sensitive differential signals.
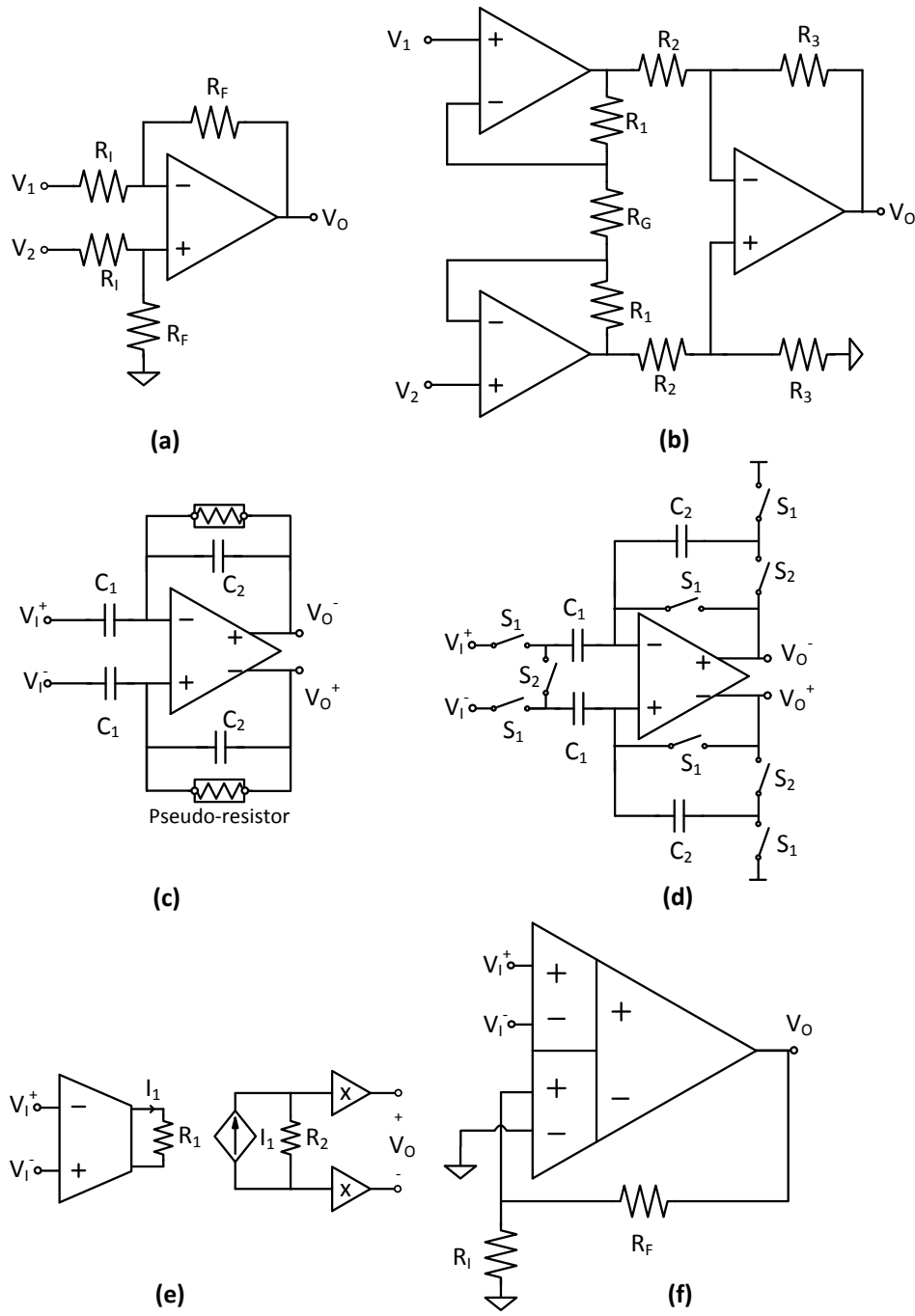
Figure 2.7: Architectures for differential and instrumentation amplifiers: (a) difference amplifier, (b) 3-opamp instrumentation amplifier, (c) fully-differential capacitively coupled amplifier, (d) switched capacitor instrumentation amplifier, (e) current balancing instrumentation amplifier, and (f) differential difference amplifier.

The difference amplifier as shown in Fig. 2.7(a) is the most basic circuit configuration to record a differential biopotential. It combines attributes of the inverting and non-inverting amplifier configurations. With matched resistances the output of this difference amplifier is:

$$V_O = \frac{R_F}{R_I} (V_2 - V_1). \tag{2.12}$$

Despite its simplicity, the basic difference amplifier suffers from several disadvantages that preclude its practical use for biopotential recording. Notably, having the input connect to the negative feedback terminal results in low input impedance on the order of R_I. Since large voltage gain requires relatively low values for R_I leading to input impedances in the kiloohm range, this configuration is almost never used directly to measure biopotentials. Additionally, unless the 4 resistors in this circuit can be perfectly matched (or in the correct ratio), this amplifier topology suffers from low CMRR.

The three-opamp instrumentation amplifier is the prototypical architecture for instrumentation amplifiers. It is also simply known as *Instrumentation Amplifier* (IA) without any additional description. In Fig. 2.7(b), we can see it is indeed composed of 3 opamps in two stages. In the first stage, 2 non-inverting opamps amplify the difference $V_2 - V_1$ into a differential output signal. In the second stage, a difference amplifier like the one shown in Fig. 2.7(a) provides further amplification and subtracts the common mode signal. Although not typical, it is also possible to implement this second stage with a fully-differential opamp. The transfer function of the classic IA is:

$$V_O = (1 + 2\,\frac{R_1}{R_G})\,\frac{R_3}{R_2}\,(V_2 - V_1). \tag{2.13}$$

This architecture is favored for its high differential gain and high common-mode rejection. Additionally, as the first stage is composed of output-coupled non-inverting amplifiers, it offers very high input impedance, allowing for biopotential measurements through non-contact and high impedance electrodes. One further advantage of this topology, is that changing a single resistor, R_G, allows for tuning of the differential gain of the circuit. Despite these advantages, resistor matching is still critical to achieving very high CMRR in excess of 100 dB, as needed in highly sensitive application settings such as EEG recording on the scalp but difficult to accomplish in an integrated process without laser trimming. Moreover, the use of 3 separate amplifiers results in extra noise and power consumption.

A fully differential capacitively coupled amplifier is effectively the same topology shown in Fig. 2.6(c), except the passive elements used for gain ratioing are implemented with capacitors rather than resistors. Capacitive feedback ratioing, particularly when Fig. 2.7(c) is implemented as an integrated circuit, ensures both accurate gain and lower power consumption for the IA. Achieving more accurate gain and better CMRR by accurate matching of pairs of capacitors like C_1 and C_2 is relatively straightforward in custom designed integrated circuits in standard semiconductor fabrication processes. Low power consumption is also more easily achievable owing to the ability to accurately integrate very small capacitances, that in turn give rise to very large impedances reducing the current draw of the amplifier. In order for the amplifier to have a stable DC operating point despite the infinite impedance of the capacitive elements lacking feedback at zero frequency, Fig. 2.7(c) makes use of very high resistance *pseudo-resistors*, which are leak

elements composed of self-biased transistors with ultra-high resistance [45]. Without such pseudo-resistors, implementing the large resistances in the gigaohm-teraohm range required for the high-pass filter cut-off frequency of biopotential recording would use prohibitively large silicon area. On the other hand, just like Fig. 2.7(a), low input impedance may be a problem at high signal frequencies for some implementations where the input capacitor C_1 is very large, possibly tens of picofarads. Minimizing the size of C_1 in this circuit, precludes achieving high gain as the transfer function within the pass-band is directly proportional to it:

$$V_O(j\omega_{pass}) = V_O^+ - V_O^- = \frac{C_1}{C_2}(V_I^+ - V_I^-).$$

(2.14)

A switched-capacitor instrumentation amplifier as shown in Fig. 2.7(d) is a discrete-time circuit that works by sampling the instantaneous voltage at periodic intervals, unlike the continuous-time amplification in the previous examples Fig. 2.7(a-c). In the sampling phase, the first part of the interval, the S_1 switches closes and charges the C_1 capacitors to the input voltage. The second phase has the S_1 switches open while the S_2 close setting the output to the product of the input and the above capacitor ratio. In order for the sampled voltage to completely settle in the relatively short phase interval, the effective bandwidth of the amplifier must be much faster than the continuous time signal bandwidth. This results in increased power consumption and integrated noise. Additionally, sampling a voltage onto a capacitor like C_1 results in a phenomenon known as kT/C noise. As the name implies, the mean square value of this sampling error due to thermal noise

26

is $\overline{v_n^2} = k_B T / C$, where k_B is the Boltzmann constant. Not having any preamplifier, the settling time of input capacitors is dependent on generally high-impedance biopotential electrodes. Despite this architecture's higher power consumption, the time discretization it performs can replace the sample and hold circuit of the subsequent ADC.

A current balancing instrumentation amplifier as conceptually demonstrated in Fig. 2.7(e) alleviates CMRR issues encountered in practical implementation of the above amplifier topologies due to difficulties in matching resistors, capacitors, and even whole amplifiers. An open loop transconductance amplifier first stage converts a differential input voltage into a differential output current I_1 which flows through the balanced resistor R_1. The current I_1 is then copied to flow through R_2 resulting in an amplified voltage which is then buffered by a final circuit. This topology may include some kind of current feedback to the first stage's output to cancel common mode. As is evident, the lack of duplicated resistors, capacitors, and amplifiers eliminates the CMRR losses due to matching. Although Fig. 2.7(e) has much higher potential CMRR and input impedance, low noise design might incur significant power costs in copying currents and powering all the stages.

A differential-difference amplifier is yet another type of instrumentation amplifier that seeks to maintain high input impedance and high CMRR despite matching challenges. It behaves like the fully-differential amplifier shown in Fig. 2.6(c) except without the inverting amplifier's low impedance inputs. Within this grouped amplifier, a first stage with two parallel amplifiers converts voltage inputs into currents, which are summed together and amplified by a second stage. The key in maintaining high-input impedance, is

using two isolated terminals exclusively for the input signal, and two separate terminals exclusively for feedback.

Other architectures and topologies are possible, and frequently featured in the scientific literature of biopotential amplifier design. Combining different features presented in Fig. 2.7 may improve the performance of a specific design targeting a particular application.

2.3.2 Intracellular Recording and Clamping Circuits

A different kind of neural instrumentation has been developed for the acquisition of intracellular potentials. These measurements of *membrane voltage* provide the means to study *in vivo* neural networks, the behavior of synapses, and even characterize single ion-channel transport proteins. Aside from characterizing the fundamental physiological behavior of trans-membrane proteins, these experiments can discover the effect of various drugs, genetic manipulations, and various pathologies on the basic building blocks of the nervous system.

In order to record the cell membrane voltage, a very different kind of microelectrode must be used. Commonly, a Ag/AgCl filament inside a glass pipette filled with saline fluid and a sharply tapering tip perforates the cell membrane probing the intracellular space. A more advanced technique, involves a *patch clamp electrode* which has a flat tip that can form a seal around a patch of the cell membrane, through suction on the electrode fluid. Additional manipulation can either perforate the isolated membrane region, forming a longer lasting intracellular interface than the sharp microelectrode; or purposefully tear off a section of membrane to specifically study its properties in isolation. Application

of these electrodes to *in vitro* systems requires specialized microscopy and mechanical micromanipulation tools. *In vivo* measurements of the intracellular potential require even more sophisticated optical and mechanical equipment. Beyond simply recording the intracellular potential, the following techniques are applied in neuroscience experiments:

2.3.2.1 Voltage Clamp

A voltage clamp is a configuration used to measure the behavior of ionic currents across the cell membrane while keeping the membrane potential constant. Practically, this is accomplished through feedback and operational amplifiers. A *potentiostat* is a circuit that sets a potential difference between two nodes while measuring the current required to maintain such potential. Fig. 2.8(a) shows a simple voltage clamp potentiostat circuit consisting of only one pipette electrode and one return electrode in the solution. Recalling the properties of opamps in negative feedback, the circuit will set the voltage at the inverting terminal to the input control voltage V_{clamp}, while the feedback across the amplifier through the transimpedance element R_F results in an amplifier output:

$$V_O = V_{clamp} + I_{meas}\,R_F. \tag{2.15}$$

A second amplifier may be used to subtract the V_{clamp} and isolate the term directly proportional to the membrane current. Unfortunately, due to R_A, the access resistance of the microelectrode, the membrane voltage is not exactly equal to the clamp voltage but rather

$$V_m = V_{clamp} - I_{meas}\,R_A, \tag{2.16}$$

which depending on the magnitude of R_A can be significantly different. One solution to this problem is to have two different pipette electrodes: one recording the intracellular voltage, and one injecting current. As there is no current flowing through the recording electrode (connected to a different high input impedance amplifier), there is no voltage difference between the command voltage V_{clamp} and V_m. This 3 electrode potentiostat, which requires probing the same cell with 2 different pipettes, is difficult to use in small neurons. A different approach towards constructing a voltage clamp with a single penetrating electrode, involves time multiplexing the voltage sensing, and current injection functions. Although this method manages to record from the electrode when there is no current (therefore no voltage drop) the settling time of this feedback control system must be smaller than the time constant of the neuronal membrane.

2.3.2.2 Current Clamp

A current clamp is used to investigate the excitability of neurons. Keeping a certain current injection while monitoring the potential generated is known as a *galvanostat*. Fig. 2.8(b) shows a galvanostatic current clamp instrument implemented by simply measuring the potential on the intracellular electrode connected to a current source. A current that discharges or *depolarizes* the membrane voltage eventually leads to an action potential. This action potential manifests as a sudden spike in the membrane voltage that is recorded by the current clamp. Similarly to the voltage clamp, a current clamp composed of a single intracellular electrode cannot simultaneously inject current and faithfully record the exact membrane voltage. Contrasting from the voltage clamp case, the clamp current setting

I_{clamp} is accurately set, and the current dependent term in the voltage measurement can be eliminated in post-processing of the data if the electrode properties of R_A are known:

$$V_O = (V_m + I_{clamp} R_A)(1 + \frac{R_F}{R_I}). \tag{2.17}$$

2.3.2.3   Dynamic Clamp

A dynamic clamp is an advanced rendition of the above voltage and current clamp techniques, where the instrument can inject currents generated with a prescribed algebraic dependence on the membrane voltage, emulating a variable conductance on the electrode side of the interface. The dependence of these currents on voltage can take the mathematical expression of neurotransmitter receptors and different ion channels that exist in the cell membranes of neurons. Among other applications, technique can enable investigations of neuronal responses to the uniquely behaving ion channels, and even simulating the complex dynamics of chemical synapses in order to form hybrid biological-neuromorphic neural networks. Dynamic clamps can be fully implemented with analog circuit control systems that enforce the desired I-V relationship, or they can be implemented through digitization and digital signal processing (DSP) in the loop.

2.4   Design Considerations and Performance Metrics

Innovations in semiconductor technology and new circuit design topologies constantly empower newer, more demanding applications in neural engineering. Although these advances have enabled the impressive miniaturization of modern technology, many functional
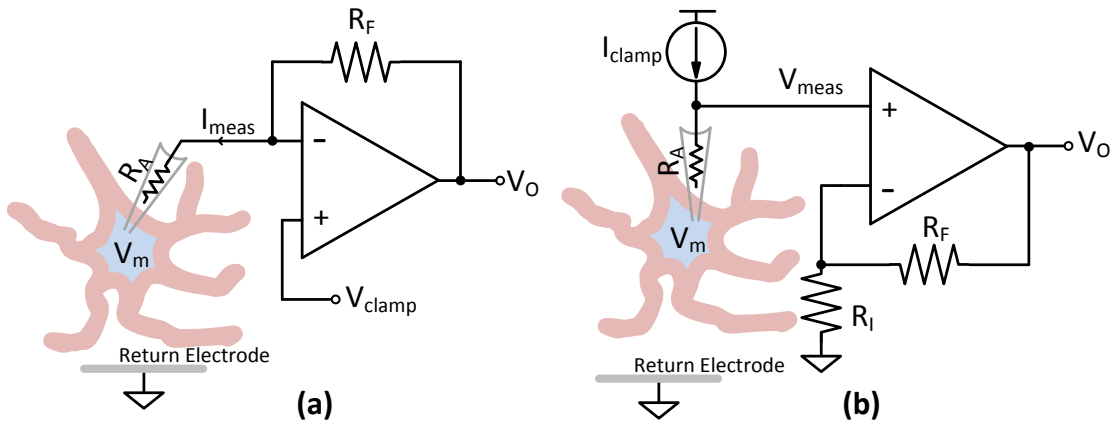
Figure 2.8: Basic instantiations of (a) voltage clamp and (b) current clamp instruments making use of a single intracellular electrode.

aspects of circuit design result in performance trade-offs. In this section we discuss some design considerations, and decisions that must be made in order to optimize performance, and the metrics that define performance quality.

2.4.1 Power Consumption

One of the primary factors limiting design choices in instrumentation is power consumption. Particularly in the case of implantable, portable, and wearable systems, gratuitous power consumption is detrimental. These systems are generally limited by how much instantaneous power they can harvest, and how much total energy they can store in a battery. As such, power autonomy is a critical consideration. Another consequence of high power consumption, is excessive heat generation which can cause tissue damage and discomfort to users of biopotential recording equipment. The objective of minimizing power

conflicts with other design requirements. The level of power used in the instrumentation, particularly the AFE, directly affects available bandwidth and signal-to-noise ratio, equally important as design considerations in ensuring sufficient signal quality. Therefore, judicious administration of a power budget among all the blocks of a neural recording and stimulation instrument is of critical importance.

2.4.2   Bandwidth

As discussed in Section 2.1 and Fig. 2.2 the temporal resolution of biopotential signals varies extensively across specific applications. The AFE used in a particular application must be adapted or configured with sufficient bandwidth to amplify the targeted biopotential signals, avoiding aliasing and distortion degrading the signal. Because noise and interference from the electrode and outside sources can decrease the signal to noise ratio (SNR), amplifier systems are generally designed to limit undesirable content outside the frequency band of interest. Even without the need to reject out-of-band interference, having excessive bandwidth in the AFE can include more total integrated noise to the final digitized signal, and needlessly consume more power.

2.4.3   Input Dynamic Range

Large gain amplifiers are required to magnify biopotentials from the lower- to mid-μV range to cover the full ADC input range in order to maximize precision in signal acquisition. This in turn limits the maximum amplitude of a signal that can be received without saturating the output of the first stage AFE. Some types of instruments require

great flexibility in configuring gain and bandwidth settings because they receive different ranges of signals. For example, some MEA systems record intracellular action potentials with approximately 100 mV peak to peak amplitude, as well as extracellular local fields with μV-range amplitudes. Some common methods employed to increase input dynamic range (IDR) include: AC-coupling or high pass filtering DC-offsets, having programmable or automatically adjusting gain, and predictive autoranging.

One important reason for increasing IDR, is the possibility of recording biopotentials simultaneously with electrical stimulation, enabling applications such as closed-loop deep brain stimulators (DBS), closed-loop retina prosetheses, and other emerging therapies. Even in conventional clinically implemented applications, recording biopotentials in the presence of large interference signals arising from other devices and surgical tools is not uncommon.

2.4.4   Cross-Talk

Advances in neural instrumentation have allowed researchers and users of the technology to increase the number of channels that they can simulatenously record. This increased throughput has been made possible due to increasing miniaturization of electrode arrays, connectors and interconnect traces. Cross-talk is the presence of interference signals from other channels in a particular channel. Cross-talk is likely to be caused by capacitive and other coupling between electrodes or interconnect traces in the circuitry. Material selection in the insulation and encapsulation layers must be considered, as well as the possibility these will degrade over the lifetime of the device giving rise to even more cross-

talk. Beyond actual cross-talk, designing electrode arrays with overly fine pitch exceeding the spatial resolution of the signal of interest (Fig. 2.2) does not result in a significant increase of information, while giving rise to many of the problems that result in cross-talk and noise. Although cross-talk is not primarily a circuit architecture issue, the addition of electrode impedance monitoring circuits to AFEs can accurately quantify the existence of cross-talk. Most typically, the cross-talk can be adequately compensated through DSP, and often the cross-talk contributed by the instrumentation is negligible to the amount of cross-talk already present in the signal due to volume conduction such as in EEG recorded on the scalp.

2.4.5 Noise

Noise is a more fundamental problem in neural instrumentation, which needs to be managed through careful design considerations in the electrodes and the interface circuits. Noise limits the attainable precision in biopotential recording. Many design choices can determine how much noise is added to the physiological signals in the process of acquisition and digitization. Beyond the thermal noise and $1/f$ noise inherent to the electrode-electrolyte interface discussed in Section 2.2.1, additional noise is contributed by circuit components in the electronics. The most significant noise contribution takes place directly at the input stage of the AFE, where signal amplitudes are smallest and most susceptible to the presence of additive noise. In contrast, subsequent stages in the signal processing pipeline operate at signal levels substantially higher than the levels of additional noise sources present. It is useful to consider the effect of noise from each stage, as the

equivalent *input referred noise* by dividing the magnitude of noise by the total accumulated gain from the AFE input to the noise source origin. This way the effect of electronic circuit noise can be directly compared by computing the signal to noise ratio (SNR), the ratio of the signal power over the noise power.

2.4.5.1   Front-End Amplifier Noise Model

The noise contributed by active and passive resistive components in the AFE circuit can be minimized through systematic model-based transistor-level circuit design. The transistors and resistors that are inside an AFE generate two major types of noise: thermal noise, and flicker or $1/f$ noise. Like the thermal noise due to ionic motion at the electrode-electrolyte interface, thermal noise generated in the AFE results from the random walk thermal fluctuations of electrons or holes in semiconductors. The model of thermal noise contributed by a single transistor in saturation and weak inversion depends on drain current I_{DS} as follows [91]:

$$\overline{i_{n,th}^2} = 2q\overline{I_{DS}}\Delta f \tag{2.18}$$

where q is the charge of an electron, and Δf is the signal bandwidth. As evident from (2.18) the average square noise is linearly proportional to the average drain current, while the signal power is proportional to the drain current square. Thus the SNR linearly improves with the magnitude of current. Consequently, increasing the current while maintaining voltage at the same level directly increases power consumption. This results in a trade-off between thermal noise reduction and power consumption. Strategies to reduce thermal noise without increasing power consumption involve low voltage and higher current circuit

architectures.

Likewise, flicker noise, also known as $1/f$ noise or pink noise, results primarily from trapping and release of charge carriers, at random time intervals, by lattice impurities at the Si/SiO_2 oxide interface surrounding the semiconductor active element. which contributes a significant source of noise at low frequency [72, 102]:

$$\overline{i_{n,f}^2} = \frac{g_m^2 K}{C_{ox} W L} \frac{1}{f} \Delta f \tag{2.19}$$

where g_m is transconductance, K is a process-dependent constant, W and L are width and length of the MOS transistor, and C_{ox} is the gate oxide capacitance. In some processes, PMOS transistors are known to have less $1/f$ noise than NMOS transistors, and therefore are often used in the input differential pair of a front-end amplifier for low-noise low-frequency applications in biosensing. Enlarging the MOS device size also decreases $1/f$ noise inversely proportional to area.

An alternative approach to mitigate flicker noise in area-limited designs, involves a high-frequency *chopper* that translates the input signal to a higher frequency for amplification, and subsequently translates it back to the original frequency [29]. Expectedly, chopping is not without trade-offs: increased power, decreased input impedance, and somewhat higher thermal noise. Another frequently used method to mitigate flicker noise, as well as low-frequency drifts and offsets, is *correlated double sampling* (CDS) [28], in which two samples of the amplifier output are collected in close succession; one measuring the signal, and another measuring a reference such as ground by bypassing the electrode input with an external reference or connecting to a separate reference electrode. The premise of

this technique is that $1/f$ noise and other low-frequency noise sources are highly correlated over short time scales, so that periodic auto-zeroing at sufficiently high rate eliminates most of it. The periodic auto-zeroing with the reference decimates the signal bandwidth, or requires sampling at higher frequency to maintain the same signal bandwidth, which is worthwhile only if the decrease in flicker noise power is greater than the increase in thermal noise power, when the $1/f$ noise corner lies in the signal band, a condition met at higher amplifier bias levels maximizing signal-to-noise ratio rather than minimizing power.

2.4.5.2   Net Noise Contributions

The relative contributions between electrode noise and circuit noise depend on electrode type and geometry, and on the available power budget for signal amplification. In general, electrode noise is strongly correlated with the contact impedance, but the actual level is significantly higher than just the thermal noise from the resistive portion of the impedance, especially for dry-contact electrodes that are gaining more wide-spread use than conventional wet-contact gel-based electrodes for their greater comfort and long-term endurance [14]. The aggregate sum of the electrode noise sources can be quite large, on the order of $\mu V/\sqrt{Hz}$ at 1 Hz, even for wet electrodes. This far exceeds the noise contribution of circuit components, illustrating the importance of proper electrode selection. Due to integrated current noise, both wet and dry electrodes have sharp $1/f^2$ spectra, which show up as baseline drifts in the time domain [14].

Non-contact electrodes can pick up additional noise from the insulating material between the metal and skin [14]. In particular, acquiring signals through fabrics can be

noisy due to the intrinsic high resistance of the fabric (>100 $M\Omega$). This amounts to the equivalent of inserting a large resistor in series with the amplifier input and can add significant noise in the signal bandwidth.

2.4.6 Interference and Common-Mode Rejection

In addition to the intrinsic noise sources that are fundamental to the operation of the electrodes and circuits, external noise and interfere due to parasitic electrical coupling from the environment as well as biasing and supply variations may also contaminate the signal. Unlike the intrinsic noise, the extent of parasitic coupling from the environment, such as line noise at the 50/60 Hz mains frequency, can be controlled through careful design of the cabling connecting the electrodes and AFE, as well as the AFE circuits themselves. In particular, common-mode noise sources, that couple nearly identically to the positive and negative leads of the AFE, can be completely eliminated with a properly designed truly-differential AFE.

2.4.6.1 Differential Sensing Circuit Techniques to Mitigate Common-Mode Interference

The most thorough means to eliminate interference due to parasitic electrical coupling from the environment is to completely shield the wiring between electrodes and AFE, such as by using coaxial cabling in which the signal is carried on the inner core surrounded by a solid ground shield. This solution, adding substantial capacitance on the signal line and incurring extra costs, is often impractical and unnecessary. A simpler

solution is to ensure that the two wires carrying the signal and the reference are subject to the same interfere, which then appears as a common-mode additive disturbance to the differential signal between the wires. By physically bringing the two wires in close proximity along their entire length, any parasitic electrical coupling from the outside would be nearly identical to both of them. A practical means to realizing near-identical parasitic coupling is a *twisted pair* of conductors. This strategy can be employed even on printed circuit boards or integrated circuits by periodically exchanging sides between pairs of metal lines carrying signal and reference through equally spaced via bridges.

To completely eliminate any common-mode disturbances, it is critical that the AFE fully rejects them, and purely amplifies the difference in potential between the non-inverting V_I^+ and inverting V_I^- inputs. An ideal differential AFE outputs a voltage V_O proportional only to this difference $V_I^+ - V_I^-$; practical limitations in the circuit implementation may produce an additional component in the output that depends on the common mode $(V_I^+ + V_I^-)/2$:

$$V_O = A_d \ (V_I^+ - V_I^-) + A_{cm} \ \frac{1}{2}(V_I^+ + V_I^-) \tag{2.20}$$

where A_d and A_{cm} are the differential gain and common-mode gain of the AFE, respectively. AFEs with higher *common-mode rejection ratio* $\mathrm{CMRR} = A_d / A_{cm}$ are proportinally more effective at suppressing common-mode noise relative to the differential signal. Most AFE designs offer a CMRR greater than 80 dB; this implies that common-mode disturbances at the input will be attenuated 10,000× more strongly than the differential signal is being amplified. This is important as 50/60 Hz mains line noise coupling to the electrodes and

wiring can easily exceed mV-levels and otherwise inundate μV-level biopotential signals present between the electrodes.

2.4.6.2 Input Impedance-Boosting Techniques

Even an AFE with perfect common-mode rejection (infinite CMRR) may still suffer from common-mode leak-through in the presence of an inbalance in impedances between the signal and reference paths feeding to the non-inverting and inverting AFE inputs. These imbalances are unavoidable despite careful design of the AFE circuit, because the electrode-electrolyte/tissue interface impedance is highly variable and unpredictable. Due to the finite input impedance into either or both non-inverting and inverting input terminals to the AFE, these variations in interface impedances at the signal and reference electrodes cause a leakage of the common-mode voltage from the electrodes, into a differential component between the AFE inputs. This differential leakage cannot be distinguished from the true differential voltage between the electrodes by the AFE, and hence passes through with full magnification. The effect of this leakage is equivalent to an *effective CMRR* of the AFE:

$$\text{CMRR}_{\text{eff}}(j\omega) \approx \frac{|Z_{in}(j\omega)|}{|Z_{sig}(j\omega) - Z_{ref}(j\omega)|} \tag{2.21}$$

where Z_{in} is the AFE input impedance, and Z_{sig} and Z_{ref} are the electrode-electrolyte/tissue impedances for the signal and reference electrodes, respectively. In addition to their effect in degrading CMRR, variations and mismatch in electrode impedances also reduce signal amplitude, and make the system more susceptible to movement artifacts. Therefore, it is of paramount importance to mitigate all these effects by maximizing the AFE input

41

impedance well beyond the expected range and variation in electrode impedances.

Although the AFE input resistance R_{in} is typically very high (in the teraohm range), the magnitude of its input impedance $|Z_{in}(j\omega)|$ at higher frequencies can be substantially smaller due to AFE input capacitance, in addition to line capacitance in carrying the signals from the electrodes to the AFE. In many cases, the input impedance is limited by the parasitic switched-capacitor resistance of the input chopper or by the AC-coupled input capacitors. A positive feedback can bootstrap the AC-coupled input capacitors to boost the input impedance, achieving input impedance on the order of gigaohms. In order to further boost the input impedance to teraohm levels, a unity-gain amplifier with active shielding can be used to bootstrap capacitance of the input transistor and all other parasitic capacitance [15, 54].

2.4.6.3   Active Grounding – Driven Right Leg

An alternative to techniques boosting CMMR by active boosting or active shielding of parasitic input capacitance is to mitigate common-mode noise and interference directly through *active grounding*. Rather than minimizing common-mode gain A_d, active grounding operates by dynamically driving the common-mode voltage $V_{CM} = \left(V_I^+ + V_I^-\right)/2$ close to zero. This is accomplished by sensing the difference between the common-mode voltage V_{CM} and ground, and feeding back the amplified difference with large negative gain to an additional *active ground* electrode in contact with body tissue. The location for this electrode is typically far removed from signal carrying electrodes in order not to interfere with the electrophysiogical setup. For electrocardiography (ECG) applications, this ground

electrode is typically applied to the right leg, hence the term "driven right leg" (DRL) commonly used to refer to the active grounding circuit, no matter where this electrode is applied. For EEG applications, the DRL electrode is typically applied on the mastoid behind the ears.

Active grounding is much more effective than passive grounding by directly connecting the body to ground due to the impedance of the ground electrode, causing voltage variations away from zero due displacement currents induced by 50/60 Hz mains line noise and other sources of common-mode noise acting on the body. Active grounding with DRL accomplishes an effective grounding impedance that is smaller than the electrode-tissue impedance by a factor $1 + A_{DRL}$, where A_{DRL} is the open-loop gain of the DRL amplifier. Hence large reduction in common-mode voltage can obtained by large DRL gain.

In order to obtain large gain in the DRL circuit, an open-loop amplifier can be employed. However, the feedback by the DRL circuit requires careful design for stability. The DRL amplifier is typically integrated with the AFE differential amplifier on the same die and using same design principles; for instance capacitive feedback with pseudo-resistors around an OTA can realize a low-power DRL along with the capacitively coupled AFE implementation in Fig. 2.7 c). Typically, large capacitance up to a few nF is required to ensure stability due to variation in electrode impedances. A digitally assisted DRL circuit has the capability to have larger gain at the mains frequency for higher rejection and lower gain elsewhere for stability. In dry-electrode applications, common-mode feedback to one of the differential inputs in the front-end increases CMRR, and ensures its stability independent of electrode impedance variations.

43

For safety, a large (megaohm-range) resistance is typically connected in series with the DRL output, limiting its range of output current for short-circuit protection while leaving the DRL open-loop gain unaffected for precise active grounding.

2.5 Survey of Neural Engineering Applications

The field of neural engineering has made significant progress towards useful and viable technologies for interfacing with the brain and body. Tools for neural recording have been developed to reliably measure everything from the fine details of action potentials *in vivo* to wide, body-area electrophysiological signals. Advancements in electrode sensor materials, high-performance integrated circuits (ICs), and precision miniaturization of complex systems have improved existing applications such as EEG and enabled new applications such as μECoG and vision restoring retinal implants. When exploring neural engineering concepts for a specific application, consideration is necessary of the particular biopotential to be investigated (i.e. spikes, LFP, brain waves, nerve impulses, etc.), the physiological source of the biopotential signal (i.e. the brain, brainstem, or peripheral nerves), and the limitations of available recording technologies.

2.5.1 Electrodes and Instrumentation

2.5.1.1 Scale and Invasiveness

Sensing biopotentials with large devices external to the human body produce very different signals than small implanted devices. In part, this is because of a trade-off in scale

between surface area coverage and location-specific access. Gel electrodes placed on the surface of the scalp connected to a biopotential amplifier for example, could easily cover the entire projected surface of the brain accessible on the head but would pick up only faint, low-frequency signals because of the shear distance of the neuron sources through the skull to the external electrodes. The obvious advantage of external electrodes like those used for scalp EEG is that they enable a non-invasive neural interface. On the otherhand, if greater biopotential quality and neural signal features are desired and invasive implants are acceptable, electrode sensors can be placed very close or even through neurons in the brain. Large-area neural engineering tools for biopotential measurement include scalp electroencephalography EEG, magnetoencephalography (MEG), electrical impedance tomography (EIT), and epidural ECoG. Small-area neural engineering tools for biopotential measurement include subdural ECoG, cortex microelectrode arrays, μECoG, and deep brain microelectrode arrays.

2.5.1.2   Temporal, Spatial, and Spectral Resolution

Examples of neural engineering applications can be categorized based on the resolution they are capable of achieving in the spatial, temporal, and spectral domains. For applications involving fast neural signals such as action potentials and short-wave ripples, an amplifier and analog-to-digital converter (ADC) with sufficiently high sampling rate are required to capture the fine temporal features in the signal. Some signals, such as those arising from the mid brain and hippocampus, need to be measured in close proximity to the source and thus require high spatial resolution from the recording apparatus. High-density

45

microelectrodes inserted in the mid brain are currently required in this setting to spatially resolve these signals. Perhaps the most important element of distinction between neural interfacing tools is spectral resolution. Certainly the distance between the source and sensor affects the range of spectral measurable because of the inherent low-pass filtering nature of biological tissues, but other factors arguably play a greater role in determining the spectral resolution of the system. These factors can include the noise floor of the acquisition circuitry, the $1/f$ noise of the amplifier, impedance of the electrode, and sampling frequency.

2.5.1.3   Experiment Model

Neural engineering tools to be used for a specific application will also depend on the type of experiment and biological model to be used. To measure from the brain *in vivo*, one could use any of the above mentioned tools. To measure from the peripheral nervous system, implantable nerve cuff or nerve needle electrodes are needed instead. In experiments involving small animals such as mice, a head-mounted sensing module should be considered. Mouse EEG has small screw-like electrodes that push up against the skull to measure brain activity, while allowing the animal to move freely. In other settings a sample of neural tissue such as a brain slice will need evaluation *in vitro*, in which case, a microelectrode array with high-density recording units and liquid containment for culture media is necessary. Finally, in cases where neurons are being grown in cell culture from either explants or iPSCs, a multielectrode array with sharp points or nanowires will enable intracellular recordings, in addition to extracellular and intercellular recordings.

2.5.1.4 In-Ear Placement

Applications of neural engineering involving discrete wearable sensors have continued to gain popularity. A particularly promising unobtrusive electrophysiology modality is *Ear-EEG*. Unlike conventional EEG which has several electrodes placed on the forehead and scalp, Ear-EEG provides a miniaturized and discrete platform for electrode placement in the outer ear and in the ear canal [36, 63, 86]. Electrode sensors can be integrated into existing personal audio devices such as hearing aides and wireless earphones. Signals recorded from these sensors are comparable in quality to those measured from conventional EEG for certain event-related potentials owing, in part, to the proximity of in-ear electrodes to major auditory processing centers of the brain, such as the auditory cortex in the temporal lobe, the brainstem, and the auditory nerve fibers [36, 63, 86]. Furthermore, the ear canal has been demonstrated to contain useful biomarkers of overall health and physiology. These biomarkers include electrodermal activity (EDA), a biomarker for overall excitement or stress levels, sodium-sweat concentration, a representative measure of hydration, and cerumen conductance, an indicator of sebum production and lipid transport [87, 106]. These unique attributes of the in-ear environment play a role in the dynamics of electrode-skin impedance, the understanding of which is important for high-quality biopotential measurement and consistency in offset between trails, different subjects, and in extended-period, continuous health monitoring.
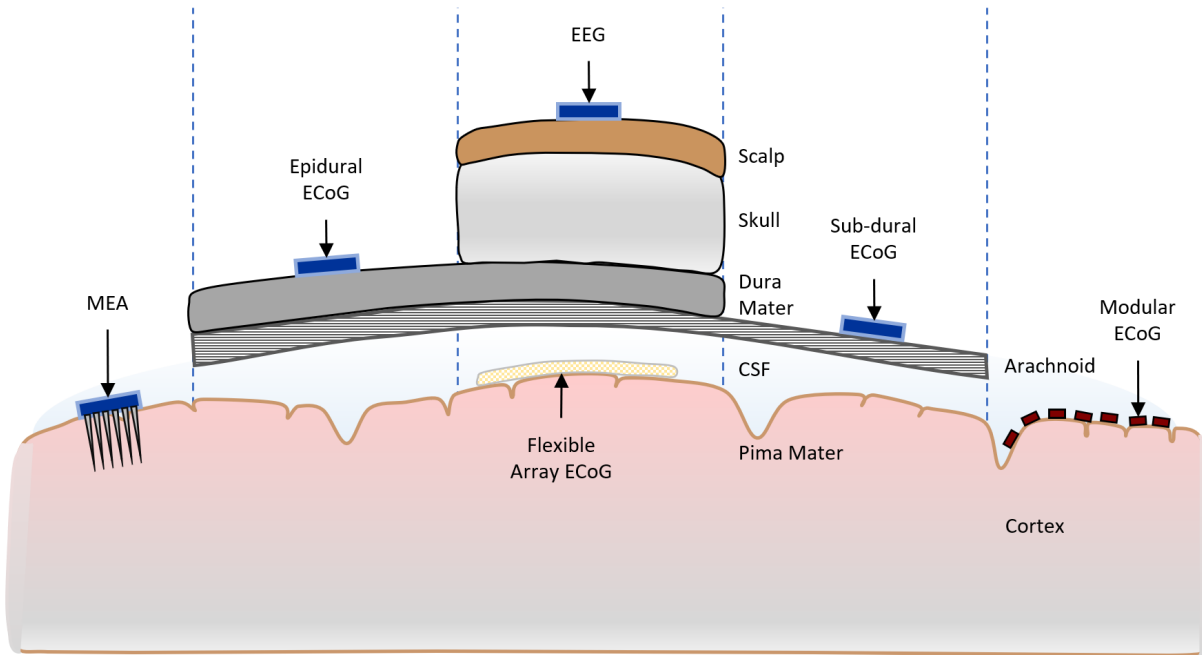
Figure 2.9: Types and positioning of integrated electrode technologies for interfacing with the brain at varying spatial scale and spectral bandwidth, at corresponding varying degrees of invasiveness [40].

2.5.2   Minimally Invasive Electrocorticography

EEG recording off the scalp is noninvasive and relatively low-cost, but limited in its spatiotemporal resolution. To achieve higher spatiotemporal resolution and spatial coverage in interfacing with the brain, the distance between the electrodes and neural tissue must be reduced. This implies a need to cross from the regime of non-invasive modalities to invasive, implanted technologies. Significant demand by academia, government funding agencies, and even the private sector for advanced brain research has driven the development of such chronically implantable neural interfaces that leverage precision material fabrication techniques and high-performance amplifier and wireless IC technologies. As elaborated in the following section, penetrating electrode systems tend to be very high resolution,

expensive, and very invasive, causing long-term tissue damage. An excellent middle ground, electrocorticography (ECoG), offers superior spatial and temporal recording resolution compared to EEG, lower cost of fabrication, and is suitable for chronically implantable use for practical long-term brain research, brain computer interface (BCI), and cognitive rehabilitation. A number of technologies are enabling next-generation fully implantable high-density ECoG systems, including PEDOT electrodes [13], signal amplifying and filtering frontend ICs [60], drivers for voltage and current stimulation [38], and wireless antennas for power and communication [84].

One such next-generation ECoG tool known as ENIAC, or *encapsulated neural interfacing acquisition chip*, places small microchips across the cortical surface of the brain to create a network of sensors covering a broad spatial area and recording individually at high spatiotemporal resolution [40]. Like μECoG, this new form of interfacing being termed modular-ECoG (mECoG), has a small footprint in regard to both physical implanted space and power consumption.

2.5.3 Design Example: ENIAC Analog Front End

The novel design of the ENIAC microsystem depicted in figure 2.12(c) presents unique system requirements for its electrodes and AFE.

2.5.3.1 System Description

In order to accomplish fully modular μECoG the ENIAC system was designed to be completely integrated on a single silicon die without the need for external discrete parts or
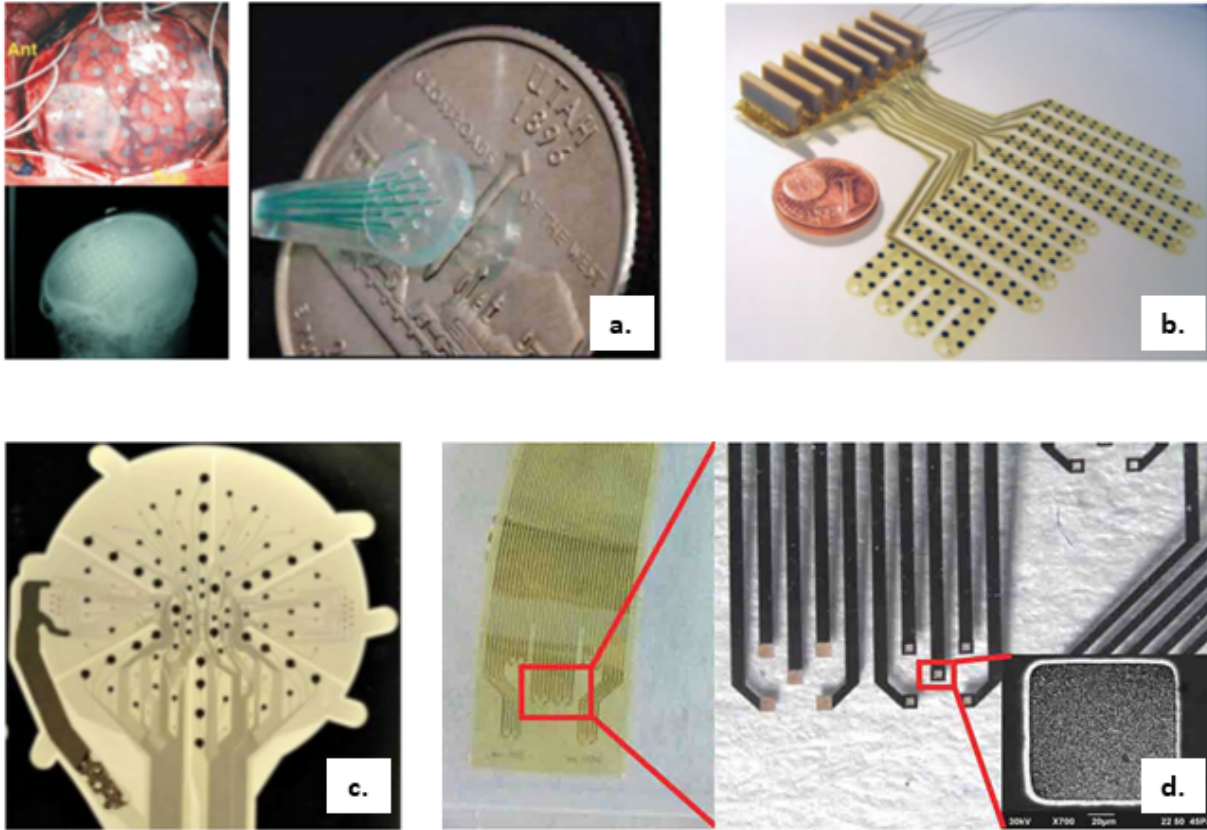
Figure 2.10: ECoG integrated neural interface technologies and applications. (a) Subdural ECoG array with an electrode diameter of 2 mm and electrode pitch of 1 cm. The radiograph image shows the position of the ECoG array implanted in the subject on the cortex surface, below the skull [60]. (b) Flexible 252-channel electrode array fabricated from thin polyimide foil substrate for implanted ECoG [90]. (c) μECoG electrode array with 3 different electrode diameters and a total of 124 recording sites [101]. (d) Electrode array with low impedance electrodes fabricated for biopotential recording from PEDOT-carbon nanotube (CNT) composite coatings [13].

packaging. The electrodes for neural interface and the coil for power and data transmission are also integrated on-chip. Figure 2.13 shows the ENIAC block diagram, including the dimensions and intended surgical placement. The on chip electrodes should be coated with a thin biocompatible encapsulant that is also a high-k dielectric, thereby forming a capacitive electrode interface. These electrodes are then connected to a switch matrix to
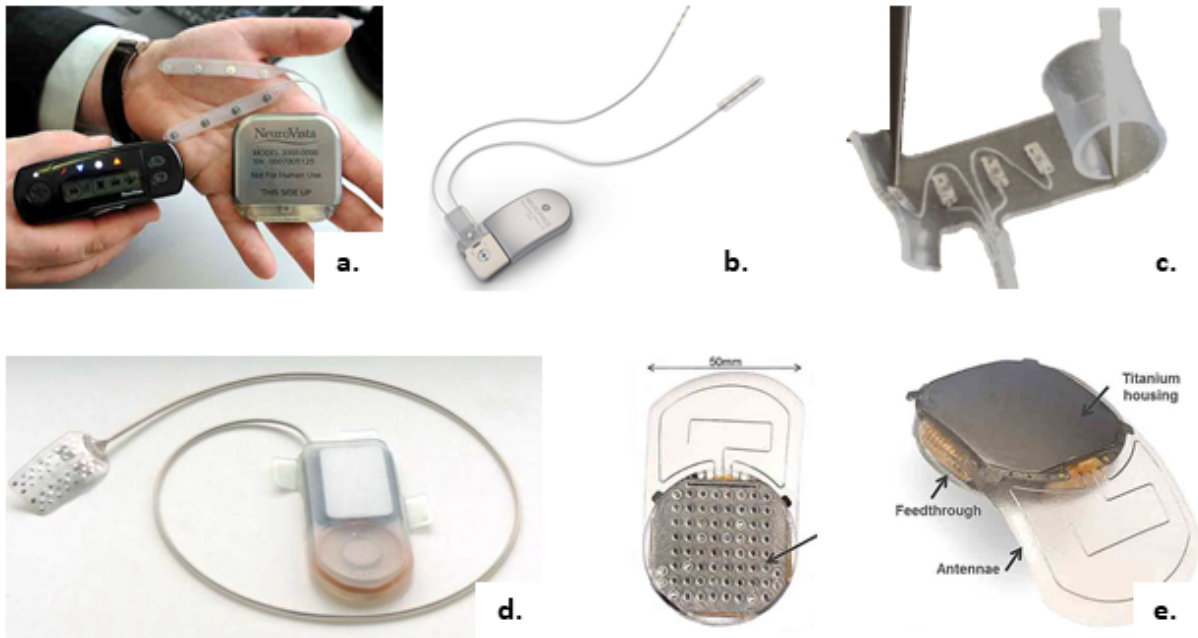
Figure 2.11: Clinically available neural interface systems and applications. (a) *NeuroVista* seizure advisory system monitors biopotentials in the brain [22]. (b) *Neuropace* RNS system monitor biopotential activity of the brain leading up to and preventing seizures [99]. (c) Spiral nerve cuff electrode for biopotential measurement of peripheral or spinal nerves [2]. (d) *BrainCon*'s BCI system for general-purpose medical neural interfacing [31, 92]. (e) *WIMAGINE* wireless implantable multi-channel neural interface [73].

select the size and location of the connected electrodes. The switch matrix also controls whether the electrodes are connected to the AFE or the stimulator.

2.5.3.2 Design Requirements:

As the target signal to be recorded is μECoG (Fig. 2.2), the small spatial distance between electrodes will capture smaller amplitude than conventional ECoG on the order of <1mV. Given this peak amplitude, the noise requirement for the AFE is approximately 2-5 μV integrated for the entire signal bandwidth between 1Hz-1kHz. Additionally, given the high electrode impedance the AFE architecture should support high input impedance. The
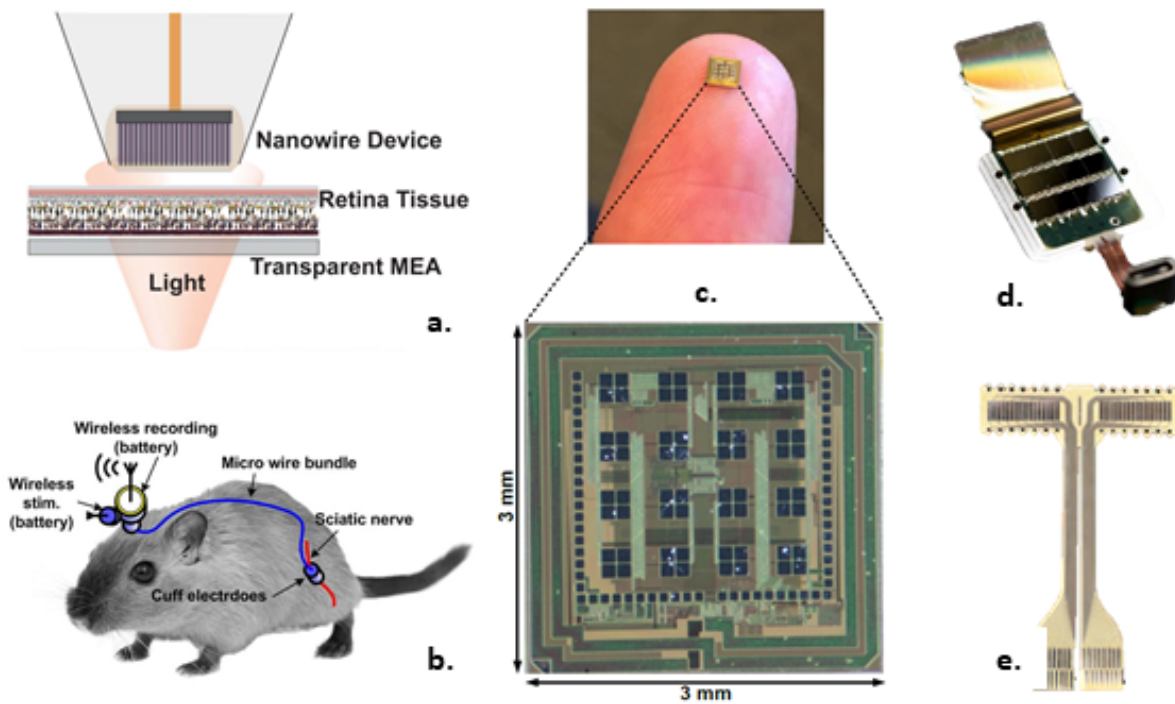
Figure 2.12: Emerging technologies for next-generation neural interfaces and applications. (a) High-resolution retinal prostheses with optical addressing and inductive telemetry, towards retinamorophic vision restoration in patients with degenerated photoreceptors in the retina [41]. (b) An implantable nerve cuff for biopotential recordings of the peripheral nerevous system in freely moving animal subjects [59]. (c) The *encapsulated neural interfacing and acquisition chip* (ENIAC) is a completely on-chip integrated system for ECoG recording, stimulation, and data transmission [38, 40, 57]. (d) The *Neuralink Neuralace* implantable BCI platform that offers thousands of biopotential recording channels [75]. (e.) Thin film, high-density peripheral nerve cuffs for biopotential recording of the injured nerves used pre- and post-operatively [48].

CMRR must also be high enough to reject signals common to multiple electrodes. Finally, as harvested power is scarce, it may not consume beyond a few μW.

2.5.3.3 Circuit Architecture

Figure 2.14 shows the schematic of the ENIAC AFE circuit. Initially, the signal interfaces with our system through a capacitive electrode. A high voltage tolerant switch

52
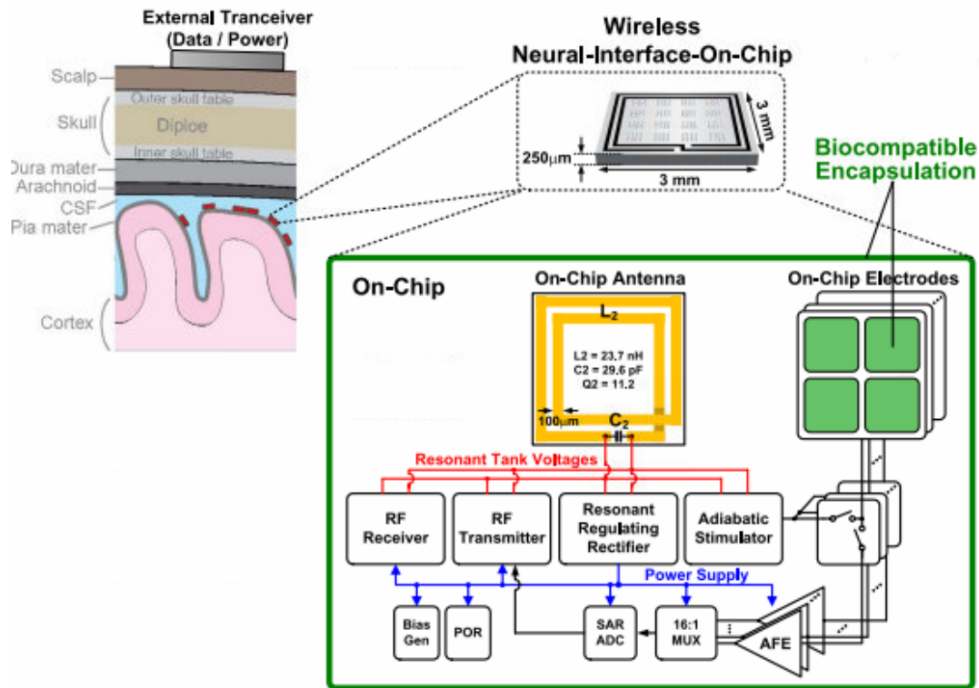
Figure 2.13: Encapsulated Neural Interface and Acquisition Chip System Block Diagram [39]. On-chip capacitive electrodes connect to the analog front end or the adiabatic stimulator

matrix multiplexes the electrode pads between the stimulator and amplifier, protecting sensitive internal circuits. The input signal is high pass filtered by the input capacitor and a pseudo-resistor connected to the target common voltage. The first stage is composed of a low-noise non-inverting amplifier with reset capability. The second stage is an inverting programmable-gain amplifier referenced to the common-mode signal. Programmability is beneficial in order to take maximum advantage of the ADC input range. Pseudo-resistors and reset switches are included to set the DC operating point of the system. By using the electrode selector switch, fully differentially amplified signals from any two different (sets of) electrodes can be output to the ADC.
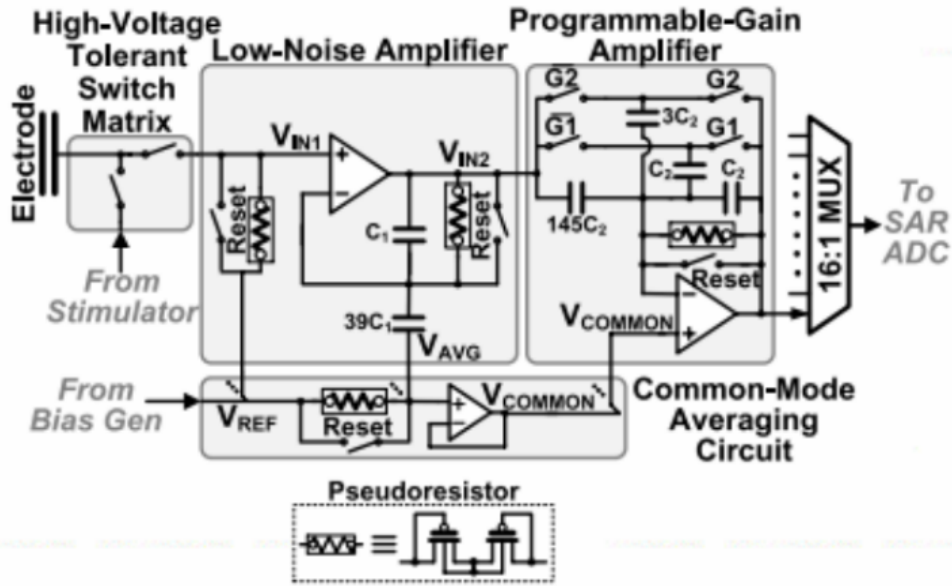
Figure 2.14: Schematic of the ENIAC analog front end [39]

2.5.3.4   Test Results

Figure 2.15 summarizes the results of the ENIAC AFE test. The left plot shows the 2-bit programmable gain controlled by the switches in the second stage, as well as the system bandwidth. Additionally, the minimum CMRR for the appropriate signal bandwidth is shown. The right plot shows the spectrum of the input referred noise for a shorted input to the AFE, as well as the power consumption given its 0.8V power supply. In total, the system has $1.49\mu V_{rms}$ integrated voltage noise (input referred) for a $1.96\mu W$ power consumption. This corresponds to an NEF of 4.02 at the highest gain setting of 70dB. These performance characteristics are sufficient for the μECoG application.
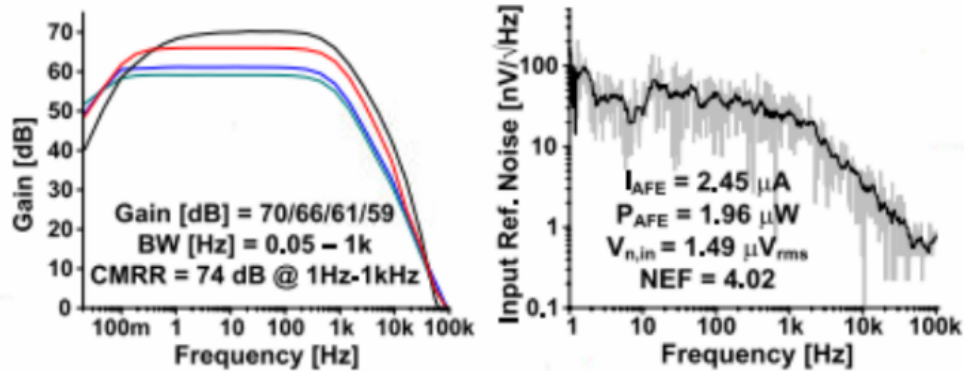
Figure 2.15: ENIAC AFE test results [39] including programmable bandwidth, CMRR, noise, and power consumption
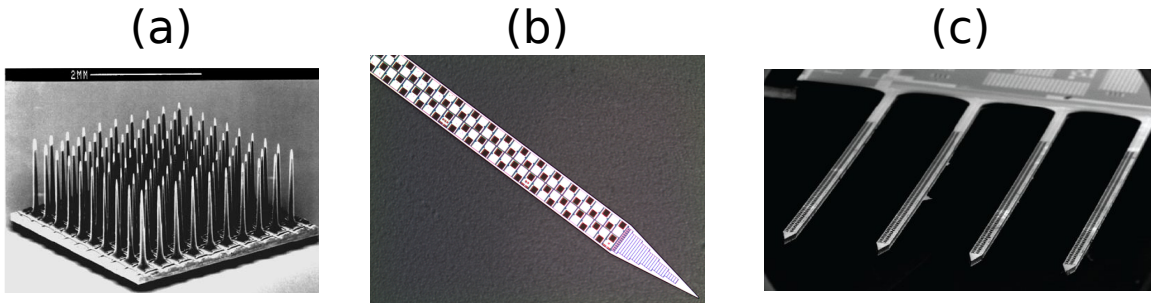
Figure 2.16: Penetrating MEA devices. (a) Utah array (from [58]). (b) Neuropixels (from [44]). (c) SiNAPS multi-shank probe (from [6]).

2.5.4 Neurotechnologies for penetrating electrodes

The above technologies provide for measurement of neural activity in non-invasive (EEG, in-ear EEG) and minimally invasive (ECoG, μECoG) manner. However, many applications require to penetrate neural tissue in order to measure the activity of single neurons or the low frequency oscillations of neural populations as *local field potentials* (LFP). Penetrating electrodes serve this purpose.

One of the most commonly used design is the *Utah array* (Fig. 2.16a) available from

Blackrock (`https://www.blackrockmicro.com/electrode-types/utah-array/`). It includes 100 passive penetrating electrodes that measure the electric potential at their tips. Utah arrays are an excellent source of recordings for Brain-Machine Interface (BMI) applications. BMI applications using Utah arrays implanted in motor cortex were used successfully to enable tetraplegic patients to accurately control 3D robotic arms [49]. The Utah array design makes it particularly suitable for BMI applications, as electrodes cover a relatively large area (2 mm^2), which makes it likely to find neural activity tuned to the task of interest (e.g. neurons tuned to arm/hand movements).

More recently, there has been a large international effort in designing new neural probes to advance research in neuroscience. The design principle of these probes is essentially different than the Utah array design, as neuroscientists are usually interested in recording the simultaneous activity of different brain regions at different depths. Moreover, a higher density of the electrodes is desired, as it facilitates the identification of single neuron activity via spike sorting [10]. The *Neuropixels* probe [55] (Fig. 2.16b – `https://www.neuropixels.org/`) has a single 1 mm-long shank with 960 closely spaced metal electrodes. The electrodes are around 20 μm apart from each other. Up to 384 simultaneous channels can be recorded, and the user can choose from which electrodes to record from. The *SiNAPS* probe [1] has a similar design, with 512 channels with 28 μm spacing which can be record simultaneously at 25 kHz. A newer version of the SiNAPS probe has multiple shanks (Fig. 2.16c) to measure more brain regions simultaneously [6].

These newly developed neural probes are revolutionizing the field of systems neuroscience, enabling high-yield experiments with thousands of recorded neurons across different

regions that were unimaginable only a few years back.

2.6 Acknowledgements

Chapter 3

Maximizing Wireless Power Transfer to Intraocular Implants Under Unconstrained Eye Movements

3.1 Background

Wireless power transfer (WPT) through inductive coupling has become increasingly relevant as a means for charging the batteries of consumer electronics, electric vehicles, and implantable medical devices. As medical implants miniaturize to enable new therapies, there is less and less space for a battery. Novel developments in the field of neural engineering aim to deliver therapeutic and diagnostic function to implants that interface with the brain. Given the proscription of batteries, many of these devices are designed to be constantly powered by an external wearable system through a wireless inductive link [39, 84] (Fig.

2.11).

The eye has been the target of various microelectronic implantable systems attempting to restore vision [42, 51, 88], monitor intraocular pressure in glaucoma [17, 107], and even monitor the body's glucose level [61, 85]. A unique challenge of WPT to the eye is the persistent motion of the ocular globe. There are 3 main types of eye movements: saccades, smooth pursuit movements, and vestibulo-ocular reflexes. These perform different functions in visual tasks. Thus, aside from considering the anatomy of the eye, we must consider the effect of these habitual motions and displacements on the WPT link.

3.2   Design Considerations

3.2.1   Anatomy and Spatial Constraints

Intraocular implants must not affect the natural or remaining function of the eye. So care must be taken to avoid excessive heat from power dissipation, and mechanical damage from poor fitting and mechanical strain to tissues. These considerations are critical in designing the size and location of WPT receiver coil. Although the implant's sensor or actuator system is located inside the eye, the inductive coil can be located intraocularly, periocularly, or even outside the eye. In the first case, intraocular coils can be placed in either the anterior section of the eye, surrounding the crystalline lens, or elsewhere on the surface of the retina. Although intraocular coils do not require a transocular connection to the rest of the implant, the additional bulk and heat inside the eye increase the risk of complications. Periocular coils can be placed around the iris on the cornea, like a

contact lens, or in the temporal subconjunctival space. The temporal extraocular space, has enough room to permit a larger coil sutured to the eye to seamlessly rotate along with eye movements. The temporal location has two main advantages over anterior coil placement: It does not obstruct vision, and power transmission is invariant to pitch (up and down) eye rotations. Finally, inductive coils may be placed at a distant location and tethered with a long, flexible lead to the intraocular space. Although this solution permits for larger coils closer to the surface, the tugging force of the lead during eye movements can distort natural motion and potentially damage the sensitive tissues inside the eye [30]. Figure 3.1 shows a computed tomography axial X-ray image of the space surrounding the eye. The approximate dimensions of the eye and the surrounding orbit are compiled in table [4]. There is significant variability in healthy subjects and due to measurement techniques which can account for $\pm$ 2mm. Given these considerations, the geometry allows for an approximately 10mm diameter, thin or conformal secondary RX coil on the temporal surface of the eye. The primary TX coil can be in alignment at a distance of 23mm from the primary for a 40mm diameter coil.

Table 3.1: Dimensions of the eyeball and orbit [4]

Eyeball	Median	Orbit	Median
Transverse (Right to Left) Diameter	24.24 mm	Width	35.59 mm
Sagittal (Vertical) Diameter	23.78 mm	Height	41.81 mm
Axial (Anterior-Posterior) Diameter	23.49 mm	Depth	48.06 mm
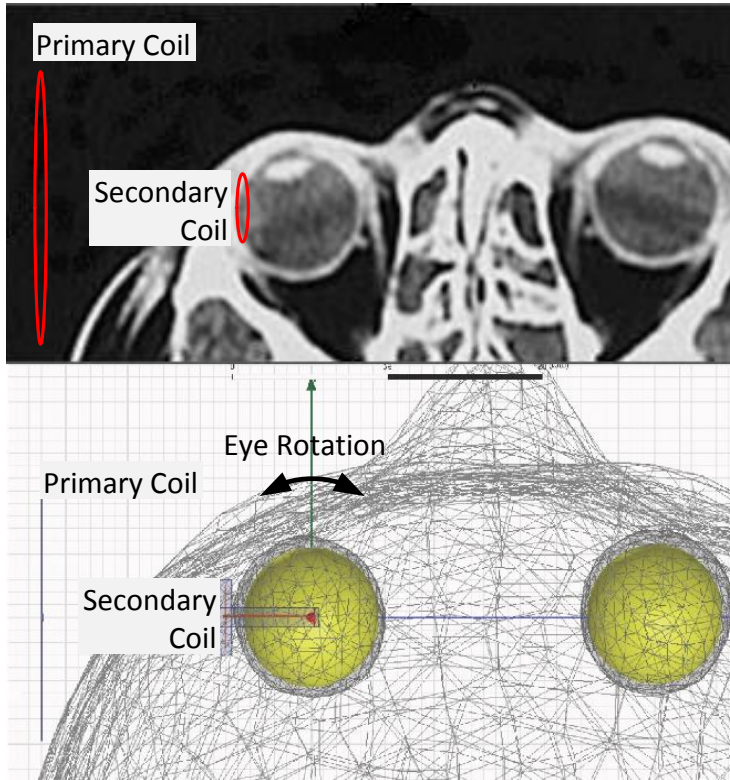
Figure 3.1: Anatomical constraints limiting the size of primary TX coil and implantable secondary RX coil. This axial CT image demonstrates the dimensions of the temporal extraocular space, and a possible location for a transmitter coil.

3.2.2 Theoretical Calculations

Inductive WPT efficiency is mostly determined by the relative geometry of TX and RX coils. In general the closer and larger they are, the higher the coupling coefficient k between the two inductors. Beyond the aforementioned limits to coil size and separation, there is also a practical limit to the ideality properties of an inductor. Because of parasitic resistance and other loss mechanisms a coil is not purely inductive, but contains an element of real impedance. The quality factor , $Q = \frac{\omega L}{R}$, is defined as the ratio of the intended

imaginary impedance over the resulting parasitic real impedance (usually also a function of frequency). Figure 3.2(a) shows a block diagram of the resonant inductive WPT TX and RX systems. Figure 3.2(b) shows a simplified schematic of the inductive link and the relevant components to calculate efficiency. In the transmitter, a waveform generator or power amplifier produces a sinusoidal voltage waveform at our target resonant frequency $\omega_o/2\pi = 13.56$ MHz. At resonance the apparent impedance $Z_{TX}(\omega_o) = R_{TX}$ must be close to R_{SRC} to provide enough power. If this is not the case, a passive matching network must be applied to convert Z_{TX} to Z_{SRC}. The efficiency of power transmission, PTE from V_{IN} to V_{OUT} is given by:

$$PTE = \frac{P_{OUT}}{P_{IN}} = \frac{k^2 Q_{TX} Q_{RX,loaded}}{1 + k^2 Q_{TX} Q_{RX,loaded}} \frac{R_L}{R_L + R_{P,RX}} \tag{3.1}$$

where:

$$Q_{TX} = \frac{\omega L_{TX}}{R_{TX}} \tag{3.2}$$

$$Q_{RX,loaded} = \frac{\omega L_{RX}}{R_{RX}} \frac{R_{P,RX}}{R_L + R_{P,RX}} \tag{3.3}$$

and $R_{R,RX}$ is the effective parallel resistance of the RX coil with the following series to parallel transformation:

$$R_{P,RX} = R_{RX}(Q_{RX}^2 + 1). \tag{3.4}$$

Therefore, the coupling coefficient k can be calculated by experimentally measuring PTE as:

$$k = \sqrt{\frac{PTE}{Q_{TX} Q_{RX,loaded}\left(\frac{R_L}{R_L + R_{P,RX}} - PTE\right)}} \tag{3.5}$$
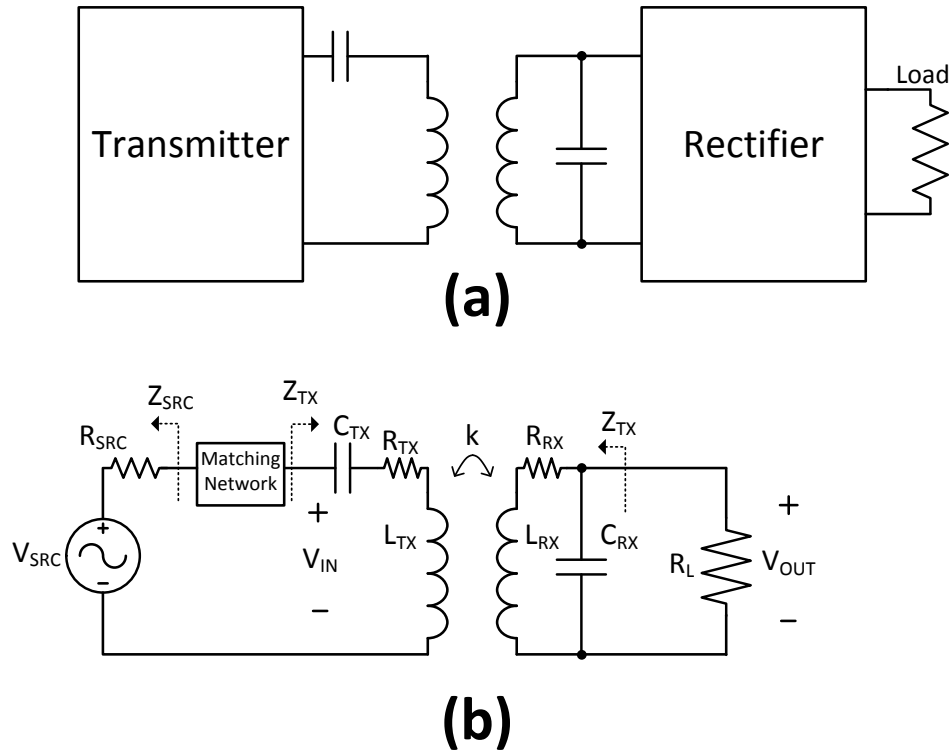
Figure 3.2: **(a)** Basic block diagram of a resonant inductive WPT system. **(b)** Simplified schematic of the WPT circuit to calculate AC power delivery efficiency.

3.2.3   Simulations and Coil Design

3.2.3.1   Simulations

With the constraints from 3.2.1 and the design objectives from section 3.2.2, we designed for a target load of $R_L = 2k\Omega$ as sufficient power to power a retina implant application [42]. In order to optimize the design parameters we used Ansys HFSS FEM simulator software following the procedure outlined in [84] to optimize the unconstrained design parameters to improve efficiency.

Figure 3.3: Primary T_X coil (green PCB) and secondary R_X (gold) coils.

3.2.3.2   Tx and Rx Coil Design

A primary T_X coil for external wearable use, and a secondary R_X coil for periocular implantation have been designed. Size, materials, and geometry selection guided by section 3.2.3.1 and by the surgical requirements for this application (Fig. 3.1).

T_X Coil: The transmitter coil was designed as a printed circuit board (PCB) in order to reduce fabrication costs, improve ease of test assembly, and facilitate connector and matching resonant capacitor interface. Although the area constraint is not as severe as the R_X coil, this T_X coil must still be part of a wearable goggle or glasses type system. Figure 3.3 shows the front side of the PCB T_X coil. The 9-turn coil has outer diameter 4 cm and

its traces are 2 $oz/ft^2 Cu$.

R_X Coil: The receiver coil was designed with feedback from surgeons as to the plausible implantable area. A diameter of 1.0 cm would not obstruct regular movement and could be affixed temporally. The implantable R_X coil was implemented as 5-turn polymer-insulated gold wirewound spiral inductor. Figure 3.3 shows the periocular coil overlayed on the PCB coil.

3.2.3.3   Matching Network

The matching network mentioned on section 3.2.2 is responsible for matching Z_{TX} to Z_{SRC} in order to maximize power transfer. Without a matching network, the value of V_{SRC} setting required to drive R_L to the desired voltage could be prohibitively high and very energy inefficient. An L-type matching network composed of passive reactive components can adapt the expected value of Z_{TX} to effectively match the output impedance of the driver or signal generator Z_{SRC} which is commonly 50Ω. Figure 3.4 shows the schematic of the L-type matching network along with the graphical representation of the impedance transformation in a Smith chart.

3.3   Experimental Results

In order to validate the design we must measure all the unknowns in Eqn. (3.1), as well as PTE itself. The link tuning/validation procedure followed was: (1) Characterize each coil in isolation; (2) Solder the appropriate resonant capacitor and verify resonance.

(3) Assemble the wireless test frame, measure PTE while varying link parameters. (4) Verify and tune matching network.

3.3.1 Experimental Setup

3.3.1.1 Coil Characterization and Tuning

Measurement of individual coil properties was performed with a vector network analyzer (VNA) (Agilent E5071C). After electronic calibration, 1-port manual calibration function was used to de-embed the effect of the wires, PCB, and connectors leading up to the wirewound and printed circuit coils. A measurement of S_{11} was taken with a frequency sweep including the relevant $13.56MHz$ point. After computing the inductance of the coil, a resonant SMT capacitance of $C = 1/(4\pi^2 f^2 L)$ is soldered as close to the coil mounting pads as possible. Given the difficulty in procuring arbitrary magnitude of capacitors, 2 pads were laid out to improve matching by using 2 capacitors and measuring again after soldering the first one. At 13.56MHz, the S_{11} measurement should show a low impedance for the series resonant T_X coil and higher impedance for the parallel resonant R_X coil. These correspond to the values R_{TX} and $R_{P,RX}$ respectively.

3.3.1.2 Wireless Test Frame

A 3D printed fixture was custom made for this experiment, fabricated with all polymer components. The fixture can control the relative separation and alignment of the coils in order to simulate the anatomical scenario. Figure 3.5 shows the wireless test

frame used to characterize the link. The PCB coil is mounted on a 3-axis stage where the

axial distance $\hat{z}$, and the lateral misalignments $\hat{x}$ and $\hat{y}$ can be manipulated. Additionally,

the implantable secondary coil hangs from the edge of a small PCB and is centered and

fastened on the side of a spherical surface with radius 13mm. The secondary coil holder

can be rotated along the central axis of the sphere simulating the *yaw* angle of the eye $\hat{\phi}$.

Calibrated rulers quantify all 4 dimensions.

3.3.1.3   Link Characterization Procedure

Characterization of the link efficiency was done with a simplified circuit similar to

Figure 3.2(**b**). As we are interested in measuring the PTE of the link we can remove the

matching network and connect the VNA directly to the V_{IN} terminal in order to measure

input power through S_{11}. To measure output power we used an oscilloscope with a high

impedance active probe to measure the voltage V_{OUT} across R_L. An alternative way to

measure PTE is removing R_L and doing a 2-port measurement with all the S-parameters

$\left(\begin{smallmatrix} S_{11} & S_{12} \\ S_{21} & S_{22} \end{smallmatrix} \right)$. In the first method PTE is measured for the exact secondary loading conditions

reflected back on the link (with the exception of probe parasitics), while on the second

method the output is connected to the 50Ω terminal of the VNA's second port. Thus, the

2-port measurement requires additional calculation and suffers from reduced precision from

cascaded mismatching.
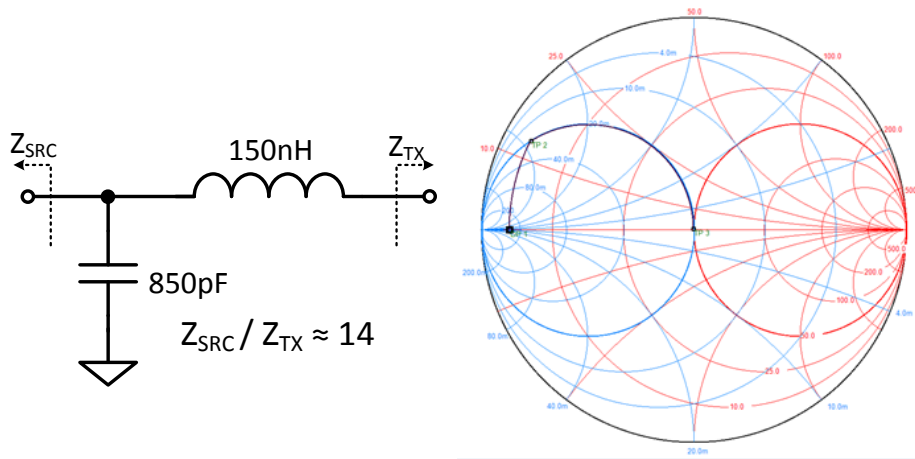
Figure 3.4: Schematic of L-shaped matching network and corresponding Smith chart.
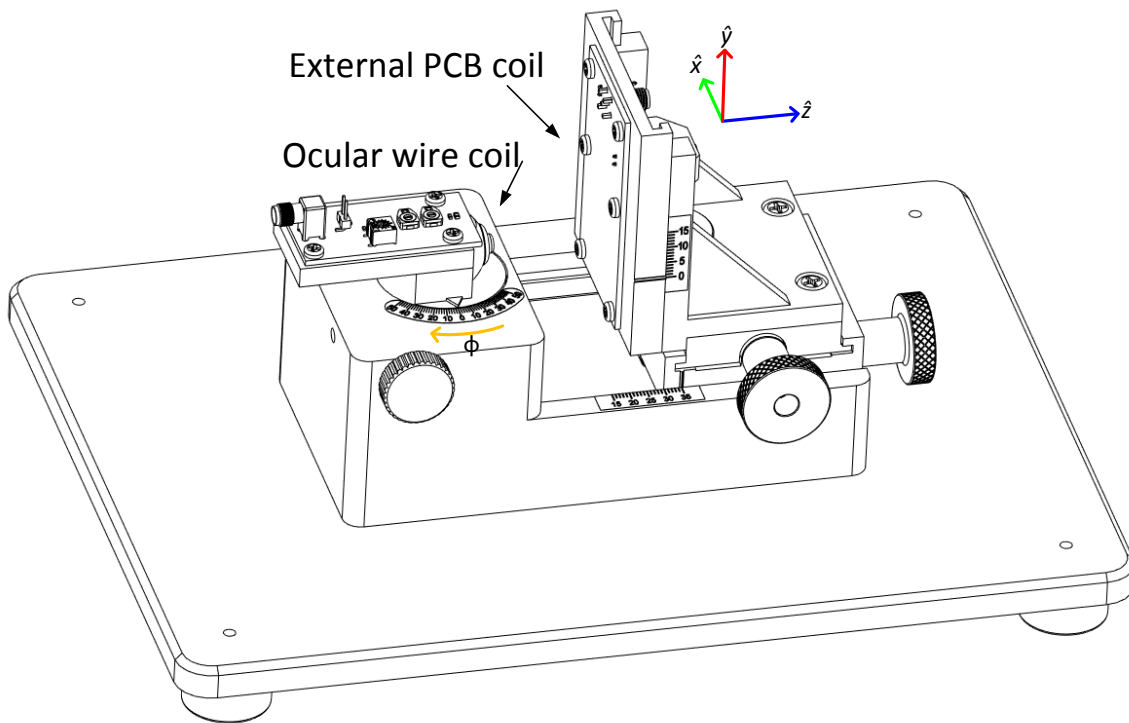
Figure 3.5: 3D printed test frame to control relative position of the proposed coils. The test frame allows for independent control of $\hat{x}$, $\hat{y}$, and $\hat{z}$ positioning of the primary coil, as well as $\hat{\phi}$ the angular rotation of the the secondary coil.

3.3.2 Individual Coil Measurement

Figure 3.6 shows the results of the 1-port measurement of individual coil complex impedances for T_X and R_X coils. Aside from the required values, we note coils' the self resonant frequency (SRF) to determine their useful frequency range. The T_X coil has $Q_{TX}(\omega_o) = 53.4$, $L_{TX}(\omega_o) = 1.75\mu H$, $R_{TX}(\omega_o) = 2.79\Omega$ and $SRF = 75MHz$. The R_X coil has $Q_{RX}(\omega_o) = 43.2$, $L_{TX}(\omega_o) = 492nH$, $R_{TX}(\omega_o) = 0.97\Omega$ and $SRF > 100MHz$. These values match expected results from simulation. The SRFs are sufficiently higher than $13.56MHz$ to avoid significant deviation. Tuning of the individual resonators was accomplished through soldering and with the assistance of screw-tunable variable capacitors.

3.3.3 Power Transfer Measurements

Characterization of PTE at various link settings requires measurement of the input power and the output power as shown in Eqn. (3.1). The maximum power output of the VNA was verified by terminating the connector with an ideal 50Ω load, obtaining $10dBm$. Figure 3.7(a) shows the PTE for the link in perfect parallel and angular alignment as the axial distance between primary and secondary coils is varied. $10mm$ is the minimum possible anatomically realistic distance in temporal side trans-orbital coupling. In contrast, $35mm$ is a likely upper bound for a wearable coil. The PTE efficiency ranges between $9\% - 36\%$ with a nominal value of 25% at the nominal distance of 23%. Transmission through a $10mm$ layer of porcine muscle does produces a minor change in PTE. Figure 3.7(b) explores the effect of parallel misalignment of the coils across $15mm$ in only one
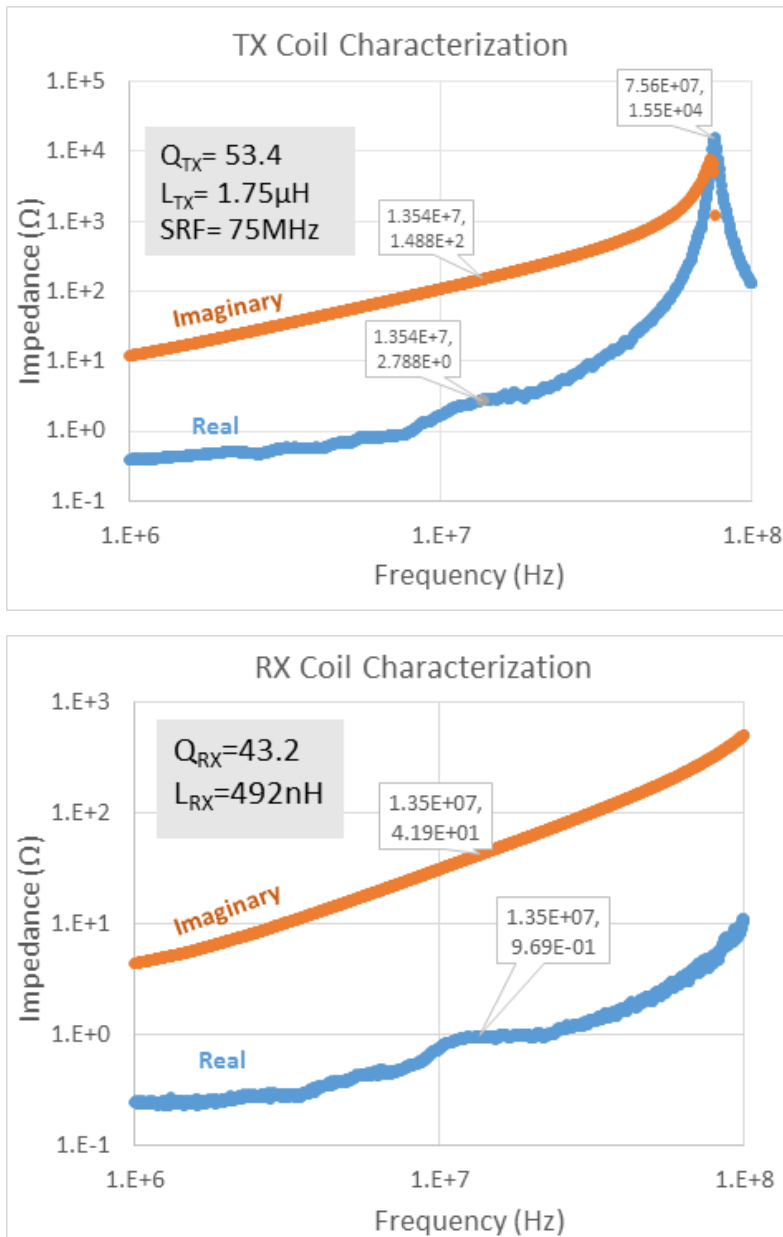
Figure 3.6: Characterization of TX and RX coils. Inductance L, quality factor Q, and self resonance frequency SRF are calculated.

direction at nominal axial distance. The rate of decay of PTE accelerates after the coil displacement is greater than the diameter of the secondary coil. Biological tissue also causes a minor loss in power. Additionally, the effect of 'eye' rotation on PTE is shown in Figure 3.7(c) for a maximum unidirectional yaw of 50° at nominal axial distance. The angle has a strong effect on PTE after passing 10° misalignment. At this distance, 50° rotation of the eye results in an 80% decrease in power transfer. The relative energy loss to biological tissue is comparable to the minor losses in the previous scenarios. Finally, the relation between PTE and the coupling coefficient k for this system (3.5) is shown in Figure 3.7(d). Hence this establishes the equivalent k for each distance, misalignment, or rotation of interest.

In future work we plan to demonstrate strategies to mitigate the effect of link uncertainty and variability on the functionality of intraocular implants. One such strategy is described in section 4.2.4.3 as part of an integrated microsystem for wirelessly powering and controlling a retina implant.

The design principles for the coil inductive link presented in this chapter set the stage for the development of a highly energy-efficient integrated circuit providing power conversion at minimum losses, along with waveform control for stimulation. The design of this integrated circuit is presented next.
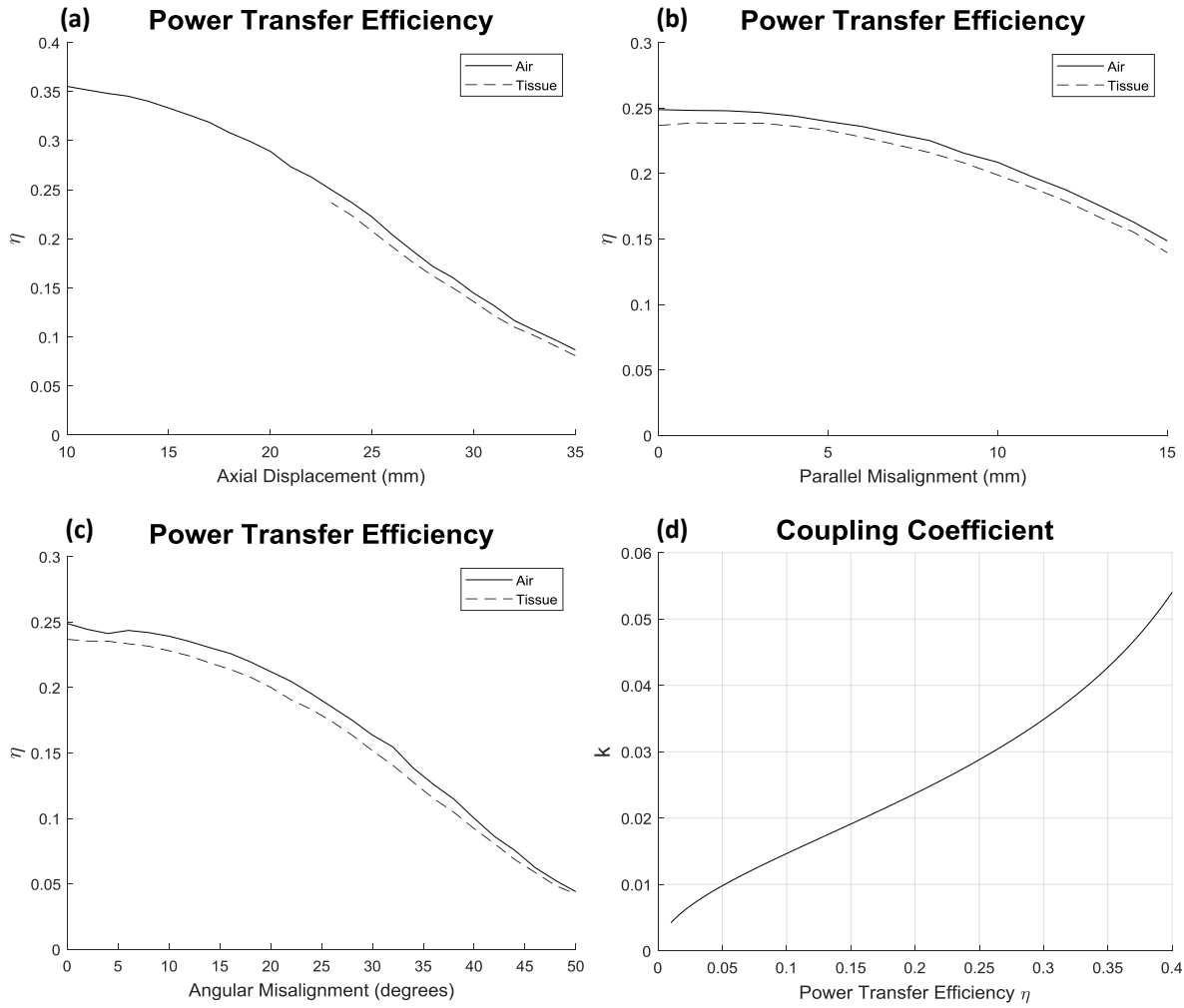
Figure 3.7: Power transfer efficiency across the wireless link as a function of: **(a)** axial displacement, **(b)** parallel misalignment, and **(c)** angular misalignment. **(d)** Shows the equivalent coupling coefficient which produced the measured PTE

3.4 Acknowledgements

Chapter 3 is largely a preprint of material being prepared for publication by Abraham Akinin, Jeremy M. Ford, Jiajia Wu, Hiren Thacker, Jiwoong Park, Patrick Mercier, and Gert Cauwenberghs. The dissertation author is the primary author and investigator of this work.

Chapter 4

Energy-Efficient RF Powered

Charge-Balanced Electrical Stimulation

4.1 Background

Neurostimulators are a kind of implantable medical devices that have achieved very successful clinical implementation in the past decades. In general they provide voltage or current pulses to electrically activate tissue in order to stimulate or suppress nerve function. Among the achievements of this technology are restoring sensory function to patients with damaged hearing, reducing the severity of tremors, treating depression, and rehabilitating voluntary motion of muscles and sphincters. Almost all of these devices require implantation in a miniaturized, hermetic, and biocompatible enclosure in order to fit into the limited space available in the surroundings of the brain or the target nerve tissue. Given the importance and sensitivity of these tissues neurostimulators must operate

73

at very high power efficiency to avoid heat damage. Another important requirement of neurostimulation is charged balanced stimulation. Neurostimulators provide electrical pulses to neural tissue through specialized electrodes. As current crosses the electrode-electrolyte interface, different kinds of physical and chemical processes occur. A constant unidirectional current applied on this interface may eventually cause irreversible chemical processes that destroy the electrode and generate harmful chemical compounds that result in tissue damage. This effect also occurs in stimulators that present biphasic electrical waveforms as stimulus, but with non-zero net charge. Over time, accumulated charge imbalances can lead to the aforementioned undesirable effects.

Retinal prostheses are a kind of neural stimulator that aims to restore vision to blind patients. At this moment, retinal prostheses have not had the same clinical success as cochlear stimulators have in restoring hearing to deaf patients. The retinal prosthesis strategy generally involves electrical stimulation of the remaining retinal tissue, in the case of patients with a diseased retinal photoreceptor cells, to elicit light perception. There is a direct relationship between the geometrical characteristics of retina stimulation and the perceived shape of the perceived visual image. Thus, retinal prostheses aim to provide as many channels of stimulation as possible, in order to approximate healthy vision which can perceive high resolution 2D images. This presents a problem to the requirements of implantable neurostimulators, as a conventional high channel count neurostimulator would: generate too much heat through inefficient stimulation and high data rate video transmission; require very bulky interconnect to control so many channels; and cause tissue damage and reduced electrode lifetime due to charge unbalanced stimulation.

Recently, we introduced a practical alternative approach toward reducing the number of interconnect channels while maintaining effective high resolution stimulation, that uses a dual-purpose electrode and photosensor array placed under the retina for optically addressed, electrically activated stimulation [42]. The array of photo-sensors is globally biased with a voltage pulse using only two wires and produces currents from each electrode/pixel proportional to the amount of incident light. Figure 4.1 summarizes the results of our previous effort. In figure 4.1**(a)** the light-dependent current output from the electrode array is demonstrated. A wireless power demodulation system for direct inductive driving of the electrodes is shown in figure 4.1**(b)**. Additionally, figure 4.1**(c)** & **(d)** show an experimental setup for *ex vivo* validation on neurodegenerative blind rat retina along with results demonstrating neural activation. This chapter addresses the challenge of powering and controlling this system wirelessly while minimizing power losses, a challenge that has not been met with previously reported RF-powered stimulation systems. Our solution, presented below, is the development of an integrated circuit that efficiently powers and controls optically modulated multichannel stimulating arrays with minimal interconnect and charge balanced outputs.

4.2   System Description

Efficiently transmitting power and control data to an inductively powered neurostimulator can be accomplished by outsourcing many of the power intensive tasks out of the implant and into the external power system where there is more space to implement energy
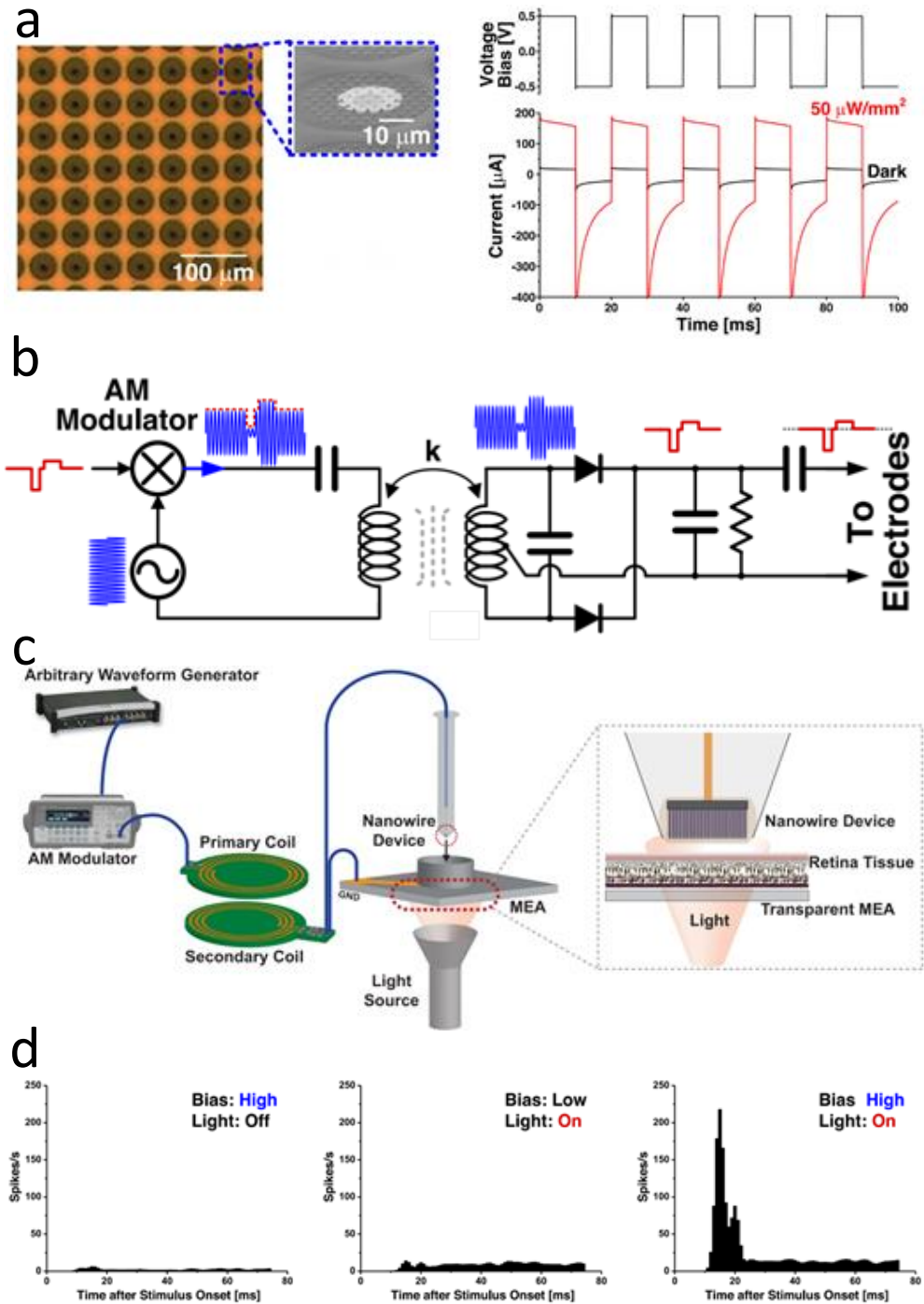
Figure 4.1: Previous developments in our retina prosthesis system [42] including nano-engineered sensor-electrodes **(a)**, wireless power transmission system to drive the electrodes **(b)**, experimental setup **(c)**, and *ex vivo* results **(d)**.
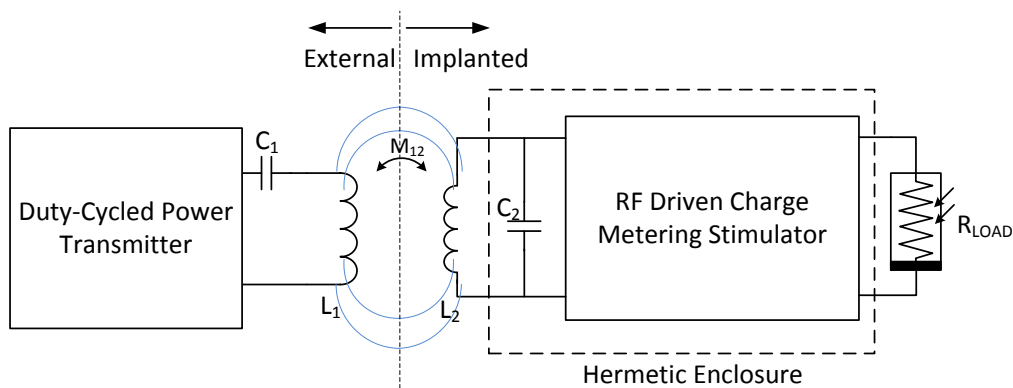
Figure 4.2: Adiabatic RF-driven charge-metering stimulator driving a load in an implant inductively coupled to an external duty-cycled power transmitter.

efficient solutions, and heat from wasted power does not result in tissue damage. Figure 4.2 shows the system concept. The first solution is to create a system that is only powered during the time it is required to output a pulse. Therefore we can build a duty cycled transmitter which powers the device dynamically as needed to produce pulses. This duty cycled power, is not only saving energy during the off-time of the pulse, but effectively time encoding the pulse width data into the power signal duty cycle; obviating the need to transmit, decode and process this data. The external duty cycled power supply is inductively coupled to the implant, which is an RF driven charge metering stimulator. The stimulator is in turn connected to the electrode array and reference ground electrode using only two wires. To the charge metering stimulator, the electrode array is electrically equivalent to a single non-linear photosensitive load impedance, so knowledge of the output voltage is not sufficient to enforce charge balanced stimulation.

An overview of the architecture of the RF driven charge metering stimulator is
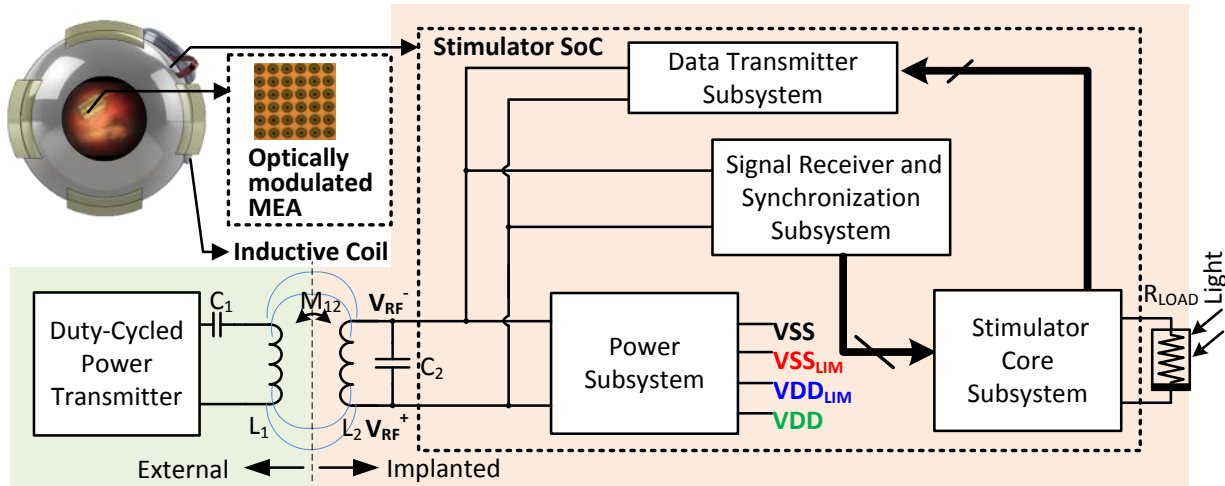
Figure 4.3: The RF driven charge metering stimulator, with power subsystem, signal receiver and synchronization subsystem, stimulator subsystem, and data transmitter subsystem.

shown in the diagram of Figure 4.3. The system designed to exemplify the implanted neurostimulator consists of 4 major subsystems: Power, Data Receiver and Synchronization, Stimulator Core, and Data Transmitter. Each of these blocks has been designed with the principle of delegating functions to the external system in order to save power. As the systems have very different functions, different strategies contribute to overall novelty and efficiency.

4.2.1 Power Subsystem

In order to control the amplitude of a stimulating pulse, a stimulator system can either have a variable power supply rail or make use of digital to analog converters. Power conversion in conventional neurostimulators, and many other electronic systems, usually requires the use of DC-DC converters. These converters require large capacitors, and sometimes even larger inductors to achieve high efficiency. This property makes them
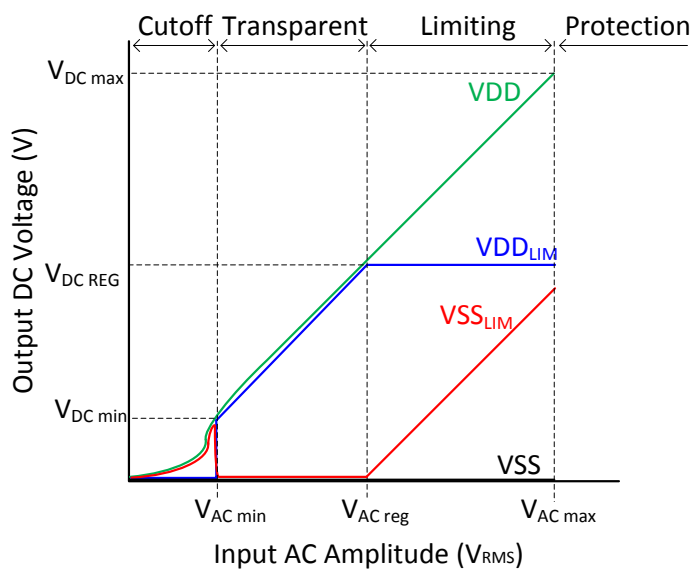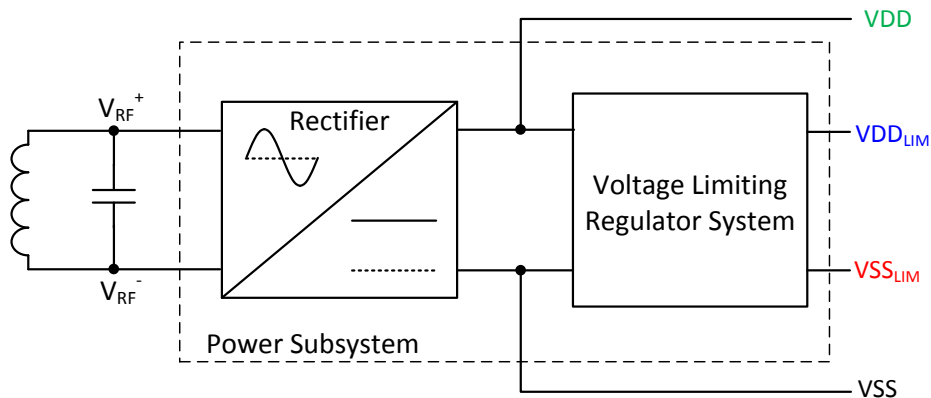
Figure 4.4: The power subsystem, and its regions of operation in rectifying and regulating the AC RF input into output DC voltages.

undesirable in miniature implants where space is a significant constraint. Additionally, DC-DC converters usually convert a fixed ratio of voltages. Alternatively variable regulators or other digital to analog converters can generate any desired voltage level lower than a maximum constant power supply. This second approach is even more wasteful, as the system must maintain a high voltage supply even as it outputs low voltage, usually

completely wasting the difference in power.

The stimulating output pulse amplitude is controlled by the external power system. During the duty cycled power, the implanted system has an AC-DC converter, or rectifier, that can operate in a broad range of AC voltage amplitude. The received RF energy is rectified with low losses, and low voltage drops to produce the system's unregulated power supply. This unregulated voltage, will be directly connected to the load avoiding regulators and other intermediate steps and energy costs. By increasing, or decreasing the amplitude of the external transmitter we can directly control the output voltage of the stimulator. The cost of this energy savings is that the rectifier, and the rest of the system's circuits must operate correctly at a wide range of voltage supply levels. So not only does this method save energy by avoiding voltage conversion losses, but it also saves energy by obviating the need for amplitude data transmission, detection and processing. This power strategy is described in Figure 4.4. For practical implementation of this system, not all integrated circuit processes have a wide supply range. Therefore, it is also necessary to generate low-power consuming regulated supplies in order to protect thinner gate transistors required for high speed digital and well performing analog circuits. Even though we used linear regulators to limit the analog and digital power at the high end of the RF levels, these do not significantly affect total system efficiency, as most of the power consumed by the system is taken from the unregulated supply to drive the load. A schematic calculation of the advantageous reduction in power consumption is shown in Figure 4.5. A further illustration of the possible power savings is shown in Figure 4.6. For the same load power, a current DAC stimulator results in significantly higher power consumption for all parts of

Current DAC Stimulator

TX Controller — PA — Rectifier — LDO — Aux FUNC / DAC — R_{LOAD}

$$\eta_{TOT} = \eta_{PA} \cdot \eta_{LINK} \cdot \eta_{Rec} \cdot \eta_{LDO} \cdot \eta_{DAC}$$
$$P_{TOT} = P_{LOAD} / \eta_{TOT} + P_{AUX} \cdot \eta_{DAC} / \eta_{TOT}$$

Adiabatic Pulse Gen — This Work

Aux FUNC — TX Controller — PA — Rectifier — R_{LOAD}

$$\eta_{TOT} = \eta_{PA} \cdot \eta_{LINK} \cdot \eta_{Rec}$$
$$P_{TOT} = P_{LOAD} / \eta_{TOT} + P_{AUX}$$
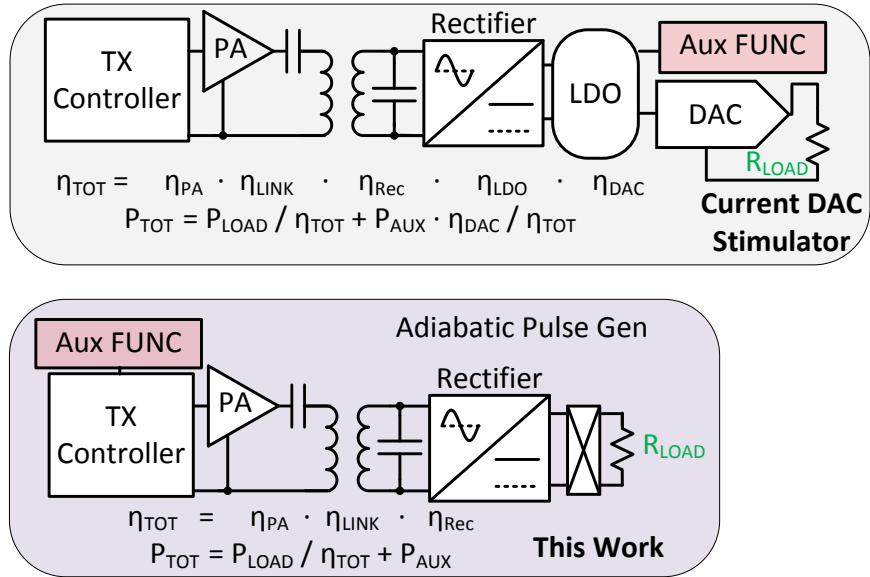
Figure 4.5: Adiabatic power savings across the entire system. Outsourcing of non-stimulating auxiliary functions to the external system results in multiplicative power efficiency improvement.

the implant. The blue arrows highlight the effect of unregulated stimulation and overhead outsourcing. As demonstrated, the multiplied power savings do not only decrease total power, but also heat in the implant, RF tissue absorption, and wearable transmitter.

4.2.1.1 Rectifier

In order to accomplish the power savings and architecture simplifications that result from the aforementioned strategy, the architecture of the rectifier must maximize power conversion efficiency and voltage conversion ratio over a wide range of input and output conditions. While there exist many architectures, they are usually optimized for a single load or voltage condition. The proposed rectifier manages very low conductive losses by a
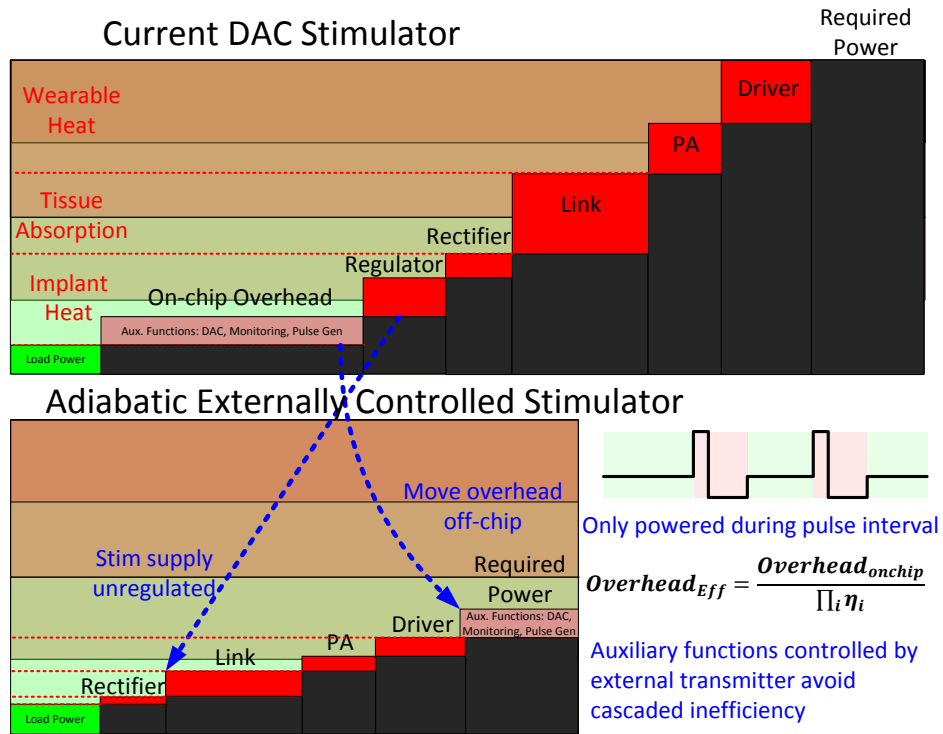
Figure 4.6: Illustration of the power efficiency gains from unregulated adiabatic external control, outsourcing of auxiliary functions, and duty cycling of the power transmitter. Because of multiplied inefficiencies, the total required power for a typical current DAC stimulator is significantly higher, resulting in more implant heat, more RF energy tissue absorption, and more heat production at the wearable external transmitter.

combination of fully cross-coupled complementary PMOS and NMOS pairs. Additionally, a native NMOS, or near-zero threshold device, is inserted to reduce the reverse current when $V_{RF+} - V_{RF-} > 0$ but $V_{RF+} < V_{DD}$. Figure 4.7 shows the architecture of the rectifier. This design improves on an existing method by only using one type of native transistor (n-type in this case), eliminating the redundant reverse current protection which reduces voltage drop, and making the design possible in a wider array of semiconductor processes that don't have complementary native devices. The proposed rectifier also has the advantage to switch itself with the existing RF sinusoid, obviating the need for comparators, phase detectors,
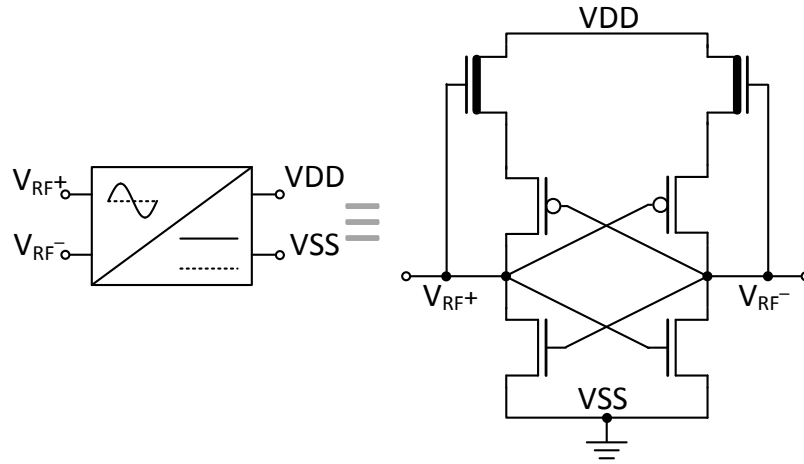
Figure 4.7: Rectifier in the power subsystem.

and phased locked loops usually present in active-rectifiers. These three mixed signal blocks require significant design effort, greatly increase power overhead, and generally must be optimized for a narrow range of operating voltage and frequency. Therefore this rectifier presents significant improvement over previous strategies as it has low power consumption overhead, and its wide operability can enable external transmitter control of stimulation amplitude.

4.2.1.2   Dual Complementary Regulators

Many semiconductor processes provide higher-voltage-tolerant transistors as well as smaller, faster, standard transistors useful for high performance analog and digital operations. In this design, both kinds are harnessed to extend the functional range. In order to execute the power strategy proposed in Figure 4.4, we require regulation of the
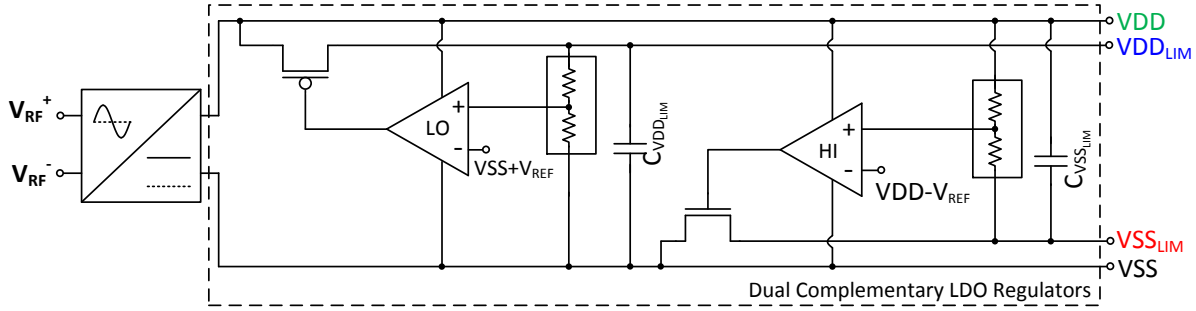
Figure 4.8: Dual supply complementary voltage limiting regulator, interfacing to the rectifier in the power subsystem.

main power supply VDD. As the goal is to make secondary supplies that will not destroy the low-voltage devices, we require a limited voltage supply with respect to ground VSS, as well as another limited voltage with respect to VDD. In order to accomplish this we have designed a dual complementary low dropout regulator to limit both supply rails. The regulator architecture, shown in Figure 4.8, has 3 main regions of operation shown in Figure 4.4: cutoff, transparent, and limiting. In the Cutoff region, the unregulated voltage VDD is too low to power the error amplifiers that control the pass transistors, thus the regulated supplies are turned off if VDD is less than $V_{DC\ min}$. In the Transparent region, the regulators turn on the pass transistor such that the regulated supplies are almost the same amplitude as the unregulated supplies (except for the dropout voltage across the pass transistors). In the Limiting region, when VDD exceeds the safe limit of the low-voltage transistors, $V_{DC\ REG}$ the error amplifiers decrease the conductivity of the NMOS and PMOS pass transistors to maintain VDD_{LIM} at $V_{DC\ REG}$ and $VDD - V_{SS\ LIM}$ at $V_{DC\ REG}$. Finally, a fourth region exists where overvoltage Protection prevents breakdown

of all circuits above V_{ACmax} max. This design improves on existing regulator architectures in that the error amplifiers, driven by the unregulated supply as a power source, default to complementary high (HI), and low (LO) voltages when the supply is insufficient to operate the amplifier correctly. The one possible architecture for the complementary error amplifiers is shown in Figure 4.9. The use of complementary-defaulting-to-rail architectures is what enables the operation of the regulator at lower VDD voltages and thus decreasing $V_{DC\ min}$ and correspondingly $V_{AC\ min}$. This allows the permissible output voltage range of the stimulator to span $[V_{DC\ min}, V_{DC\ max}]$, while utilizing the advantages of both high voltage and low voltage transistors.

4.2.2 Data Subsystem

The signal receiver and synchronization subsystem consists of a downlink telemetry receiver, clock recovery circuit, power-on reset circuit, and system state machine. Its purpose is to receive data signals from the external controller, recover a clock of the same frequency as the carrier wave, and setup the correct sequence of calibration and stimulation. As part of the strategy to reduce the amount of operations on the implantable system, the only data transmitted downlink is a single bit asynchronous, time encoded, amplitude modulated pulse signaling a change in the stimulation phase. As described previously, the amplitude of the stimulation waveform and the duration of the stimulation waveform are analog encoded on the RF signal by the external transmitter, to minimize power dissipation and operational complexity in the implant.
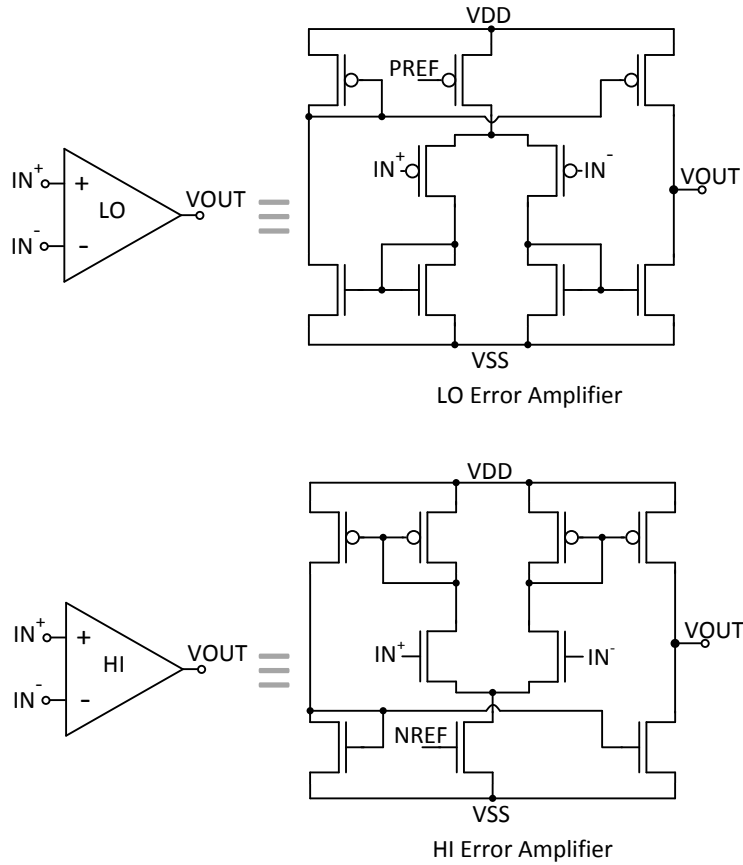
Figure 4.9: The low-ranging (LO) and high-ranging (HI) error amplifiers in the voltage limiting regulator.

4.2.2.1   Data Receiver

In order to receive the phase-changing data pulses the amplitude modulated RF wave must be demodulated. In this system we propose a strategy for demodulation that involves the proposed rectifier described in Figure 4.7. The system diagram of the downlink data receiver is depicted on Figure 4.10. As the proposed rectifier is an efficient, wide input range circuit, the same architecture can be applied toward demodulating the RF
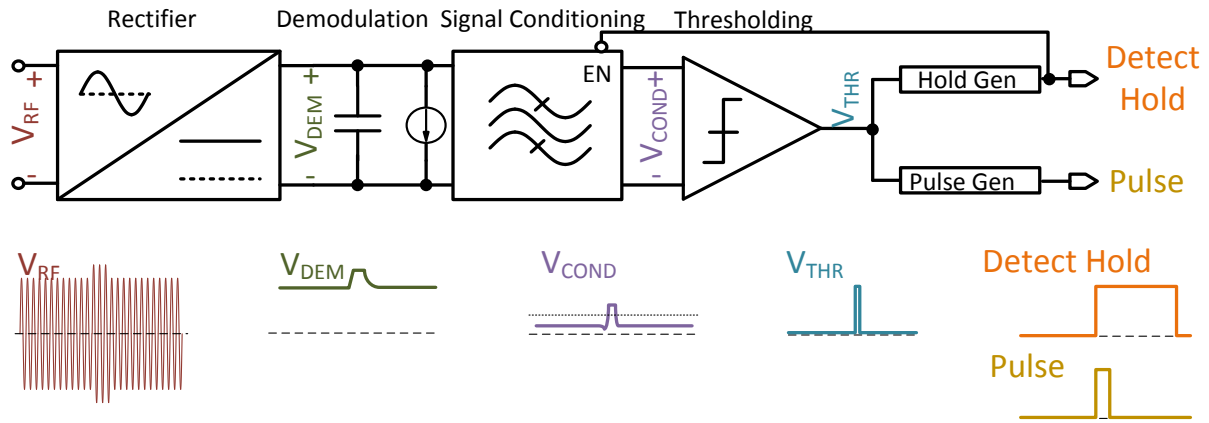
Figure 4.10: Signal receiver and synchronization subsystem, with example waveforms for generation of the Pulse and Detect Hold signals from the RF input.

signal envelope. In order to minimize power syphoned away from the rectifier system, this auxiliary rectifier is many times narrower than the primary power rectifier, as it needs to drive a much smaller load. After the signal demodulating rectifier, the signal encounters an integrating capacitor and a current sink that permits the demodulated voltage to decrease after the modulated signal pulse is over. Subsequently a mixed signal active bandpass filter conditions the signal to enhance the pulse. After the bandpass filter, a real time comparator detects threshold crossing pulses. When a pulse is detected a circuit, Pulse Gen, generates a digital pulse signal of a standard duration, while another circuit, Hold Gen, generates a much longer hold signal that digitally resets the bandpass filter and prevents any duplicate events from detection for a refractory period.

4.2.3 Stimulator Subsystem

Figure 4.11 shows the stimulator subsystem. The stimulator provides a voltage pulse waveform by directly connecting the duty-cycled and amplitude modulated supply
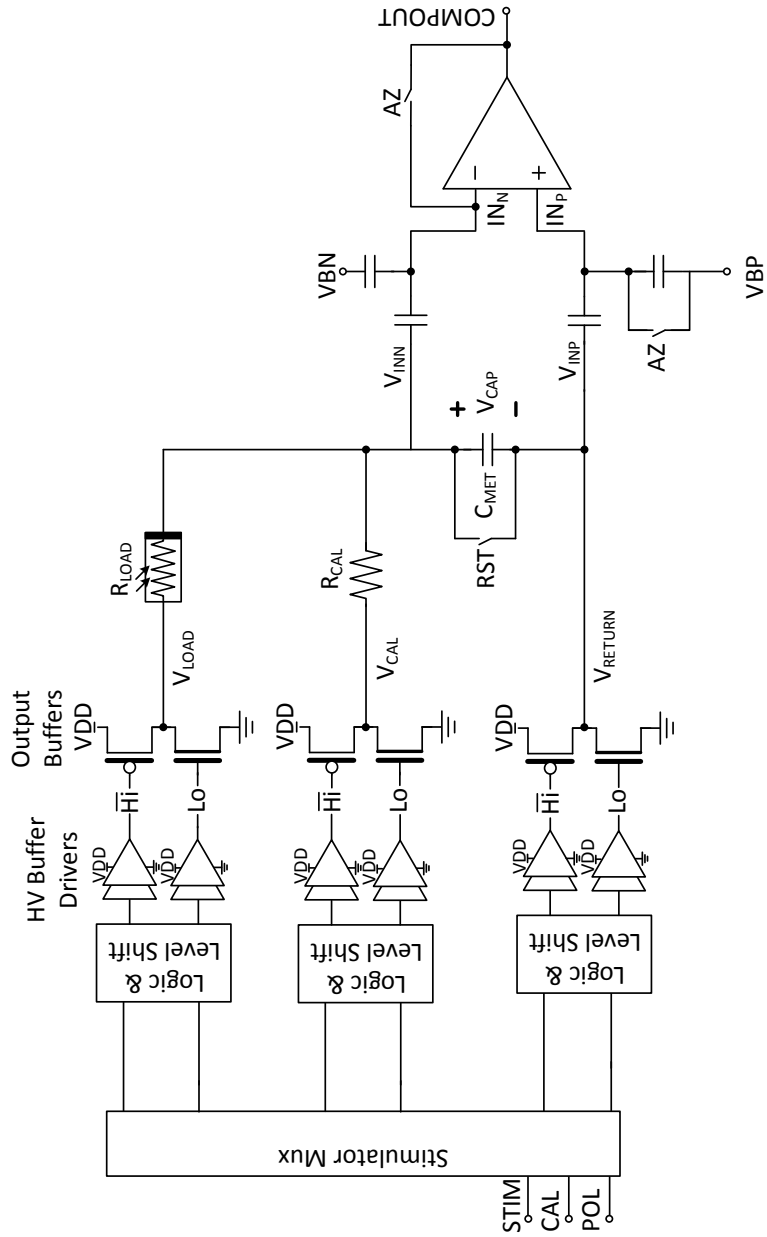
Figure 4.11: Stimulator core subsystem for adiabatic voltage stimulation and charge metering.

VDD to the desired load. To this end, the stimulator relies on 3 tri-state switches, or Output Buffers, that can connect each terminal of either the intended load, or a known calibration resistor to VDD or VSS. As the current flows through the load R_{LOAD}, metering capacitor C_{MET}, begins charging until it reaches a set differential voltage threshold, at which point the comparator monitoring this voltage activates a reset switch to discharge the capacitor. Each time there is a discharge event, an amount of charge $Q = C_{MET} V_{thresh}$. Therefore this stimulator outputs an analog voltage of arbitrary amplitude to drive a load of unknown impedance while outputting digital counts of the delivered charge. This method conserves a lot of power, and prevents complexity and error in the system compared to a series transimpedance amplifier or series resistor current measurement. A transimpedance amplifier is impractical as currents of the order of miliamperes would need to be driven through an operational amplifier at great cost in headroom power. Similarly, a series resistor current measurement would require a precise, linear, high bandwidth amplifier, and an accurate analog to digital converter to quantize the current followed by digital integration to calculate total charge. Instead, the proposed system is not only simpler and more power efficient, but the charge quantization signals may be directly used to send backtelemetry events to the external system.

4.2.3.1   Output Buffers

The switches in the Output Buffers are designed to have very low impedance in order to reduce power consumption and voltage drop across them. They also have to be built to withstand the full range of stimulation voltage, and so in this implementation

they are designed to use high voltage tolerant IO transistors. In order to have both low impedance, especially at very low voltages, and tolerate high voltages, the switches were sized considerably large in relation with the rest of the system. Although the area occupied by the switches is significant, it is an acceptable trade-off for the large range of operation of the stimulator which is approximately [0.5-3V] in the implemented process, but may be significantly higher in processes with higher voltage tolerant devices. The output buffers are preceded by HV Buffer Drivers, output multiplexor logic, and voltage level shifters.

4.2.3.2 Charge Metering

Although the output buffers and corresponding drivers are implemented with high voltage tolerant devices, the rest of the stimulator is entirely composed of standard gate thickness low voltage devices, for size speed, and threshold voltage considerations. In order to operate in potentially breakdown inducing conditions, several strategies were taken to protect the circuits while utilizing the advantages of the standard devices.

The comparator required to detect whether C_{MET} has exceeded the desired threshold voltage is capacitively coupled preventing DC overvoltage. This capacitive coupling is also advantageous to apply a differential bias through VBN VBP. In this way the comparator acts like an open loop difference differential amplifier. The comparator also has the capability to perform an auto-zero cycle to eliminate intrinsic offsets and set the otherwise-floating input voltage operating point.

4.2.3.3 Metering Reset Switch

Another critical component of the stimulator is the reset switch RST. A diagram describing these switches and supporting structures is shown in Figure 4.12. As switching must be fast and efficient, low voltage standard devices must be used. In order to prevent overvoltage at the reset switch several strategies are applied. First the NMOS reset switch is isolated through triple well, and as usual the PMOS switch is implemented in its own n-well. Second, the comparator prevents the source drain voltage from exceeding a set threshold. Third the high speed drivers required to switch the reset switches on and off are powered by a muxed power supply. For example, in the positive current phase, if VDD exceeds $V_{DC\ REG}$, the RST's NMOS transistor driver is driven with VDD_{LIM}. Conversely, in the reverse current phase when the switch terminal V_{RETURN} is connected to VDD, the RST's PMOS is driven with VSS_{LIM} as a low supply rail. To make this possible logic circuits, a power rail selector mux, and dual rail level shifters (level translators) are implemented on the drivers. The drivers are sized for maximum speed of reset using the principles of logic effort sizing.

4.2.3.4 Timing of Charge Metering

A description of the signals involved in the adiabatic charge metering stimulator are represented in Figure 4.13. As the unregulated supply voltage VDD charges up to V_{HI} at the beginning of a duty cycled pulse the comparator undergoes autozero and the state machine is reset. Thereafter, VDD is connected to the load providing positive V_{HI} of voltage across the load terminals. During this time the metering capacitor charges
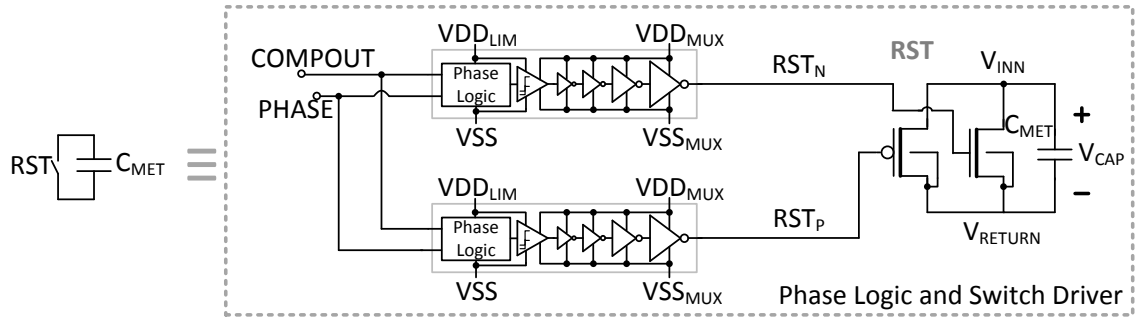
Figure 4.12: Phase logic and switch driver for reset of the metering capacitor in the stimulator core subsystem.

and discharges as the comparator input reaches threshold. The voltage excursion of the metering capacitor causes a triangle ripple voltage across the applied load voltage. However, considering it is desirable for the reset threshold to be low, and the switching frequency to be much higher than the stimulation (pulse repetition) frequency; it will not affect the performance of this system as a neurostimulator. For each charge quantum completed, there is an immediate backtelemetry event pulse. When the first phase is complete the external system sends an upmodulated pulse to signal a phase change, and the amplitude of the RF signal is immediately decreased to change VDD to V_{LO}. After a brief autozero period, the stimulator turns on applying a negative V_{LO} voltage across the same terminals mentioned above. Similarly, charge quanta cause resets, which in turn are transmitted back to the external system. Enforcing the reverse phase duration to contain the same number of charge quanta as the first, in other words charge balance, can simply be done from the external system.
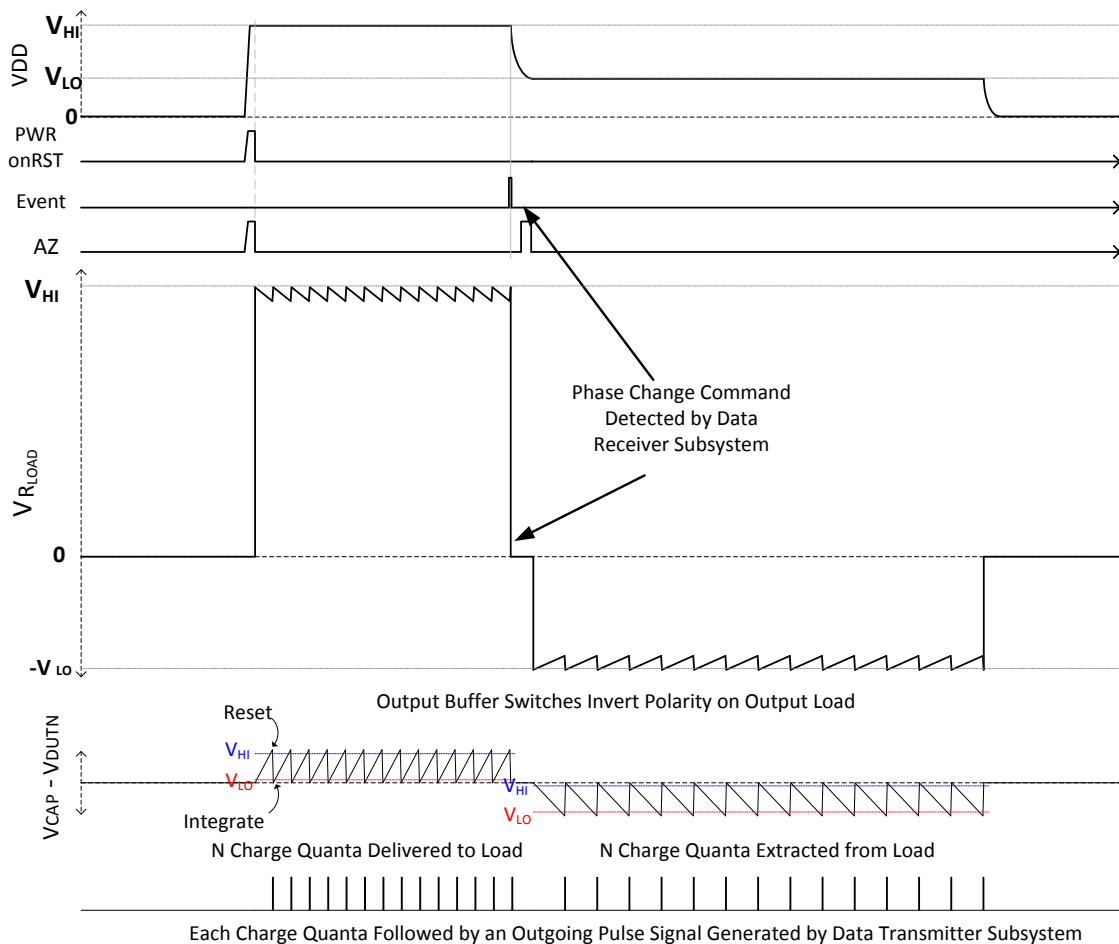
Figure 4.13: Principle of operation with example timing diagram of the adiabatic charge metering stimulator.

4.2.3.5 Comparator

Figures 4.14 and 4.15 show the current reference with supply variation rejection and bias generator circuits for the real time comparator in the stimulator. The comparator itself is a folded cascode amplifier designed with reduced threshold devices in order to operate at very low voltage. The combination of the design choices for the current and bias generators, as well as the amplifier enable the extended operating range which is the goal
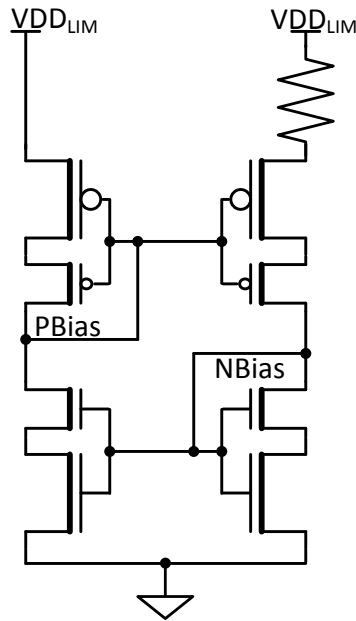
Figure 4.14: Regulated supply voltage invariant current reference.

of this design. The architecture of the folded cascode comparator is shown in Figure 4.16.

4.2.4 Backtelemetry

Finally the backtelemetry subsystem is responsible for transmission of uplink data from the implant to the external transmitter. Whereas downlink data was transmitted through amplitude shift keying (ASK). Uplink data is transmitted through load shift keying (LSK). The external and internal resonators in the system, described in Figure 4.2, are coupled in such a way that changes in the resonance of the implanted resonator (or even an extreme and sustained rise in power consumption) can be observed on the external system
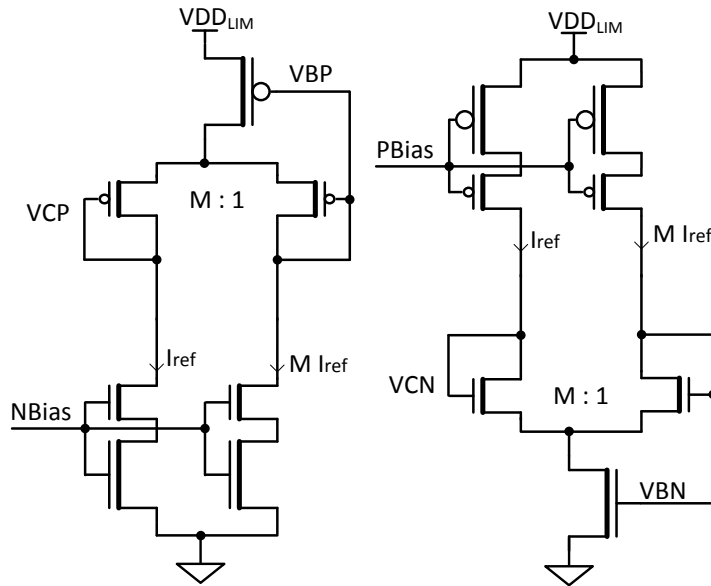
Figure 4.15: Complementary high-output-swing cascode bias generator.
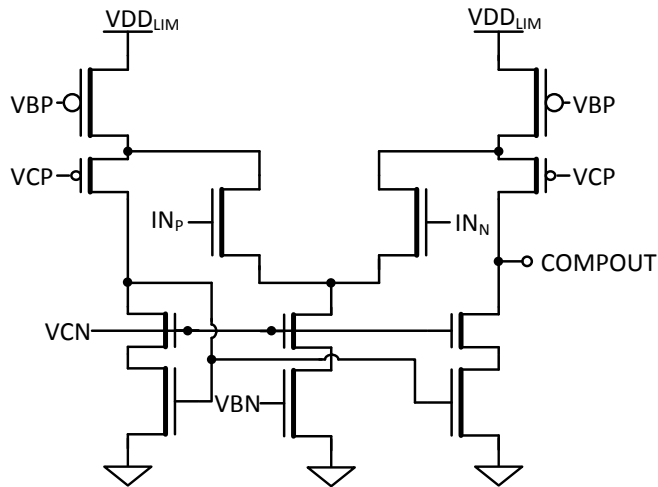
Figure 4.16: Real-time comparator using a folded cascode architecture.
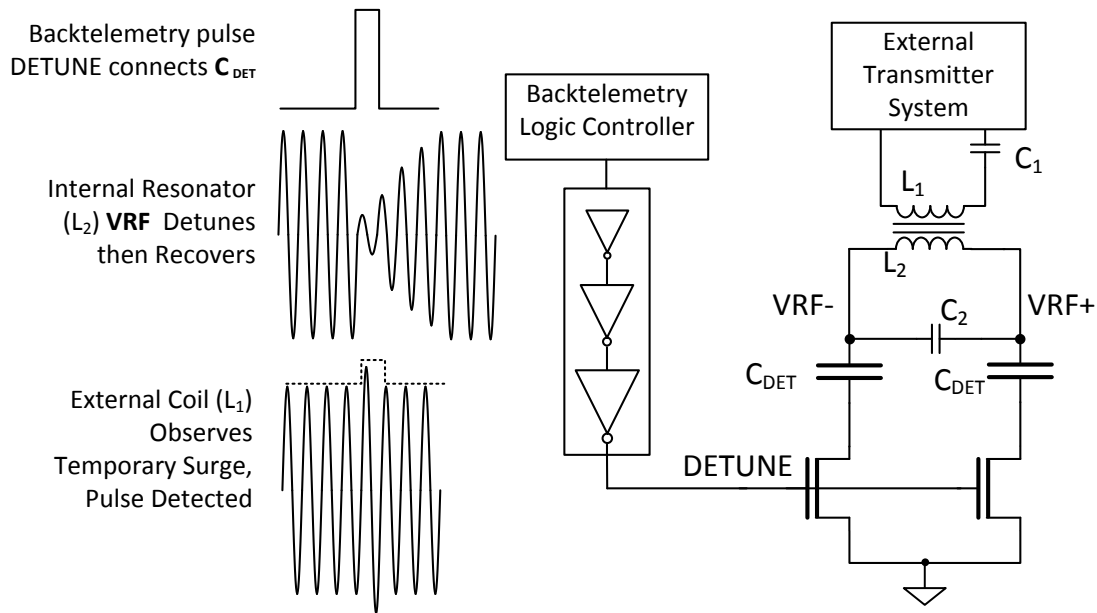
Figure 4.17: Uplink data transmission through load shift keying by parallel detuning of the secondary resonator.

as a reflected impedance.

4.2.4.1 Switch and Driver

When a charge quanta has been delivered to the load, Figure 4.17 shows how a driver and switch system connects additional capacitors to the resonator in order to detune the system and send a backtelemetry pulse signal. Though higher duration backtelemetry pulses and greater magnitude of detuning generate a stronger signal at the external transmitter, they also consume large amounts of power which may inadvertently power down the system.
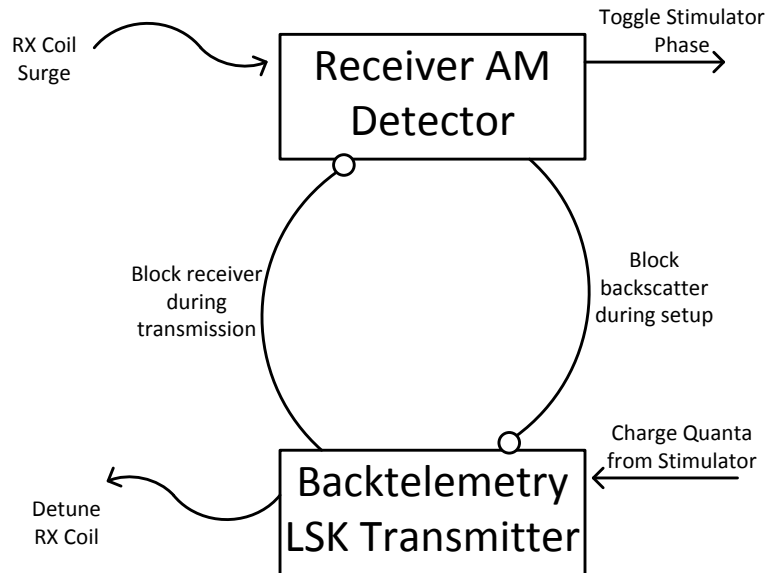
Figure 4.18: The uplink-downlink data telemetry arbitration scheme.

4.2.4.2   Uplink-Downlink Arbitration

In order to prevent incoming and outgoing events from colliding an uplink/downlink arbitration scheme at the implant is proposed and implemented as a timed state machine, shown in Figure 4.18. An additional, but similar system must be included in the external system that ensures data is transmitted faithfully.

4.2.4.3   Closed-Loop Calibration

A remaining detail in the functionality of the system is of critical importance. The external and internal systems are loosely inductively coupled. As this implementation
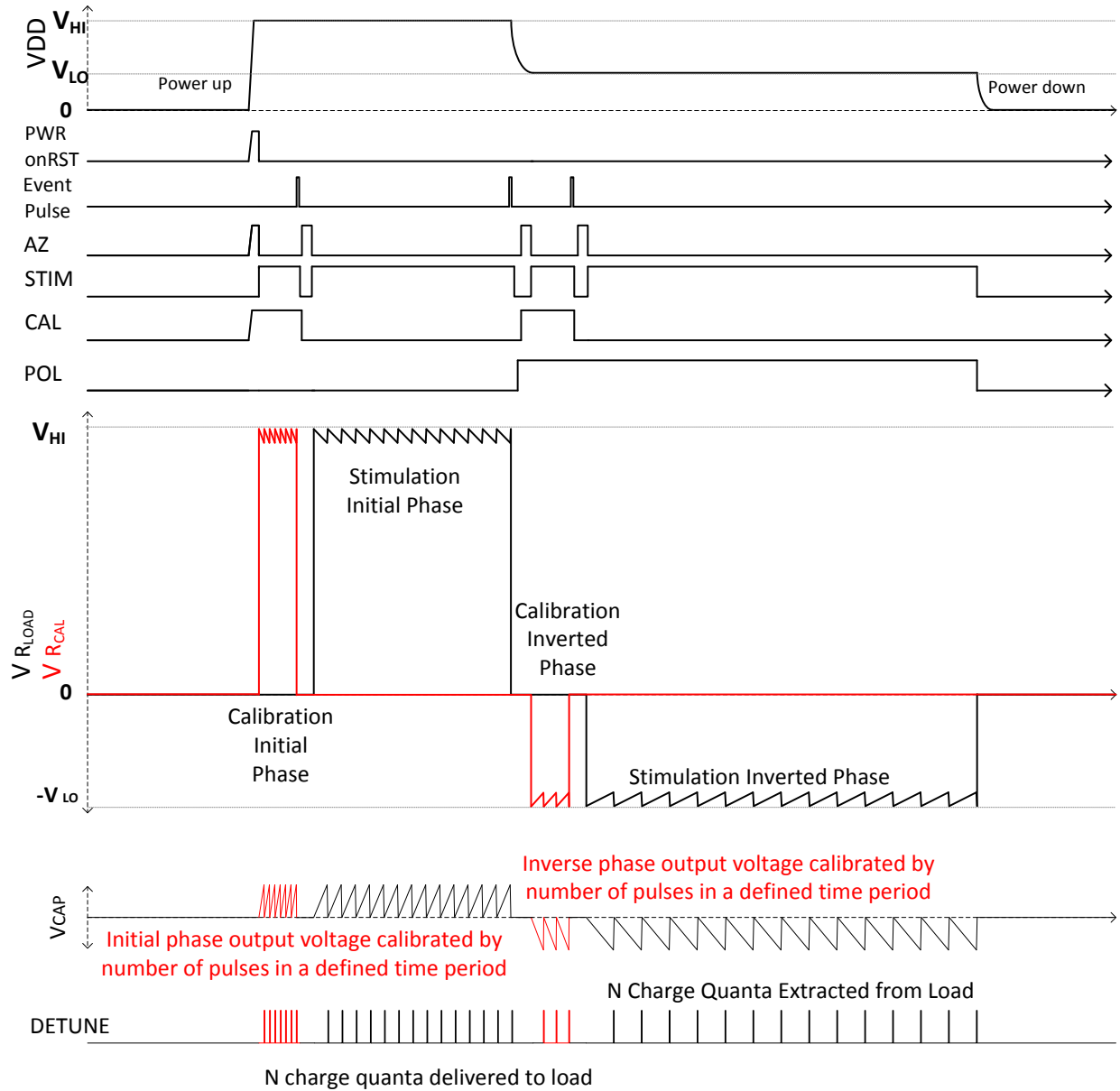
Figure 4.19: The principle of operation with example timing diagram of the adiabatic charge metering stimulator with the addition of voltage calibration phases.

details a retina implant application the coil may be tethered to the eyeball, changing the coupling coefficient whenever eye movements such as saccades and microsaccades occur. In order to ascertain the exact value of the implant's VDD at the time of stimulation, an additional known resistance is provided as a test load. By connecting this resistor to VDD and monitoring the number of charge metering pulses the system transmits to the external system the information required to calculate VDD. Figure 4.19 shows the role of calibration on the system and how charge quanta pulses can be used both to enforce charge balanced stimulation and closed loop voltage control. Having discussed the reasons and implementation of calibration, Figure 4.20 shows the implemented state machine of the system cycling through calibration and stimulation phases as downlink phase changing events are sent from the external system.

4.3   Implementation

4.3.1   Integrated Circuit

The adiabatic RF-powered charge-conserving stimulator was implemented as a custom integrated circuit (IC) fabricated through TSMC in a 180nm CMOS process, spanning a total area of 5 mm^2. Figure 4.21 shows a picture of the IC including main circuit blocks and important I/O pads used in the implant. Notably, the output buffer switch occupies a significantly large area due to the requirement to operate at very low impedance at 0.5 V power supply as well as at 3.3 V. This combination requires a large number thick gate devices to be connected in parallel. RF power and backtelemetry switch inputs are
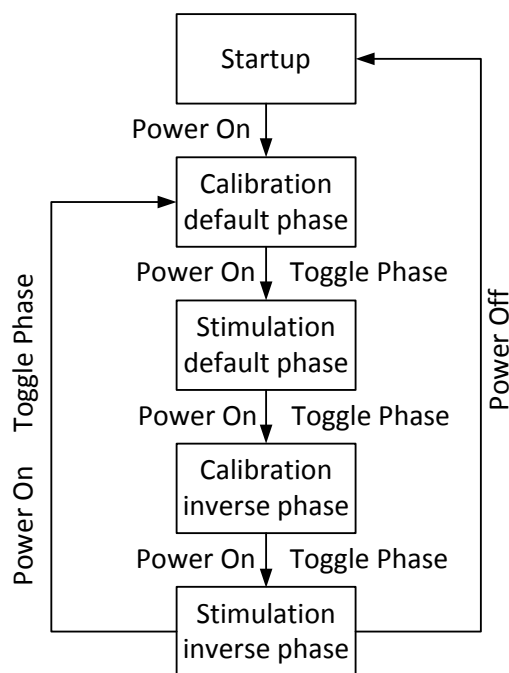
Figure 4.20: Stimulation phase state diagram with transitions toggled by downlink telemetry events.

located in the upper west edge of the chip, while output pins of the stimulator are in the south edge. All remaining space not occupied by primary system components was tiles with on-chip decoupling capacitor cells. Additionally, the north-east corner contains a replica copy of the rectifier circuit in order to do detailed characterization of power efficiency.

4.3.2 Printed Circuit Test Board

A printed circuit board (PCB) was designed and fabricated in order to test all the functions of the chip. As this test board involves inductive wireless coupling, care was taken to avoid unnecessary parasitics. Stray inductances and capacitances in the traces before the chip were minimized by not packaging the chip in a standard package and socket.
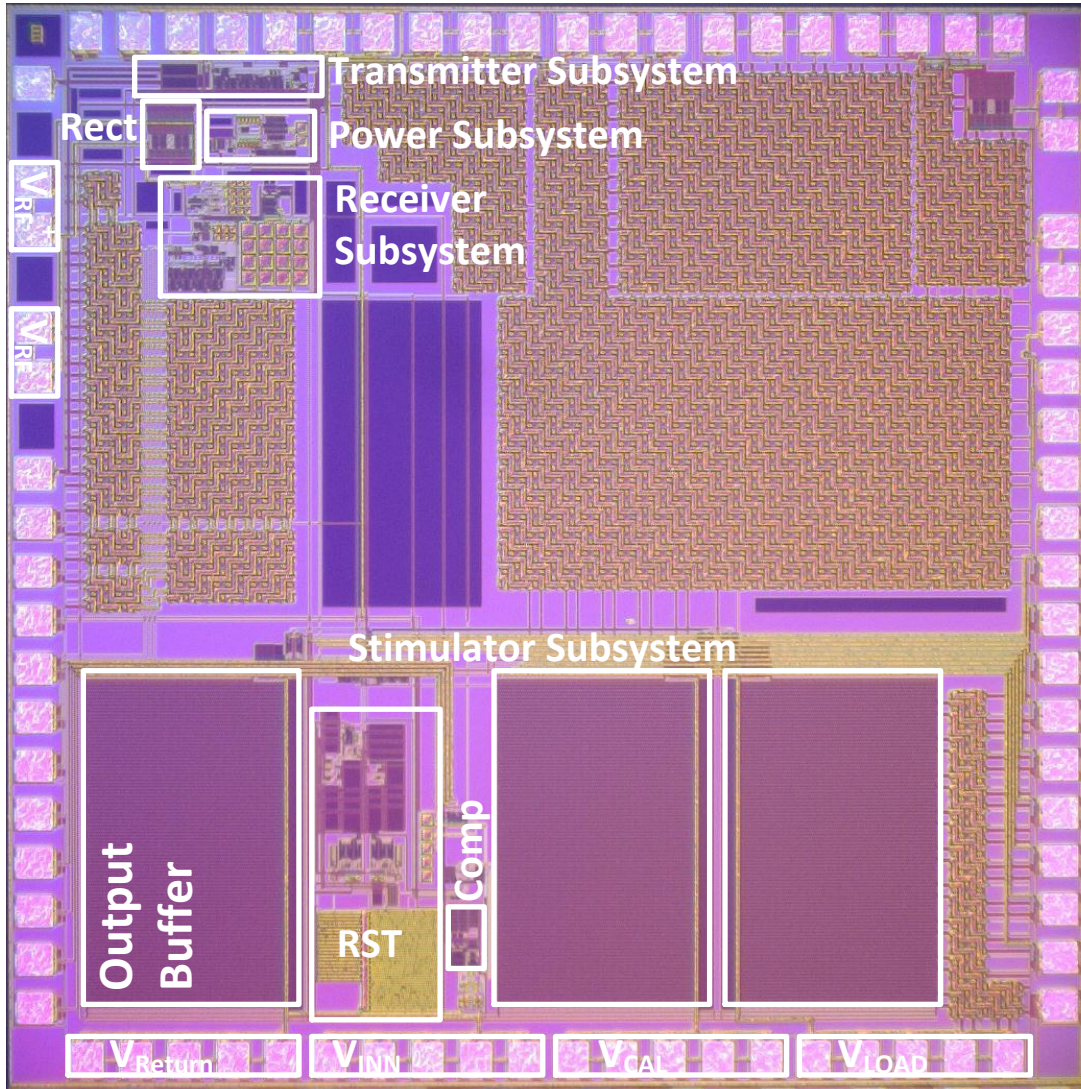
Figure 4.21: Chip micrograph of the retina implant adiabatic wireless power and charge balancing stimulation IC. The location of major system components is overlayed on the die photo.

PCB Cavity Dimensions
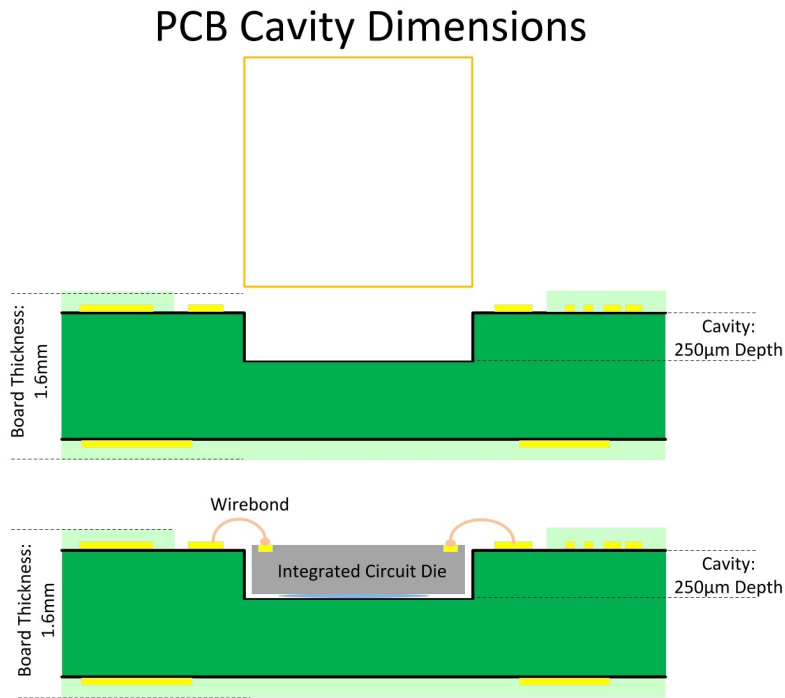
Figure 4.22: Blind cavity for mounting the integrated circuit on the printed circuit board.

Instead the chip was directly wirebonded to the PCB. In order to reduce trace length even further the die was placed in a blind cavity on the board. Figure 4.22 shows the IC cavity. The board is insertable into the 3D wireless test frame described in chapter 3, in order to perform reconfigurable fully wireless tests.

4.4   Measurements and Experimental Characterization

Several tests were conducted on the IC to evaluate the performance of all the subsystems. The board described in section 4.3.2 has separate test circuits for testing each of the subsystems described in Figure 4.3.
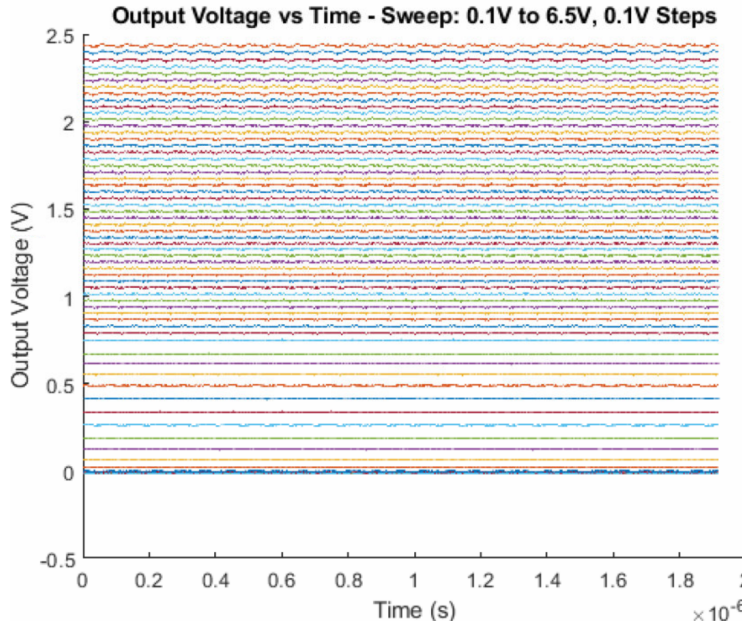
Figure 4.23: Demonstration of wireless AC-to-DC power conversion, showing time traces of DC rectified output for 13.56 MHz AC input of varying peak-to-peak amplitudes transmitted across the wireless link.

4.4.1 Power Subsystem

The power subsystem is responsible for wireless power harvesting and conversion to DC. Additionally, it must generate auxiliary power supplies to power thin gate transistors. As described in section 4.2.1 the system has been designed to provide high efficiency across a wide range of operating voltage. AC-to-DC conversion is demonstrated in Figure 4.23 where a 13.56 MHz sinusoidal voltage wave is transmitted across the wireless link described in chapter 3 and converted to a constant voltage by the rectifier described in Figure 4.7. In this same plot, we can observe the range of the output voltages for various inputs.

In order to compare the performance of this rectifier to recent designs we have characterized two important metrics: Voltage Conversion Ratio (VCR), and Power Conversion Efficiency (PCE). VCR is defined as the ratio of the output DC voltage over input AC

amplitude:

$$\text{VCR} = \frac{V_{DD}}{V_{RF\ amplitude}} \tag{4.1}$$

whereas PCE is the ratio of the output DC power over the average input RF power:

$$\text{PCE} = \frac{P_{OUT}}{P_{IN}}. \tag{4.2}$$

Figure 4.24 shows the voltage conversion measurement for a replica of the rectifier used in the main system with a load of 2 kΩ as a function of output voltage. After the input voltage reaches a sufficient level, corresponding to $0.5V$ output, VCR remains relatively flat around 0.8. The second graph in Figure 4.24 shows high PCE efficiency across the designed output range for the same load condition. These two plots demonstrate the performance of the rectifier is advantageous for the entire range.

The dual complementary regulator described in Figure 4.8 was measured for the same load condition. The results in Figure 4.24 also demonstrate the wide performance of the regulator outputs for VDD_{LIM} and VSS_{LIM}. In addition to VCR and PCE, the ripple output voltage and the startup rise time for the rectified and regulated voltages are also shown. Although ripple and rise time are inversely proportional trade-offs based on the magnitude of the decoupling capacitor, for 5nF both values remain within the requirement for the entire voltage range. Ripple voltages less than 15 mV, and rise times below $20\mu s$ do not negatively affect the functionality of any of the system blocks.
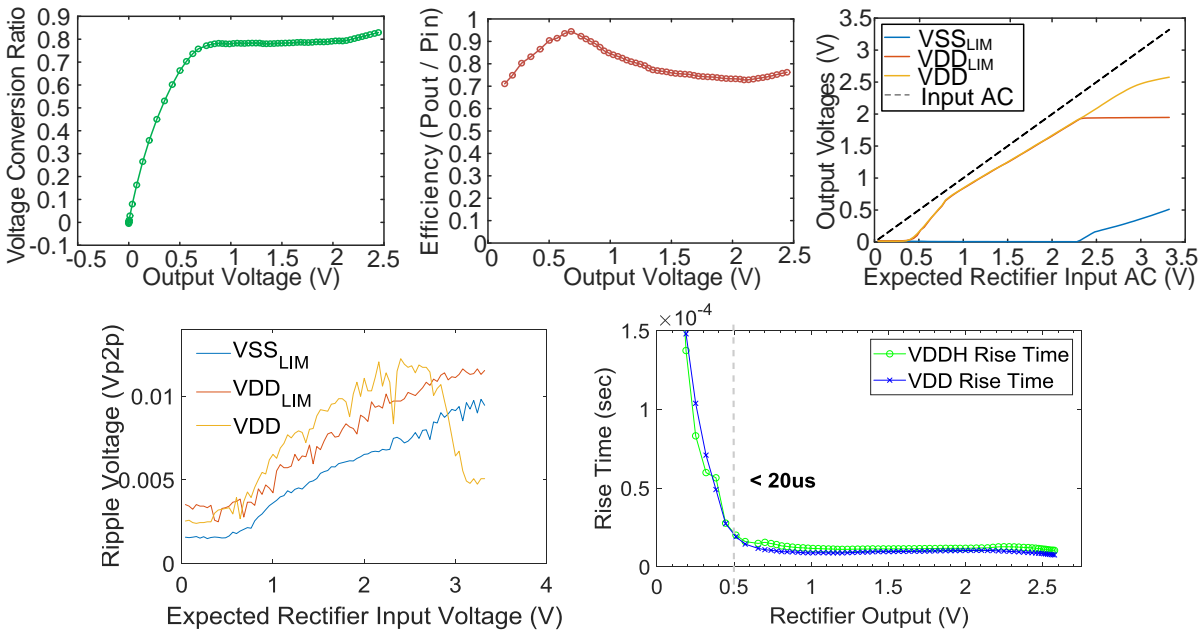
Figure 4.24: Experimental characterization of the power subsystem: voltage conversion ratio, power conversion efficiency, regulator output voltage, output ripple voltage, and power-up rise time.

4.4.2   Data Subsystem

As the subsystem responsible for receiving communications from the external transmitter, the data subsystem described in section 4.2.2 has two main functions that can be quantified: Clock recovery from the externally transmitted signal and AM pulse demodulation. Figure 4.25 shows the recovered 13.56 MHz clock from the RF carrier wave across the entire range of input voltage amplitudes. The under-damped quality of the buffer is an artifact of the digital output driver buffer. The clock is successfully recovered at the appropriate frequency, although phase offset and duty cycle skew increase with lower voltages. The pulse AM demodulation receiver (Fig. 4.10) detects sudden increases
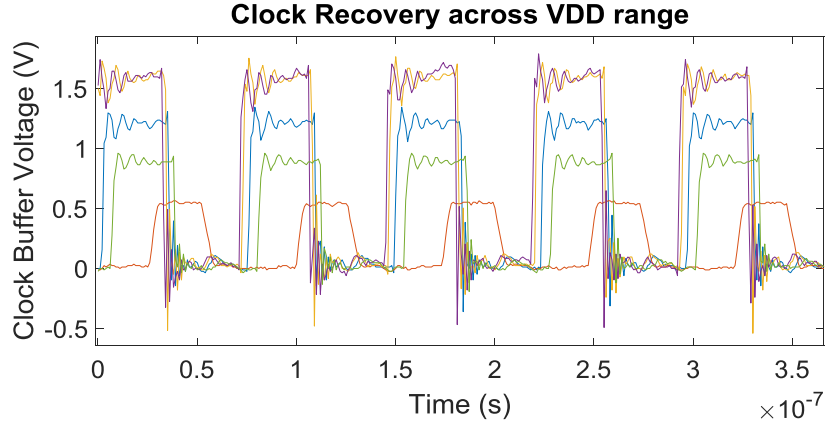
Figure 4.25: Oscilloscope traces of the wireless clock recovery circuit across the operational voltage range. Ringing is due to the measurement probes.

in the input amplitude envelope, but ignores slower changes. In order to quantify the accuracy of event detection we classify 3 different types of errors: missed events, duplicate or multiplied events, and spuriously detected events. Figure 4.26 shows the incidence of the 3 types of errors for two different VDD levels. The left plot, corresponding to 0.6V VDD level, shows a modulation depth threshold of approximately 23% . Past this level, there are no missed events or other detection errors. In contrast, for the 1.4V VDD level, the modulation depth threshold is approximately 5%. Proportionally greater modulation is able to reduce the incidence of missed events to near zero (less than 1 in 1500 according to measurement resolution). Despite the lower threshold, duplicate event incidence prevents the total detection error from completely disappearing even at higher modulation depth.

4.4.3 Stimulator Subsystem

A biphasic voltage pulse must be provided to the MEA to produce light dependent currents at each pixel. The timing of the pulse is configured to optimize neural stimulation.
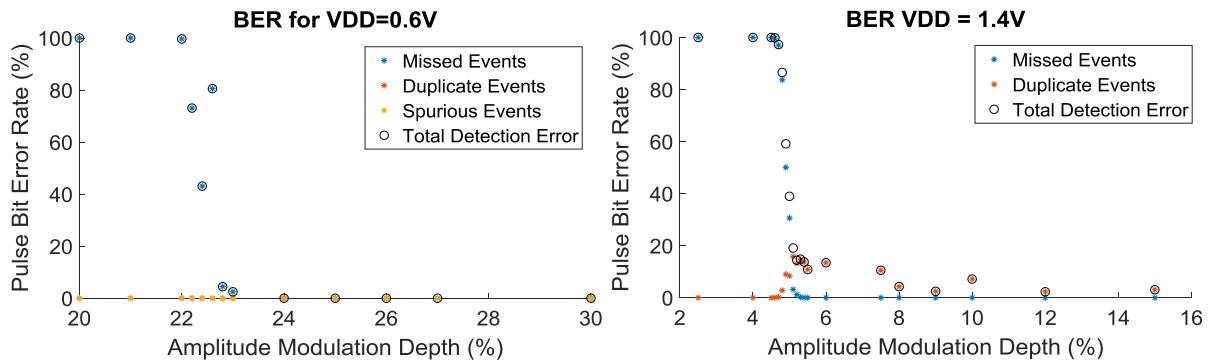
Figure 4.26: Pulse AM receiver bit error rate for two different VDD voltage levels. The sigmoidal shape shows the required modulation threshold for each voltage level.

Enforcing charge balance between cathodic and anodic phase extends electrode life and prevents tissue damage. The proposed stimulator (Fig. 4.11) is shown to correctly produce positive and negative calibration output across R_{CAL}, and stimulation output across R_{LOAD} (Fig. 4.27**a**). In between pulses for each load, the tri-state output buffer switches are set to high impedance (dashed line), permitting the sharing of the metering circuitry. As the voltage is applied to either load (R_{CAL} or R_{LOAD}), charge begins to accumulate on the series metering capacitor C_{MET} until a set threshold is detected by the real-time comparator, the capacitor is discharged by the RST reset switch, and a unit of charge is registered for LSK transmission. Figure 4.27**b** shows the charging of the metering capacitor during application of the stimulation waveform to a resistive load. The 15 charges metered during a time interval can be identically metered during the corresponding inverse polarity phase (4.27**c**) enforcing charge balance. Metering of the charge output through the complex impedance of a wet electrode is demonstrated in Figure 4.27**d**. As the double layer capacitance is part of the load impedance, we can observe a progressive decrease in the (dis)charging period due to the exponentially decaying current. The metering process generates a sawtooth

ripple voltage on the effective electrode bias (Fig. 4.27**a**) with no significant effect on neural stimulation. The discharge rate of C_{MET} is considerably faster than the charging time in both phases, preventing quantization inaccuracy. Moreover, regardless of the test condition the real-time comparator and RST switch driver respond fast enough to contain the charge-discharge voltage within 100 mV.

4.4.4   Backtelemetry

The load shift keying backtelemetry system transmits a pulse for each quantum of charge detected by the stimulator metering system. In Figure 4.27 the charge metering pulses are registered after each charge cycle of C_{MET}. In order to sufficiently detune the input resonator, the impedance of the backtelemetry switch was characterized, measuring the equivalent resistance of the backtelemetry switch at a range of power levels as well as switch activation voltage. Figure 4.28 At the turn-on of the switch, the impedance can range from 34 Ω to 1.04 kΩ. When the backtelemetry switch is not activated ($V_{GS} = 0$) the switch impedance is greater than 10 M$Omega$. Even for a 0 Ω detuning element, the off impedance of the backtelemetry switch is sufficiently high to prevent degradation of the implantable resonator.

The implemented microsystem supports the generation of arbitrary biphasic and triphasic waveforms for pulsed voltage stimulation to drive the electrode array. This stimulator takes advantage of capacitive charge metering as a direct means to enforce charge balance and therefore reduce adverse biological effects and extend electrode lifetime.
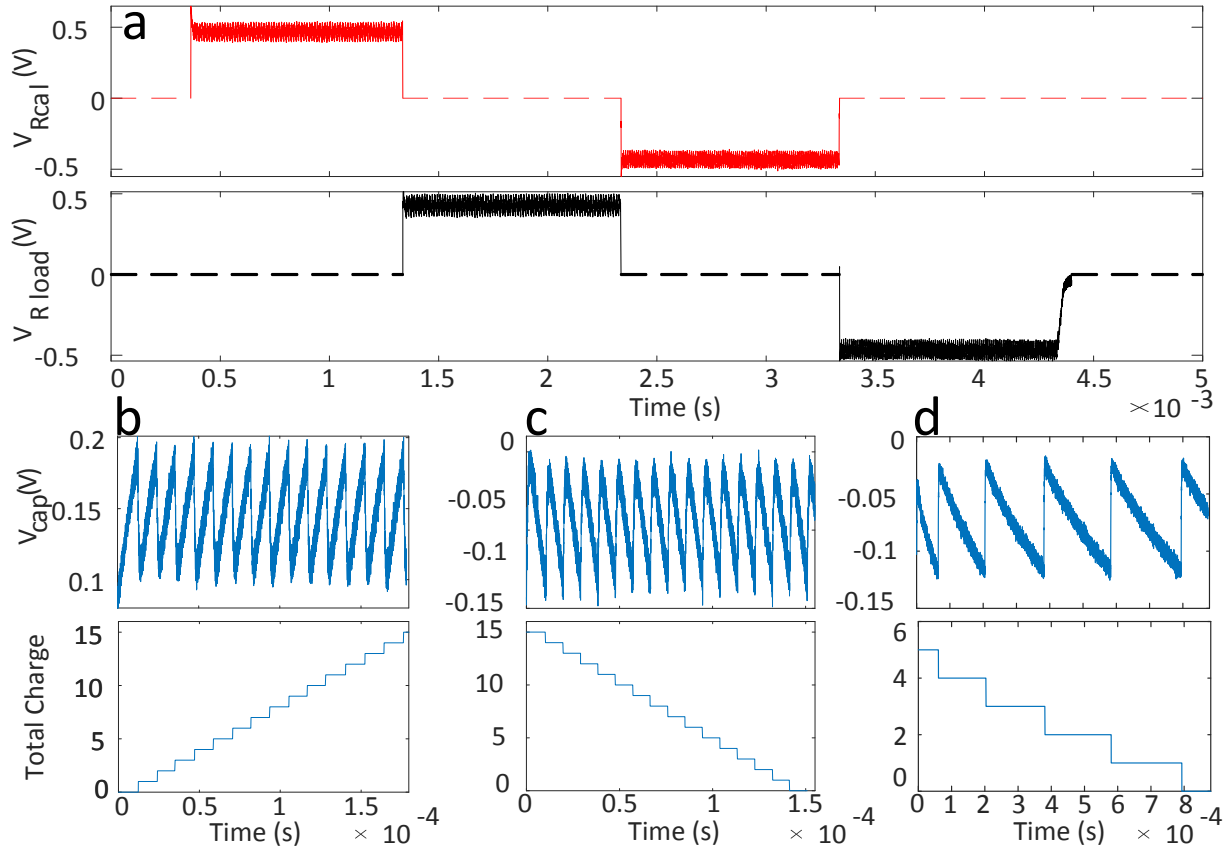
Figure 4.27: Measured results from the charge-balancing stimulator. **a** Output voltage waveforms across the calibration resistor V_{Rcal} (red), and V_{Rload} (black). **b** Voltage across the metering capacitor V_{cap} (top) as 15 charge quanta are counted (bottom) in the positive calibration phase. **c** Same as (b), but during the inverse calibration phase. **d** Same as (b) and (c), but during the stimulation phase for a wet electrode.

4.5 Acknowledgements

Chapter 4 is based on material being prepared for publication by Abraham Akinin, Jeremy Ford, Jiajia Wu, Chul Kim, Hiren Thacker, Patrick Mercier, and Gert Cauwenberghs. The dissertation author is the primary author and investigator of this work.
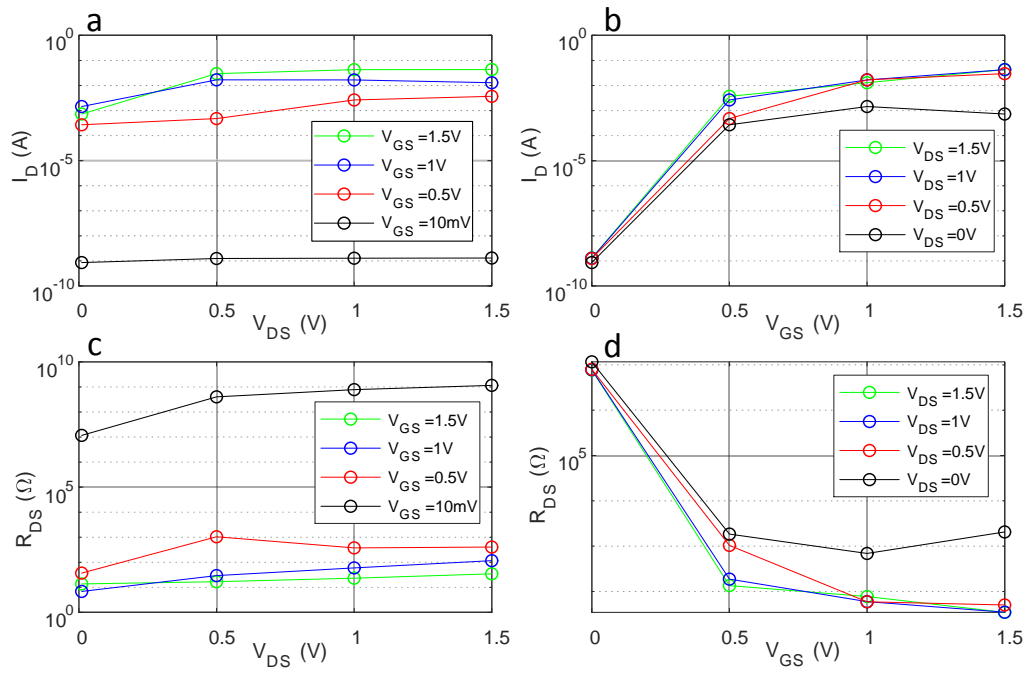
Figure 4.28: Backtelemetry switch current as a function of V_{DS} **(a)**, and V_{GS} **(b)**. Backtelemetry switch impedance as a function of V_{DS} **(c)**, and V_{GS} **(d)**.

Chapter 5

In Vivo Validation of a Silicon Nanoengineered Retinal Prosthesis

For over 20 years, there has been an international, multidisciplinary effort to develop retinal prostheses to restore functional vision to patients blinded by retinal degeneration. In this chapter we describe our work on the development of a novel subretinal prosthesis with 1,512 optically addressed silicon nanowire photodiodes, and demonstrate its functionality in transducing incident light into an electrical stimulation of the remaining retinal circuitry.

5.1 Background

Retinitis pigmentosa and age-related macular degeneration are debilitating causes of blindness resulting from the gradual loss of photoreceptors in the outer retina. It is estimated that over one million people worldwide are blinded by retinitis pigmentosa [46] and it is

projected that there will be 196 million people with age-related macular degeneration by 2020 [105]. Available treatments slow the progress of the degeneration, but do not reverse vision loss. In these diseases, only the photoreceptor layer degenerates leaving the remainder of the retina intact [97], albeit with some remodeling [53]. Retinal prosthetics function by electrically stimulating spared retina, bypassing the missing photosensory neurons. This approach makes use of the remaining visual pathway to elicit phosphenes in a retinotopic manner to restore some useful vision to the patient. There are three retinal prostheses that are available to patients in the European Economic Area having been granted the CE mark for commercial use: Retina Implant Alpha AMS subretinal implant with 1,600 electrodes at 70 μm pitch (Retina Implant AG, Reutlingen, Germany) [27, 33], IRIS® II epiretinal implant with 150 electrodes (Pixium Vision, Paris, France) [88], and Argus® II epiretinal implant (Second Sight Medical Products Inc, Sylmar, CA) [24]. Of those, only the Argus II device is also approved by the US FDA and available to patients in the US market, but its 60 electrodes at 525 μm electrode pitch results in stimulation being spread over a large field of view, precluding high resolution vision. Recently, Retina Implant AG and Pixium Vision have commenced clinical trials in the United States for their latest devices, Alpha AMS [20] and PRIMA [19] (378 photovoltaic electrodes, 70 μm pitch) [7, 34, 65, 68, 71, 83]. A major goal of retinal prosthetic development is to decrease pixel spacing and increase pixel number, to improve high acuity vision over a larger area of the visual field. We have developed a retinal prosthesis with a high-resolution subretinal neurostimulator consisting of 1,512 optically addressed silicon nanowire photodiodes [42]. Each nanowire photodiode converts incident light into electric current to stimulate nearby inner retinal neurons, which

allows for a compact, optically addressable stimulating array, and obviates the need for individually wired electrodes. There are several key advantages to implanting the device in the subretinal space. Specifically, it avoids direct activation of retinal ganglion cell axons in the retinal fiber layer, which can cause streaked phosphenes [37]. It also makes use of remaining inner retinal circuitry allowing for more natural image processing. In vivo electrophysiology studies are essential to demonstrate that an implant effectively stimulates the retina to generate neural signals that are transmitted to the visual cortex as in natural vision. Recording visual evoked potentials (VEPs) from the occipital cortex in response to repeated visual stimuli is a common clinical measure of visual pathway integrity [80]. This technique can be extended to record electrically evoked potentials (EEPs) to demonstrate the effectiveness of prosthetics to electrically stimulate the retina and cause a cortical response in the visual cortex. [16, 64, 66, 70, 76–78, 89, 93, 103, 108, 109]. In vivo studies also allow for optimization of surgical technique and biocompatibility evaluation of the retinal prosthetic device in an animal model. Here, we use an in vivo rabbit model to demonstrate the effectiveness of subretinal stimulation with a nanowire prosthesis and compare the visible light induced VEP response with the EEP response to prosthetic stimulation.

5.2   Methods

5.2.1   Photovoltaic Implants

The silicon nanowire photovoltaic devices were fabricated using the procedures as previously described [42], The subretinal implants consisted of 6 silicon tiles mounted onto
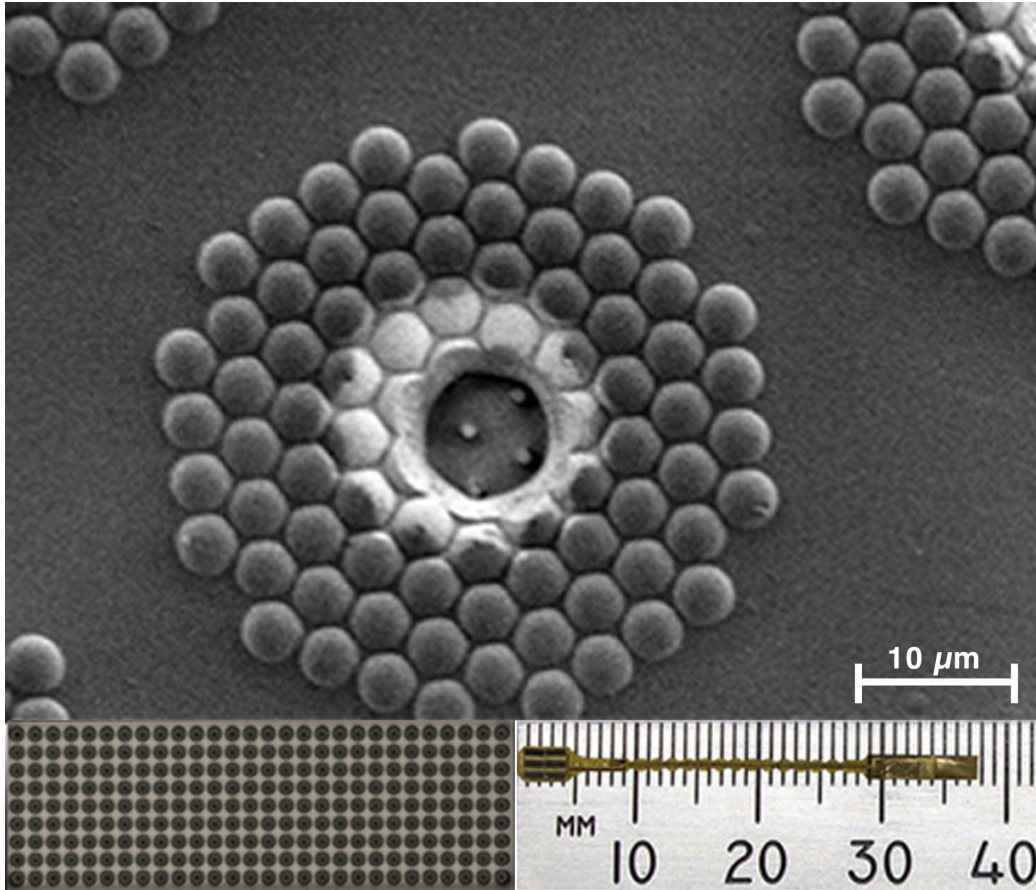
Figure 5.1: The retinal prosthesis consists of 6 tiles on a polyimide substrate (bottom right). Each tile has 252 electrodes (bottom left). Each of the electrodes has 85 silicon nanowires capped with iridium oxide (top).

a flexible polyimide substrate (Figure 5.1, bottom right), covering an area of 3 x 4 mm, or about 17 degrees of visual field. Each tile measured 1.4 x 0.5 mm and contained an array of 252 sputtered iridium oxide film (SIROF) electrodes with a diameter of 12 μm and spaced with a pitch of 50 μm (Figure 5.1, bottom left) for a total of 1,512 stimulating electrodes. Each electrode consisted of a group of 85 vertically aligned silicon p-n junction nanowires (Figure 5.1, top), bundled together under a transparent indium tin oxide electrode. Through the photovoltaic effect, the nanowires convert the energy of the incident light into

114

an electron-hole electrical charge pair, as a typical photodiode [23, 94, 100]. Each nanowire electrode pixel is coated with parylene and capped with a SIROF electrode located in the center of the pixel, which delivers the charge to the retina. The stimulating electrodes shared a common return electrode located 6 mm away from the stimulating electrodes. In this study, the devices were unbiased and powered only with high intensity infrared light described in section 2.4. Each implant was sterilized in a steam autoclave (Tuttnauer, Hauppauge, NY) for 7 minutes at 31 PSI and 134 °C.

5.2.2 Device Implantation Surgery

New Zealand pigmented rabbits (N=12, average age 4.9 months, 4.1 kg) were implanted with a subretinal prosthesis in this study. All experimental methods and animal care procedures adhered to the ARVO Statement for the Use of Animals in Ophthalmic and Vision Research and were approved by the UCSD Institutional Animal Care and Use Committee. Anesthesia was induced by a cocktail of ketamine hydrochloride (35 mg/kg) and xylazine (5 mg/kg) administered by subcutaneous injection, and maintained with alternating half-doses of ketamine only or ketamine and xylazine every 30-40 minutes. The pupils were dilated with 1% atropine, 0.5% tropicamide, and 2.5% phenylephrine. Implantation of the device was performed using a trans-scleral (i.e. ab externo) approach unilaterally in the right eye. Two polyimide glides were used to support the device on both sides as it was inserted into the subretinal space. The head of the device containing the stimulating electrode array was placed near the visual streak. The tail of the implant was anchored at the scleral incision by a 7-0 nylon suture. After insertion, a 25 gauge three-port
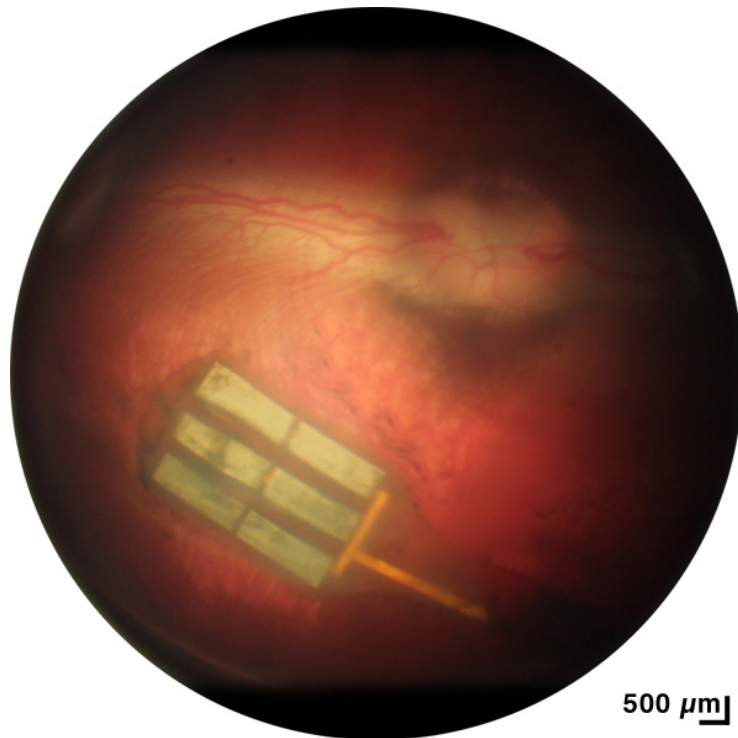
Figure 5.2: Fundus photo showing retina covering the 6-tiled nanowire implant following surgical placement into the subretinal space.

trans pars plana vitrectomy was performed before air-fluid exchange and final tamponade with silicon oil (ADATO SIL-ol 5000, Bausch & Lomb, Rochester, NY). The vitrectomy was performed using a Landers wide field vitrectomy lens under a surgical microscope (Zeiss, Oberkochen, Germany). Fundus photos (Figure 5.2) and optical coherence tomography (OCT, Figure 5.3) were taken the following day to verify implant position.

5.2.3 Cortical Electrode Implantation Surgery

The day following implantation surgery the rabbit was implanted with cortical recording electrodes as previously described. [56, 89] The rabbit was anesthetized as described above and the skin over the posterior skull was prepared by shaving the scalp
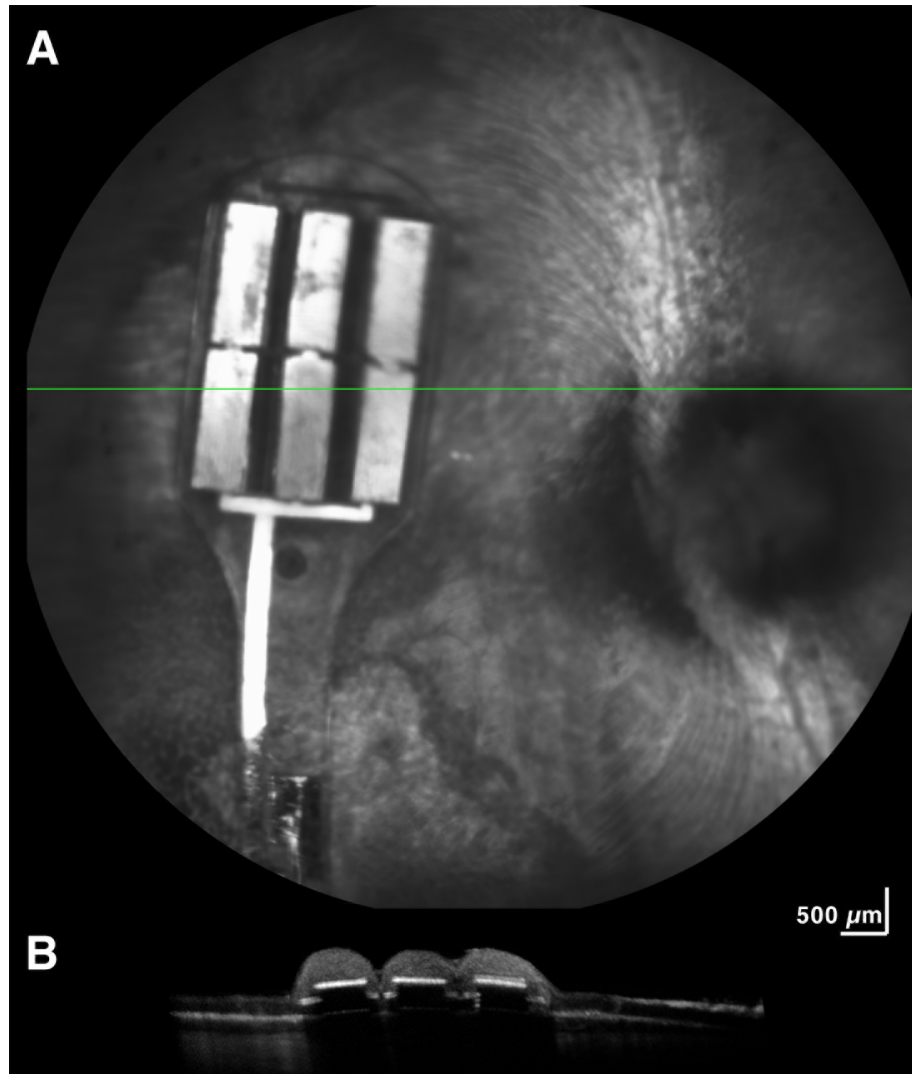
Figure 5.3: Optical Coherence Tomography (OCT) imaging 24 hours after implantation shows that retina overlaying the device is in close contact with the retinal prosthesis tiles. The horizontal line across the prosthesis (A) corresponds to the cross section of retina over the tiles shown below (B).

with electric clippers. The skin was incised, periosteum opened, and the skull exposed. Two

skull burr holes were made with a 1.5 mm surgical drill 5 mm away from the sagittal suture

on each side overlying the visual cortex and 6 mm anterior to lambda. A third burr hole

was made for the reference electrode 3 mm right of the sagittal suture and 5 mm anterior

to bregma (Figure 5.4). A grounding electrode was placed on the ear. Subsequently, 4.75
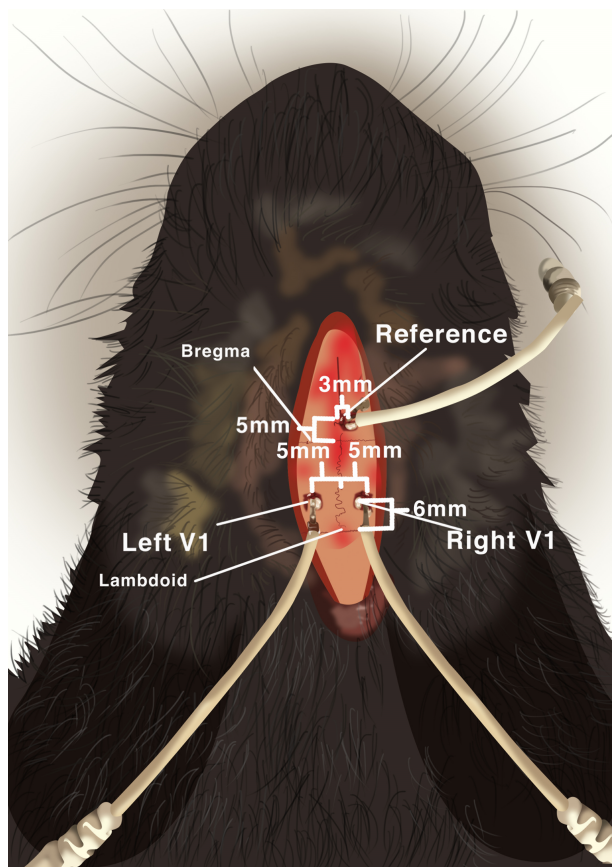
Figure 5.4: Cortical screw electrode placement diagram demonstrating electrode locations with respect to skull suture landmarks in the rabbit.

mm cranial screw electrodes were inserted until achieving contact with the dura. Dental cement was then applied and cured to hold the electrodes securely in place and the incision was closed by suturing.

5.2.4 Light Stimulation Delivery

A Large Spot slit-lamp adapter (Iridex Corp, Mountain View, CA) was used to project a 3 mm diameter laser through a slit-lamp (Haag-Streit, Mason, OH) into the eye. Two laser diodes (DJ532-40 and L852P150, Thorlabs, Newton, NJ) were used to emit 10

ms pulses every 500 ms of either 532 nm 100 μW/mm^2 green light or 852 nm 3.4 mW/mm^2 infrared light. Green 532 nm light was used as a positive control to verify natural VEPs were elicited from retina over the implant. Although the device is sensitive to both visible and IR light, we used 852 nm IR light to activate the device to avoid natural stimulation of the rabbit photoreceptors. The laser diodes were mounted in a temperature controlled mount (TCLDM9, Thorlabs) and driven by a Benchtop Laser Controller (ITC4020, Thorlabs). In patients, a glasses-mounted camera will capture the visual scene and project patterns of IR light into the implanted eye via a DLP pico display (Texas Instruments, Dallas, TX) while still permitting visible light to pass through allowing for residual natural vision.

5.2.5 Electrophysiology Recording

Electrophysiology measurements were recorded using an animal physiology UBA-4204 Universal Biomedical Amplifier (LKC Technologies, Gaithersburg, MD) at 2 kHz sampling rate. A low-cut filter at 1 Hz, high-cut filter at 100 Hz, and notch filter at 60 Hz were applied to reduce ambient electrical noise. Unrelated cortical activity and noise were further minimized by averaging trial repeats (50-200) for each experimental condition. A HK Loop ERG electrode (Unimed Electrode Supplies, Farnham, United Kingdom) was placed on the cornea to monitor the device electrical activation and a reference electrode was placed on the nose. Data was recorded for 256 ms every 500 ms. Following electrophysiology recordings, anesthetized animals were euthanized by an intracardiac injection of 120 mg sodium pentobarbital per kg body weight. After euthanasia, the eyes were enucleated and processed for histological analysis by light microscopy.

5.2.6   Data Analysis

Data was imported into MATLAB (The Mathworks, Inc., Natick, MA) for visualization and analysis. The baseline, measured at the first point, was subtracted from each trace such that all recordings began at 0 V. The amplitude of the N1 was measured at the lowest local minimum between time 20-60 ms after the start of the laser pulse. The start of the N1 time window was set at 20 ms to exclude the stimulation artifact. We used 60 ms as the end of the N1 time window based on the existing literature and preliminary data. P2 was measured at the highest local maximum between 60 ms and the end of the recording. Local extrema were determined with the findpeaks MATLAB function. The VEP and EEP amplitudes were calculated from N1 trough to P2 peak. Latency of N1 and P2 was calculated from the start of the onset of the laser pulse. A total of 229 cortical recordings were made from 7 rabbits (14 eyes); 108 recordings (from 7 eyes) of IR laser on the device inducing EEPs, 45 recordings (from 7 eyes) of focal green laser inducing VEPs in the implanted eye, 54 (from 7 eyes) recordings of baseline cortical activity without stimulation, and 22 (from 4 eyes) recordings of IR laser stimulation in the non-implanted eye. Corneal potentials were recorded from 6 rabbits. For the statistical analysis, a mixed model regression was performed using the VEP and EEP amplitudes as the dependent variable and recording conditions (4 groups) as the independent variable while assigning the animal ID as a random effect to account for the repeated measurements. After identification of a significant association between amplitude and recording conditions, further comparisons of the least square means of amplitude among the 4 recording conditions were performed

using the student's t-test while limiting Type I errors to a rate of 0.05. The statistical analysis was performed using JMP SAS software version 13 (JMP, Cary, NC).

5.3 Results

5.3.1 Electrically Evoked Potentials
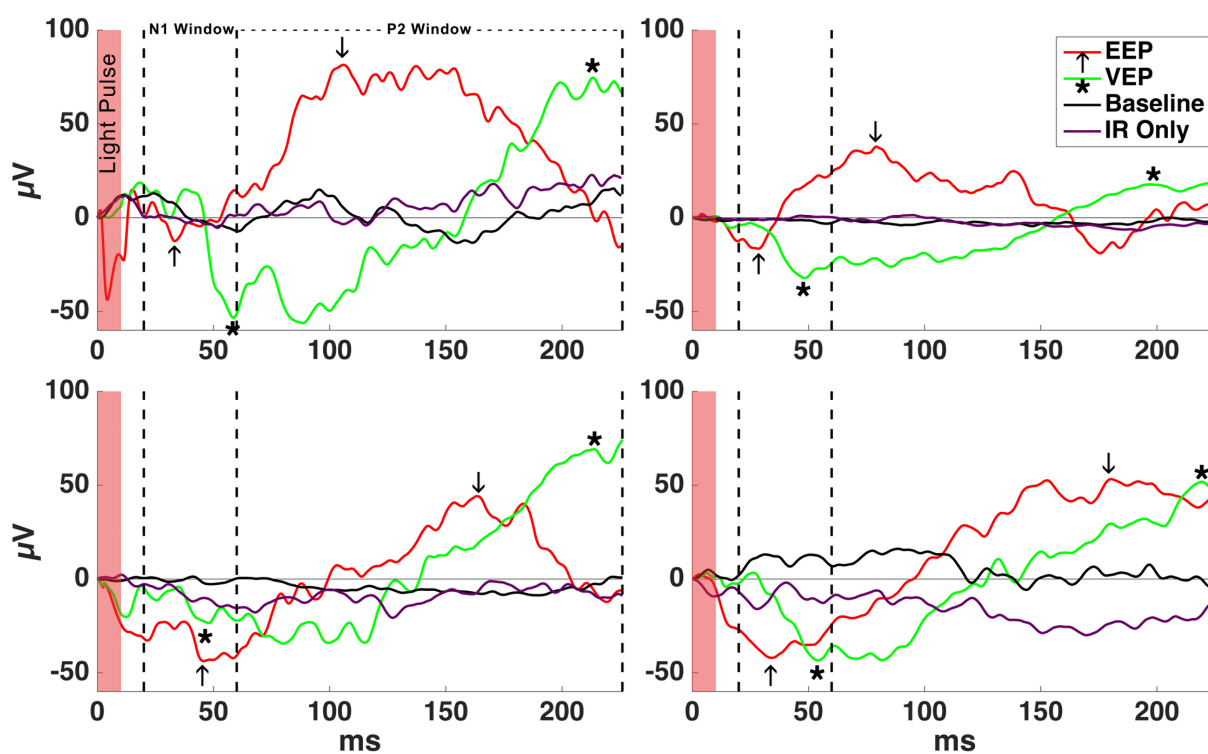
Figure 5.5: Example EEPs from 4 rabbits in response to electrical stimulation of the retina as the subretinal implant was activated with a 10 ms pulse of IR light over 50 repeats averaged. EEP N1 and P2 are marked with arrows (↓/↑). Example VEPs in response to focal green stimulation are shown for comparison. VEP N1 and P2 are marked with asterisks (*). No VEPs were detected in response to 10 ms pulsed IR light in the non-implanted eye, which resulted in a signal similar to baseline cortical activity without stimulation.

To examine how stimulation of the prosthetic device activates retina, electrically
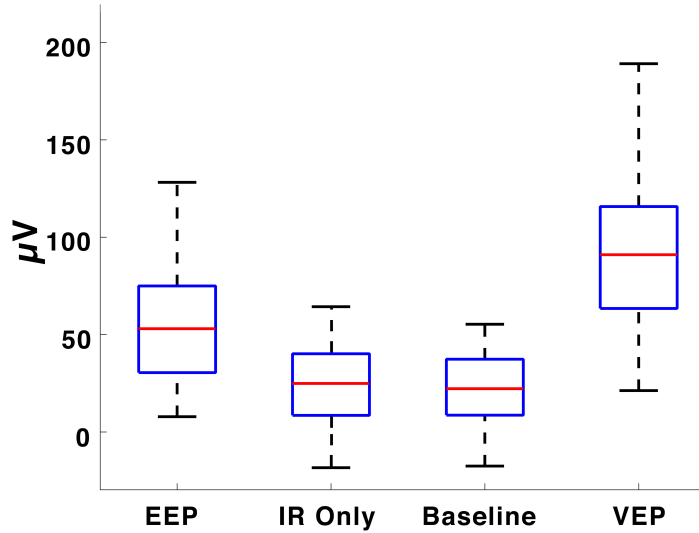
Figure 5.6: The average focal VEP amplitude (94.88 ± 43.3 μV) was significantly higher than EEP (54.17 ± 33.4 μV), IR Only (24.07 ± 22.1 μV), and baseline cortical activity (23.22 ± 17.2 μV) amplitudes. Average EEP amplitude differed significantly from IR stimulation of the non-implanted eye and baseline. Cortical potentials measured when stimulating the non-implanted eye with IR light did not generated amplitudes significantly different from baseline cortical activity. Boxes indicate 25th/75th percentiles and dotted lines are the ranges of amplitude values.

evoked potentials (EEPs) were recorded by activating the subretinal prosthesis with a 10 ms pulse 3 mm diameter spot size 852 nm infrared laser with an intensity of 3.4 mW/mm^2, resulting in a charge injection of 0.32 nC per electrode. 852 nm light activates the prosthesis with high efficiency, but does not activate mammalian photoreceptors. [81] IR stimulation of the device resulted in a voltage waveform on the contralateral electrode with a negative peak (N1) after stimulation followed by a positive peak (P2), consistent with activation of the visual cortex (Figure 5.5). The average EEP amplitude from 108 recordings was 54.17 μV (SD = 33.4) and average N1 latency was 36.55 ms (SD = 11.6) (See Table 5.1 and Figure 5.6). To determine if high intensity IR light could directly activate photoreceptors and

cause a VEP without prosthetic stimulation, we pulsed 852 nm light in the non-implanted eye at the same intensity and duration. The non-implanted eye was used instead of focusing the laser spot on retina away from the device to eliminate the possibility of activating the device with scattered light from the high-powered laser. No VEP waveform was observed from IR stimulation in non-implanted eyes and the average trough-to-peak amplitude of cortical activity in response to pulsed IR light stimulation was not significantly different from baseline cortical activity recordings in the absence of any stimulation (Figure 5.6).

5.3.2   Focal VEPs Elicited from Retina Over the Device

To examine how implantation of the prosthetic device may influence normal responses of the retina, we stimulated the implanted eye with a visual stimulus using a 3 mm diameter spot of 532 nm laser pulsed for 10 ms at 2 Hz. From a total of 45 recordings, the average focal VEP amplitude was 94.88 ± 43.3 μV and average N1 latency was 48.04 ± 12.3 ms. Implanted eyes remained sensitive to visible light after implantation, exhibiting normal VEP waveform kinetics. The VEP amplitudes were greater than EEP amplitudes ($p < 0.0001$) and EEP N1 latencies were significantly faster than VEP N1 latencies by an average of 11.5 ms ($p < 0.0001$).

5.3.3   Performance Monitoring from Corneal Potentials

The HK Loop ERG electrode placed on the cornea was used to record the voltage change as the device was activated with varying light intensities. These measurements were recorded in 3 rabbits pre-euthanasia and 3 rabbits immediately post-euthanasia,

Table 5.1: The average VEP elicited by focal green stimulation was significantly higher than all other conditions (column 1). The average EEP elicited by device activation was significantly higher than both baseline activity and IR in the non-implanted eye (column 2). IR stimulation of the non-implanted eye did not result in cortical activity any greater than baseline cortical activity (column 3).

	Focal Green VEP	Device Elicited EEP	Non-Implanted Eye	Baseline Activity
	n=45	n=108	n=22	n=54
	avg=94μV	avg=54.17μV	avg=24.07μV	avg=23.22μV
	sd=43.3	sd=33.4	sd=22.1	sd=17.2
Baseline Activity	p<0.0001	p<0.0001	p=0.8827	
Non-Implanted Eye	p<0.0001	p<0.0001		
Device Elicited EEP	p<0.0001			

no systematic difference was observed between pre and post-euthanasia experiments. A typical device activation signal is shown in the top graph of Figure 5.7 as IR light was pulsed for 10 ms while varying the IR power from 0 to 3.4 mW/mm^2. The trough-to-peak corneal potential amplitudes resulting from device activation increases logarithmically with increased IR laser power, as shown in the bottom six graphs of Figure 5.7. Although the corneal potential amplitude varied greatly between recordings, the shape of the relationship between corneal potential and irradiance remained consistent.

5.4 Discussion

The purpose of this study was to determine the feasibility of a photovoltaic nanowire based subretinal prosthesis to drive visual responses in a rabbit model. We demonstrate
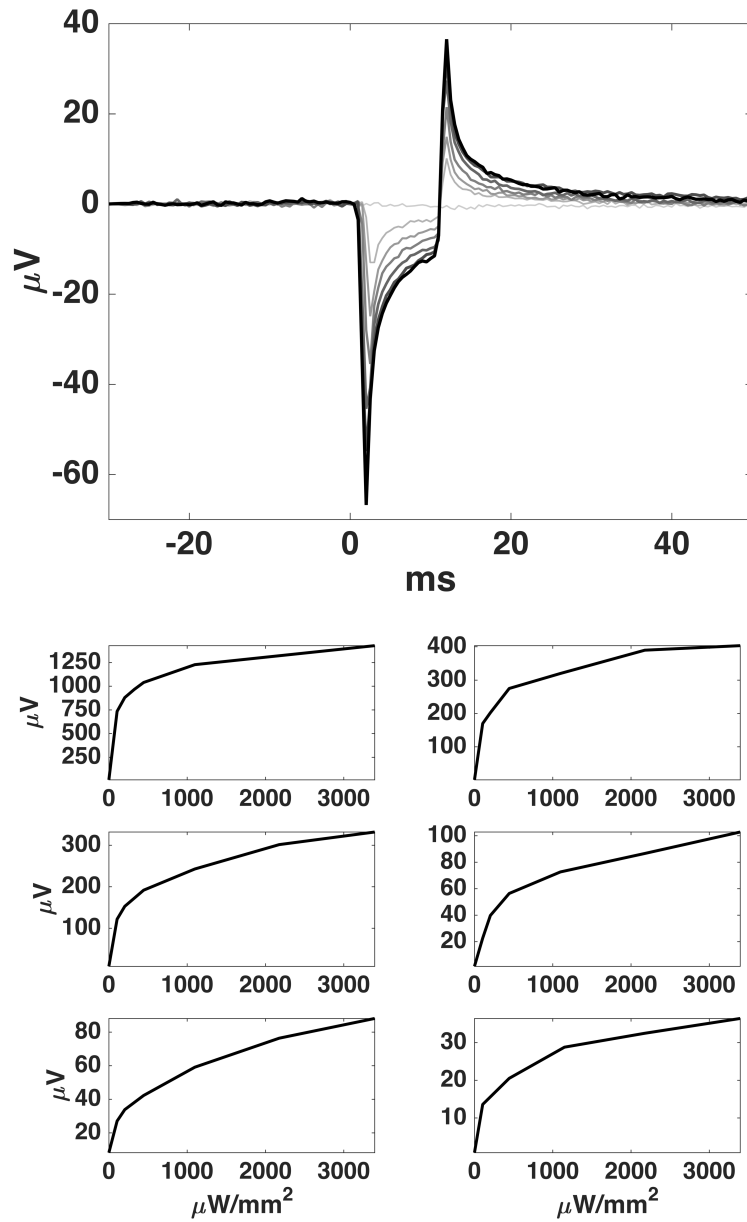
Figure 5.7: The device activation signal recorded from an electrode on the cornea increased in amplitude as the IR light power activating the device was increased. The top graph shows a typical device activation signal waveform. The bottom six graphs show the relationship between device activation corneal potentials and IR power in 3 live (left) and 3 euthanized (right) rabbits. Note that the absolute voltage amplitude varied due to variations in electrode placement and tissue impedances.

that the subretinal nanowire prosthesis can generate visual cortical signals powered only with infrared light by recording electrically evoked potentials (EEPs) in anesthetized rabbit visual cortex. Furthermore, as a negative control, we showed that IR light of the same intensity does not cause any stimulation of photoreceptors in intact retina of the non-implanted eye, indicating that visual cortical signals are the result of electrical stimulation of the retina by the prosthetic. Initially the negative control recordings were taken by focusing the IR laser on retina further away from the device in the implanted eye, however we detected some device activation from the corneal electrode recording, likely due to scattering light from the high intensity laser. Therefore, the non-implanted eye was used to prevent scattered light from confounding the experiment. In addition, we demonstrate that subretinal implantation of the prosthetic device can be successfully performed while preserving the function of the overlying retina by recording focal visually evoked potentials (VEPs) in response to visible light, and we show how corneal potential recordings can be used to validate device activation. Together these results provide evidence for the viability of a subretinal nanowire prosthetic approach to vision restoration.

Measuring VEPs and EEPs in an in vivo animal model is a standard pre-clinical practice for most retinal prosthesis research groups, however there is considerable variability in how results are presented due to a lack of standardized methods. Even so, there are still specific response hallmarks that are common between groups. For example, although some groups present a fast positive peak followed by a long negative trough [76, 77, 89] whereas other groups present a fast negative trough followed by a long positive peak [16, 64, 66, 70, 93, 108, 109], there is still a typical waveform pattern of a short latency voltage

deflection (either negative or positive) followed by a rapid reversal in voltage that slowly decays back to baseline. This typical waveform pattern is qualitatively similar to a classical VEP waveform with one major difference being that EEP latencies are generally shorter than VEP latencies [70, 89]. It is theorized that the shorter latencies of electrical retinal stimulation are a result of bypassing the relatively slow phototransduction cascade of the photoreceptors by directly stimulating inner retinal neurons. Our results are consistent with other groups, showing a shorter N1 EEP latency than VEP N1 and a characteristic waveform that fits the overall interpretation of electrically evoked potentials.

Vertical silicon nanowires are highly efficient at utilizing the photovoltaic effect to convert light into electrical stimulation. The p-n junction within the silicon photodiode is responsible for the photovoltaic conversion of light to current; no other material used in the fabrication of the device can contribute to the photocurrent given the band gap energies of each material [9, 23, 94, 100]. In this study, we used 3.4 mW/mm^2 IR light to activate the silicon nanowires operating in photovoltaic mode. This level of irradiance is 20 times lower than thermal safety limits for 10 ms pulses of 852 nm light [67]. Past work from our group has shown that applying bias to the nanowire devices greatly increases the gain, which can be exploited to further decrease the irradiance required to reach stimulation threshold [42]. Regardless, these experiments serve as an important proof of principle in the design of subretinal nanowire prosthetics. Future experiments will explore the relationship between light intensity, charge injection, stimulation frequency, and the stimulation threshold to elicit EEPs.

The corneal potential recorded from the ERG electrode served as a control to confirm

127

device activation. Corneal potential increased logarithmically as the IR laser power was increased, consistent with a logarithmic increase in charge output. This is congruent with similar work from Lorach et al. that reported increased corneal potential amplitude with increased illumination area [64] As expected, the absolute amplitudes of corneal potentials are not directly comparable between subjects due to variations in electrode placement, tissue impedances, or anatomical differences, but relative potential over a range of irradiance provides a qualitative measure of device performance [8]. The corneal waveform could also be modulated by decreasing or increasing the laser pulse duration (data not shown), which can be used as another measure of validating device performance. Corneal monitoring of device activation is an important control measure in clinical testing because it can be non-invasively used as a method to verify device function over the lifetime of the implant.

The optically activated nanowire based prosthesis offers several significant advantages to other retinal prosthetic strategies currently being pursued. The nanowire design allows the integration of photodetection and neural stimulation into each pixel. This allows for individual pixels to be optically addressed, which greatly simplifies the form factor and packaging requirements for a retinal prosthesis and obviates the need for hard wired connections to the pixels of an external camera [104], which is a daunting engineering challenge. It also eliminates the need for a complicated integrated circuit for each pixel as in the case for prosthetics making use of an intraocular CMOS sensor [96]. With the nanowire based prosthesis, a large number of high density electrodes can be placed in a small surgically tractable package. The device tested here covered approximately a 3×4 mm area of retina providing more than 17 degrees of visual field, while containing 1,512

electrodes at 50 μm spacing. This design may offer advantages versus the individually wired 60 electrodes in the Argus II or the 378 optically addressed electrodes in the Pixium PRIMA in terms of electrode density and visual field, and with a simpler electrical component packaging strategy when compared with the Alpha AMS. Although estimation of visual acuity from retinal spacing alone is challenging, it is widely assumed that increasing pixel density will lead to an increase in visual acuity. From sampling theory, a 50 μm pixel pitch roughly corresponds to a best theoretical acuity of approximately 20/400 [26, 74, 98]. This compares favorably with other devices on the market or in clinical testing in terms of array spacing [3, 25, 52, 96]. Taken together the photovoltaic nanowire device described here represents a substantial advance in the field of retinal prosthetics, demonstrating a functional response to light activation of the subretinal implant *in vivo* from recordings of illumination evoked potentials in visual cortex.

5.5 Acknowledgements

Chapter 6

Conclusion and Outlook

This chapter highlights the contributions of this thesis and offers an outlook on ongoing and anticipated future further developments in neural interfaces for next generation retinal prostheses.

6.1 Thesis Contributions and Significance

Chapter 2 offered an in-depth review of engineering principles in the design of neural interfaces for clinical applications. The chapter analyzed trade-offs in noise and energy of electrode arrays and interface circuits across a wide range of spatial scale, temporal resolution, and purpose. Careful understanding of the signal properties, the specific kind of electrodes required for measurement, and the most appropriate circuit architecture needed to amplify and process these signals are critical to faithfully record and make use of these neural signals.

Chapter 3 formulated guiding principles in the design of resonant inductive wireless power transfer links for retinal prostheses, and established the particular design considerations to power an intraocular implant. Because of the unique motion and position of the eye, validation of the power transfer strategy was extended beyond the typical nominal distance. Aside from characterizing the performance across rotational and linear displacements we also evaluated the effect of electromagnetic losses in the biological tissue separating the coils.

Chapter 4 presented the development and validation of a complete integrated system-on-chip for scalable, energy-efficient RF power delivery and waveform control, interfacing with a nanowire photodiode array for subretinal optically addressed electrical stimulation. Scalability is derived from the dual use of the subretinal nano-engineered electrode array as both light sensor and electrical stimulating electrode. Due to this property, only two cables are required to be implanted through the eye to globally control all pixels, greatly simplifying implantation surgery and biocompatible packaging. Several innovations in wireless power, stimulation, and data telemetry circuitry provide substantial power savings over existing state-of-the-art systems. These innovations include duty cycling the transmitter, and externally controlling the unregulated received power to directly stimulate the electrode array. With these innovations, not only are regulator losses eliminated, but also most power-consuming overhead functions are outsourced to the external system where more efficient, larger-area, and off-the-shelf solutions are readily available.

In conjunction with the novel power and stimulation strategies, new communication protocols from the external system to the implant and back have been designed to minimize

131

power consumption and system complexity. Only single bit phase changes must be transmitted from the external system, as the RF envelope already controls stimulation power. Furthermore, as the stimulator directly monitors charge instead of current, single bit messages representing a fixed charge quantity can be transmitted through the load shift keying backtelemetry.

Finally, in Chapter 5, we demonstrated light transduction into an electrical stimulation of a passive, unpowered nanowire photodiode array that evokes a physiological response in the rabbit visual cortex. This demonstration is a substantial advance over our previous *ex vivo* work using actively biased, optically addressed, electrically activated stimulation [42].

6.2 Outlook and Broader Impact

Our experiments demonstrated high energy efficiency of RF power delivery and stimulation waveform control on the electrical testbench, and validated successful *in vivo* operation of an electrically unbiased nanowire photodiode array eliciting illumination evoked potentials in retinal diseased animal subjects. We have also shown in our previous work that we can further boost light sensitivity of the system by providing bias power [42]. While these are substantial contributions constituting encouraging developments towards a fully functional subretinal prosthesis to restore functional vision in blind patients, plans to extend these bench-top results to fully packaged animal experiments, and ultimately human clinical trials, are currently under way.

While the contributions of this dissertation were specifically directed towards development of retinal prostheses, the design principles for highly energy-efficient neural interface circuits and systems apply to a broader range of neuroscience and neuroengineering settings to meet pressing challenges both of fundamental research nature and serving towards clinical translation. Continued developments in electrode materials, interface circuits, and embedded systems for neural interfaces with tailored instrumentation solutions at a range of spatial and temporal scales will drive advances towards future unprecedented medical therapies and neuroscience discoveries.

Bibliography

[1] G. N. Angotzi, F. Boi, A. Lecomte, E. Miele, M. Malerba, S. Zucca, A. Casile, and L. Berdondini. Sinaps: An implantable active pixel sensor cmos-probe for simultaneous large-scale neural recordings. *Biosensors and Bioelectronics*, 126:355–364, 2019.

[2] Ardiem Medical Inc. Photograph of standard spiral nerve cuff electrode with four electrodes arrayed radially around the cuff diameter. `www.ardiemmedical.com/neural-cuff/`.

[3] L. N. Ayton, P. J. Blamey, R. H. Guymer, C. D. Luu, D. A. Nayagam, N. C. Sinclair, M. N. Shivdasani, J. Yeoh, M. F. McCombe, R. J. Briggs, N. L. Opie, D. P. N. Villalobos, Joel, M. Varsamidis, M. A. Petoe, C. D. McCarthy, J. J. Walker, N. Barnes, A. N. Burkitt, C. E. Williams, R. K. Shepherd, and P. J. Allen for the Bionic Vision Australia Research Consortium. First-in-human trial of a novel suprachoroidal retinal prosthesis. *PloS one*, 9(12):e115239, 2014.

[4] I. Bekerman, P. Gottlieb, and M. Vaiman. Variations in eyeball diameters of the healthy adults. *Journal of ophthalmology*, 2014, 2014.

[5] L. Berdondini, A. Bosca, T. Nieus, and A. Maccione. Active pixel sensor multielectrode array for high spatiotemporal resolution. In *Nanotechnology and Neuroscience: Nanoelectronic, Photonic and Mechanical Neuronal Interfacing*, pages 207–238. Springer, 2014.

[6] F. Boi, N. Perentos, A. Lecomte, G. Schwesig, S. Zordan, A. Sirota, L. Berdondini, and G. N. Angotzi. Multi-shanks SiNAPS active pixel sensor CMOSprobe: 1024 simultaneously recording channels for high-density intracortical brain mapping. *bioRxiv*, page 749911, 2019.

[7] D. Boinagrov, X. Lei, G. Goetz, T. I. Kamins, K. Mathieson, L. Galambos, J. S. Harris, and D. Palanker. Photovoltaic pixels for neural stimulation: circuit models and performance. *IEEE transactions on biomedical circuits and systems*, 10(1):85–97, 2015.

[8] B. Bosse, E. Zrenner, and R. Wilke. Standard erg equipment can be used to monitor functionality of retinal implants. In *2011 Annual International Conference of the IEEE Engineering in Medicine and Biology Society*, pages 1089–1092. IEEE, 2011.

[9] S. H. Brewer, D. Wicaksana, J.-P. Maria, A. I. Kingon, and S. Franzen. Investigation of the electrical and optical properties of iridium oxide by reflectance ftir spectroscopy and density functional theory calculations. *Chemical physics*, 313(1-3):25–31, 2005.

[10] A. P. Buccino, M. Kordovan, T. V. Ness, B. Merkt, P. D. Häfliger, M. Fyhn, G. Cauwenberghs, S. Rotter, and G. T. Einevoll. Combining biophysical modeling and deep learning for multielectrode array neuron localization and classification. *Journal of neurophysiology*, 120(3):1212–1232, 2018.

[11] A. P. Buccino, M. Kuchta, K. H. Jæger, T. V. Ness, P. Berthet, K.-A. Mardal, G. Cauwenberghs, and A. Tveito. How does the presence of neural probes affect extracellular potentials? *Journal of neural engineering*, 16(2):026030, 2019.

[12] M. Capogrosso, N. Wenger, S. Raspopovic, P. Musienko, J. Beauparlant, L. B. Luciani, G. Courtine, and S. Micera. A computational model for epidural electrical stimulation of spinal sensorimotor circuits. *Journal of Neuroscience*, 33(49):19326–19340, 2013.

[13] E. Castagnola, L. Maiolo, E. Maggiolini, A. Minotti, M. Marrani, F. Maita, A. Pecora, G. N. Angotzi, A. Ansaldo, M. Boffini, L. Fadiga, G. Fortunato, and D. Ricci. PEDOT-CNT-coated low-impedance, ultra-flexible, and brain-conformable micro-ecog arrays. *IEEE Transactions on Neural Systems and Rehabilitation Engineering*, 23(3):342–350, 2014.

[14] Y. M. Chi, T.-P. Jung, and G. Cauwenberghs. Dry-contact and noncontact biopotential electrodes: Methodological review. *IEEE reviews in biomedical engineering*, 3:106–119, 2010.

[15] Y. M. Chi, C. Maier, and G. Cauwenberghs. Ultra-high input impedance, low noise integrated amplifier for noncontact biopotential sensing. *IEEE Journal on Emerging and selected topics in circuits and systems*, 1(4):526–535, 2011.

[16] A. Y. Chow and V. Y. Chow. Subretinal electrical stimulation of the rabbit retina. *Neuroscience letters*, 225(1):13–16, 1997.

[17] E. Y. Chow, A. L. Chlebowski, and P. P. Irazoqui. A miniature-implantable rf-wireless active glaucoma intraocular pressure monitor. *IEEE Transactions on Biomedical Circuits and Systems*, 4(6):340–349, 2010.

[18] F. Claudi. Pyramidal neuron. `www.scidraw.io`.

[19] ClinicalTrials.gov [Internet]. Bethesda (MD): National Library of Medicine (US). Identifier nct03333954, feasibility study of compensation for blindness with the

prima system in patients with dry age related macular degeneration (prima fs). `https://www.clinicaltrials.gov/ct2/show/NCT03333954`, 2017.

[20] ClinicalTrials.gov [Internet]. Bethesda (MD): National Library of Medicine (US). Identifier nct03629899, retina implant alpha ams in blind patients with retinitis pigmentosa. `https://clinicaltrials.gov/ct2/show/NCT03629899`, 2018.

[21] S. F. Cogan. Neural stimulation and recording electrodes. *Annu. Rev. Biomed. Eng.*, 10:275–309, 2008.

[22] M. J. Cook, T. J. O'Brien, S. F. Berkovic, M. Murphy, A. Morokoff, G. Fabinyi, W. D'Souza, R. Yerra, J. Archer, L. Litewka, S. Hosking, P. Lightfoot, V. Ruedebusch, W. D. Sheffield, D. Snyder, K. Leyde, and D. Himes. Prediction of seizure likelihood with a long-term, implanted seizure advisory system in patients with drug-resistant epilepsy: a first-in-man study. *The Lancet Neurology*, 12(6):563–571, 2013.

[23] Y. Cui and C. M. Lieber. Functional nanoscale electronic devices assembled using silicon nanowire building blocks. *science*, 291(5505):851–853, 2001.

[24] L. da Cruz, J. D. Dorn, M. S. Humayun, G. Dagnelie, J. Handa, P.-O. Barale, J.-A. Sahel, P. E. Stanga, F. Hafezi, A. B. Safran, J. Saltzmann, A. Santos, D. Birch, C. A. Spencer, Rand, E. de Juan, J. L. Duncan, D. Eliott, and R. J. Greenberg. Five-year safety and performance results from the argus ii retinal prosthesis system clinical trial. *Ophthalmology*, 123(10):2248–2254, 2016.

[25] G. Dagnelie, P. Christopher, A. Arditi, L. da Cruz, J. L. Duncan, A. C. Ho, L. C. Olmos de Koo, J.-A. Sahel, P. E. Stanga, G. Thumann, Y. Wang, M. Arsiero, J. D. Dorn, R. J. Greenberg, and the Argus® II Study Group. Performance of real-world functional vision tasks by blind subjects improves after implantation with the argus® ii retinal prosthesis system. *Clinical & experimental ophthalmology*, 45(2):152–159, 2017.

[26] S. Damle, Y.-H. Lo, and W. R. Freeman. High visual acuity retinal prosthesis: understanding limitations and advancements toward functional prosthetic vision, 2017.

[27] T. L. Edwards, C. L. Cottriall, K. Xue, M. P. Simunovic, J. D. Ramsden, E. Zrenner, and R. E. MacLaren. Assessment of the electronic retinal implant alpha ams in restoring vision to blind patients with end-stage retinitis pigmentosa. *Ophthalmology*, 125(3):432–443, 2018.

[28] C. C. Enz and G. C. Temes. Circuit techniques for reducing the effects of op-amp imperfections: Autozeroing, correlated double sampling, and chopper stabilization. *Proceedings of the IEEE*, 84(11):1584–1614, 1996.

[29] C. C. Enz, E. A. Vittoz, and F. Krummenacher. A CMOS chopper amplifier. *IEEE Journal of Solid-State Circuits*, 22(3):335–342, 1987.

[30] H. Faber, D. Besch, K.-U. Bartz-Schmidt, H. Eisenstein, J. Roider, H. Sachs, F. Gekeler, E. Zrenner, and K. Stingl. Restriction of eye motility in patients with retina implant alpha ams. *Acta Ophthalmologica*, 2020.

[31] J. D. Fischer. *The Braincon Platform Software-a Closed-loop Brain-computer Interface Software for Research and Medical Applications*. PhD thesis, University of Freiburg, Germany, 2015.

[32] U. Frey, U. Egert, F. Heer, S. Hafizovic, and A. Hierlemann. Microelectronic system for high-resolution mapping of extracellular electric fields applied to brain slices. *Biosensors and Bioelectronics*, 24(7):2191–2198, 2009.

[33] K. Gekeler, K. U. Bartz-Schmidt, H. Sachs, R. E. MacLaren, K. Stingl, E. Zrenner, and F. Gekeler. Implantation, removal and replacement of subretinal electronic implants for restoration of vision in patients with retinitis pigmentosa. *Current opinion in ophthalmology*, 29(3):239–247, 2018.

[34] G. Goetz and D. Palanker. Electronic approaches to restoration of sight. *Reports on Progress in Physics*, 79(9):096701, 2016.

[35] T. Goto, R. Hatanaka, T. Ogawa, A. Sumiyoshi, J. Riera, and R. Kawashima. An evaluation of the conductivity profile in the somatosensory barrel cortex of Wistar rats. *Journal of neurophysiology*, 104(6):3388–3412, 2010.

[36] V. Goverdovsky, W. von Rosenberg, T. Nakamura, D. Looney, D. J. Sharp, C. Papavassiliou, M. J. Morrell, and D. P. Mandic. Hearables: Multimodal physiological in-ear sensing. *Scientific reports*, 7(1):6948, 2017.

[37] L. E. Grosberg, K. Ganesan, G. A. Goetz, S. S. Madugula, N. Bhaskhar, V. Fan, P. Li, P. Hottowy, W. Dabrowski, A. Sher, and D. Palanker. Activation of ganglion cells and axon bundles using epiretinal electrical stimulation. *Journal of neurophysiology*, 118(3):1457–1471, 2017.

[38] S. Ha, A. Akinin, J. Park, C. Kim, H. Wang, C. Maier, G. Cauwenberghs, and P. P. Mercier. A 16-channel wireless neural interfacing soc with rf-powered energy-replenishing adiabatic stimulation. In *2015 Symposium on VLSI Circuits (VLSI Circuits)*, pages C106–C107. IEEE, 2015.

[39] S. Ha, A. Akinin, J. Park, C. Kim, H. Wang, C. Maier, P. P. Mercier, and G. Cauwenberghs. Silicon-integrated high-density electrocortical interfaces. *Proceedings of the IEEE*, 105(1):11–33, 2016.

[40] S. Ha, A. Akinin, J. Park, C. Kim, H. Wang, C. Maier, P. P. Mercier, and G. Cauwenberghs. Silicon-integrated high-density electrocortical interfaces. *Proceedings of the IEEE*, 105(1):11–33, Jan 2017.

[41] S. Ha, M. L. Khraiche, A. Akinin, Y. Jing, S. Damle, Y. Kuang, S. Bauchner, Y.-H. Lo, W. R. Freeman, G. A. Silva, and G. Cauwenberghs. Towards high-resolution retinal prostheses with direct optical addressing and inductive telemetry. *Journal of Neural Engineering*, 13(5):056008, aug 2016.

[42] S. Ha, M. L. Khraiche, A. Akinin, Y. Jing, S. Damle, Y. Kuang, S. Bauchner, Y.-H. Lo, W. R. Freeman, G. A. Silva, and G. Cauwenberghs. Towards high-resolution retinal prostheses with direct optical addressing and inductive telemetry. *Journal of neural engineering*, 13(5):056008, 2016.

[43] E. Hagen, S. Næss, T. V. Ness, and G. T. Einevoll. Multimodal modeling of neural network activity: Computing LFP, ECoG, EEG, and MEG signals with LFPy 2.0. *Frontiers in neuroinformatics*, 12, 2018.

[44] T. D. Harris. New silicon probes record activity of hundreds of neurons simultaneously. `https://www.hhmi.org/news/new-silicon-probes-record-activity-hundreds-neurons-simultaneously`.

[45] R. R. Harrison and C. Charles. A low-power low-noise cmos amplifier for neural recording applications. *IEEE Journal of solid-state circuits*, 38(6):958–965, 2003.

[46] D. T. Hartong, E. L. Berson, and T. P. Dryja. Retinitis pigmentosa. *The Lancet*, 368(9549):1795–1809, 2006.

[47] A. Hassibi, R. Navid, R. W. Dutton, and T. H. Lee. Comprehensive study of noise processes in electrode electrolyte interfaces. *Journal of applied physics*, 96(2):1074–1082, 2004.

[48] A. Hess-Dunning and D. Tyler. Thin film, high-density peripheral nerve cuffs,.

[49] L. R. Hochberg, D. Bacher, B. Jarosiewicz, N. Y. Masse, J. D. Simeral, J. Vogel, S. Haddadin, J. Liu, S. S. Cash, P. Van Der Smagt, and J. P. Donoghue. Reach and grasp by people with tetraplegia using a neurally controlled robotic arm. *Nature*, 485(7398):372, 2012.

[50] G. R. Holt and C. Koch. Electrical interactions via the extracellular potential near cell bodies. *Journal of computational neuroscience*, 6(2):169–184, 1999.

[51] M. S. Humayun, E. de Juan Jr, and G. Dagnelie. The bionic eye: a quarter century of retinal prosthesis research and development. *Ophthalmology*, 123(10):S89–S97, 2016.

[52] M. S. Humayun, J. D. Dorn, L. Da Cruz, G. Dagnelie, J.-A. Sahel, P. E. Stanga, A. V. Cideciyan, J. L. Duncan, D. Eliott, E. Filley, A. C. Ho, A. Santos, A. B. Safran, A. Arditi, L. V. Del Priore, and R. J. Greenberg for the Argus II Study Group. Interim results from the international trial of second sight's visual prosthesis. *Ophthalmology*, 119(4):779–788, 2012.

[53] B. Jones, M. Kondo, H. Terasaki, Y. Lin, M. McCall, and R. Marc. Retinal remodeling. *Japanese journal of ophthalmology*, 56(4):289–306, 2012.

[54] S. Joshi, C. Kim, and G. Cauwenberghs. A 6.5-$\mu W/MHz$ charge buffer with 7-ff input capacitance in 65-nm cmos for noncontact electropotential sensing. *IEEE Transactions on Circuits and Systems II: Express Briefs*, 63(12):1161–1165, 2016.

[55] J. J. Jun, N. A. Steinmetz, J. H. Siegle, D. J. Denman, M. Bauza, B. Barbarits, A. K. Lee, C. A. Anastassiou, A. Andrei, Ç. Aydın, M. Barbic, T. J. Blanche, V. Bonin, J. Couto, B. Dutta, S. L. Gratiy, D. A. Gutnisky, M. Häusser, B. Karsh, P. Ledochowitsch, C. Mora Lopez, C. Mitelut, S. Musa, M. Okun, M. Pachitariu, J. Putzeys, P. D. Rich, C. Rossant, W.-l. Sun, K. Svoboda, M. Carandini, K. D. Harris, C. Koch, J. O'Keefe, and T. D. Harris. Fully integrated silicon probes for high-density recording of neural activity. *Nature*, 551(7679):232, 2017.

[56] M. L. Khraiche, S. El Emam, A. Akinin, G. Cauwenberghs, W. Freeman, and G. A. Silva. Visual evoked potential characterization of rabbit animal model for retinal prosthesis research. In *2013 35th Annual International Conference of the IEEE Engineering in Medicine and Biology Society (EMBC)*, pages 3539–3542. IEEE, 2013.

[57] C. Kim, S. Ha, J. Park, A. Akinin, P. P. Mercier, and G. Cauwenberghs. A 144mhz integrated resonant regulating rectifier with hybrid pulse modulation. In *2015 Symposium on VLSI Circuits (VLSI Circuits)*, pages C284–C285. IEEE, 2015.

[58] S.-J. Kim, S. C. Manyam, D. J. Warren, and R. A. Normann. Electrophysiological mapping of cat primary auditory cortex with multielectrode arrays. *Annals of biomedical engineering*, 34(2):300–309, 2006.

[59] B. Lee, M. K. Koripalli, Y. Jia, J. Acosta, M. Sendi, Y. Choi, and M. Ghovanloo. An implantable peripheral nerve recording and stimulation system for experiments on freely moving animal subjects. *Scientific reports*, 8(1):6115, 2018.

[60] E. C. Leuthardt, G. Schalk, J. R. Wolpaw, J. G. Ojemann, and D. W. Moran. A brain–computer interface using electrocorticographic signals in humans. *Journal of neural engineering*, 1(2):63, 2004.

[61] Y.-T. Liao, H. Yao, A. Lingley, B. Parviz, and B. P. Otis. A 3-μw cmos glucose sensor for wireless contact-lens tear glucose monitoring. *IEEE Journal of Solid-State Circuits*, 47(1):335–344, 2011.

[62] H. Lindén, E. Hagen, S. Leski, E. Norheim, K. H. Pettersen, and G. T. Einevoll. LFPy: a tool for biophysical simulation of extracellular potentials generated by detailed model neurons. *Frontiers in Neuroinformatics*, 7:41, 2014.

[63] D. Looney, C. Park, P. Kidmose, M. L. Rank, M. Ungstrup, K. Rosenkranz, and D. P. Mandic. An in-the-ear platform for recording electroencephalogram. In *2011*

Annual International Conference of the IEEE Engineering in Medicine and Biology Society, pages 6882–6885, Aug 2011.

[64] H. Lorach, G. Goetz, Y. Mandel, X. Lei, T. I. Kamins, K. Mathieson, P. Huie, R. Dalal, J. S. Harris, and D. Palanker. Performance of photovoltaic arrays in-vivo and characteristics of prosthetic vision in animals with retinal degeneration. *Vision research*, 111:142–148, 2015.

[65] H. Lorach, G. Goetz, R. Smith, X. Lei, Y. Mandel, T. Kamins, K. Mathieson, P. Huie, J. Harris, A. Sher, and D. Palanker. Photovoltaic restoration of sight with high visual acuity. *Nature medicine*, 21(5):476, 2015.

[66] H. Lorach, X. Lei, L. Galambos, T. Kamins, K. Mathieson, R. Dalal, P. Huie, J. Harris, and D. Palanker. Interactions of prosthetic and natural vision in animals with local retinal degeneration. *Investigative ophthalmology & visual science*, 56(12):7444–7450, 2015.

[67] H. Lorach, J. Wang, D. Y. Lee, R. Dalal, P. Huie, and D. Palanker. Retinal safety of near infrared radiation in photovoltaic restoration of sight. *Biomedical optics express*, 7(1):13–21, 2016.

[68] J. Loudin, D. Simanovskii, K. Vijayraghavan, C. Sramek, A. Butterwick, P. Huie, G. McLean, and D. Palanker. Optoelectronic retinal prosthesis: system design and performance. *Journal of neural engineering*, 4(1):S72, 2007.

[69] C. H. Lubba, Y. Le Guen, S. Jarvis, N. S. Jones, S. C. Cork, A. Eftekhar, and S. R. Schultz. PyPNS: Multiscale simulation of a peripheral nerve in python. *Neuroinformatics*, pages 1–19, 2018.

[70] Y. Mandel, G. Goetz, D. Lavinsky, P. Huie, K. Mathieson, L. Wang, T. Kamins, L. Galambos, R. Manivanh, J. Harris, and D. Palanker. Cortical responses elicited by photovoltaic subretinal prostheses exhibit similarities to visually evoked potentials. *Nature communications*, 4(1):1–9, 2013.

[71] K. Mathieson, J. Loudin, G. Goetz, P. Huie, L. Wang, T. I. Kamins, L. Galambos, R. Smith, J. S. Harris, A. Sher, and D. Palanker. Photovoltaic retinal prosthesis with high pixel density. *Nature photonics*, 6(6):391, 2012.

[72] A. L. Mcwhorter. $1/f$ *noise and related surface effects in germanium*. PhD thesis, Massachusetts Institute of Technology, 1955.

[73] C. S. Mestais, G. Charvet, F. Sauter-Starace, M. Foerster, D. Ratel, and A. L. Benabid. Wimagine: Wireless 64-channel ecog recording implant for long term clinical applications. *IEEE transactions on neural systems and rehabilitation engineering*, 23(1):10–21, 2014.

[74] G. K. Moghadam, R. Wilke, G. J. Suaning, N. H. Lovell, and S. Dokos. Quasi-monopolar stimulation: a novel electrode design configuration for performance optimization of a retinal neuroprosthesis. *PloS one*, 8(8), 2013.

[75] E. Musk and Neuralink. An integrated brain-machine interface platform with thousands of channels. *bioRxiv*, 2019.

[76] M. N. Nadig. Development of a silicon retinal implant: cortical evoked potentials following focal stimulation of the rabbit retina with light and electricity. *Clinical neurophysiology*, 110(9):1545–1553, 1999.

[77] K. Nakauchi, T. Fujikado, H. Kanda, T. Morimoto, J. S. Choi, Y. Ikuno, H. Sakaguchi, M. Kamei, M. Ohji, T. Yagi, S. Nishimura, H. Sawai, Y. Fukuda, and Y. Tano. Transretinal electrical stimulation by an intrascleral multichannel electrode array in rabbit eyes. *Graefe's Archive for Clinical and Experimental Ophthalmology*, 243(2):169–174, 2005.

[78] D. A. Nayagam, R. A. Williams, P. J. Allen, M. N. Shivdasani, C. D. Luu, C. M. Salinas-LaRosa, S. Finch, L. N. Ayton, A. L. Saunders, M. McPhedran, C. McGowan, J. Villalobos, J. B. Fallon, A. K. Wise, J. Yeoh, J. Xu, H. Feng, R. Millard, M. McWade, P. C. Thien, C. E. Williams, and R. K. Shepherd. Chronic electrical stimulation with a suprachoroidal retinal prosthesis: a preclinical safety and efficacy study. *PloS one*, 9(5), 2014.

[79] T. V. Ness, C. Chintaluri, J. Potworowski, S. Łęski, H. Głąbska, D. K. Wójcik, and G. T. Einevoll. Modelling and analysis of electrical potentials recorded in microelectrode arrays (MEAs). *Neuroinformatics*, 13(4):403–426, 2015.

[80] A. M. Norcia, L. G. Appelbaum, J. M. Ales, B. R. Cottereau, and B. Rossion. The steady-state visual evoked potential in vision research: a review. *Journal of vision*, 15(6):4–4, 2015.

[81] J. Nuboer and P. Moed. Increment-threshold spectral sensitivity in the rabbit. *Journal of comparative physiology*, 151(3):353–358, 1983.

[82] P. L. Nunez and R. Srinivasan. *Electric fields of the brain: the neurophysics of EEG*. Oxford University Press, USA, 2006.

[83] D. Palanker, A. Vankov, P. Huie, and S. Baccus. Design of a high-resolution optoelectronic retinal prosthesis. *Journal of neural engineering*, 2(1):S105, 2005.

[84] J. Park, C. Kim, A. Akinin, S. Ha, G. Cauwenberghs, and P. P. Mercier. Wireless powering of mm-scale fully-on-chip neural interfaces. In *2017 IEEE Biomedical Circuits and Systems Conference (BioCAS)*, pages 1–4. IEEE, 2017.

[85] J. Park, J. Kim, S.-Y. Kim, W. H. Cheong, J. Jang, Y.-G. Park, K. Na, Y.-T. Kim, J. H. Heo, C. Y. Lee, J. H. Lee, F. Bien, and J.-u. Park. Soft, smart contact lenses with integrations of wireless circuits, glucose sensors, and displays. *Science advances*, 4(1):eaap9841, 2018.

[86] A. Paul, A. Akinin, M. S. Lee, M. Kleffner, S. R. Deiss, and G. Cauwenberghs. Integrated in-ear device for auditory health assessment. In *2019 41st Annual International Conference of the IEEE Engineering in Medicine and Biology Society (EMBC)*, pages 56–59, July 2019.

[87] A. Paul, S. R. Deiss, D. Tourtelotte, M. Kleffner, T. Zhang, and G. Cauwenberghs. Electrode-skin impedance characterization of in-ear electrophysiology accounting for cerumen and electrodermal response. In *2019 9th International IEEE/EMBS Conference on Neural Engineering (NER)*, pages 855–858, March 2019.

[88] Pixium Vision Press Release. Pixium vision announces ce market approval of iris ®ii, its first bionic vision system. `http://www.pixium-vision.com/en/media/press-releases`, 2016.

[89] J. F. Rizzo III, S. Goldbaum, M. Shahin, T. J. Denison, and J. Wyatt. In vivo electrical stimulation of rabbit retina with a microfabricated array: strategies to maximize responses for prospective assessment of stimulus efficacy and biocompatibility. *Restorative neurology and neuroscience*, 22(6):429–443, 2004.

[90] B. Rubehn, C. Bosman, R. Oostenveld, P. Fries, and T. Stieglitz. A mems-based flexible multichannel ecog-electrode array. *Journal of neural engineering*, 6(3):036003, 2009.

[91] R. Sarpeshkar, T. Delbruck, and C. A. Mead. White noise in MOS transistors and resistors. *IEEE Circuits and Devices Magazine*, 9(6):23–29, 1993.

[92] M. Schuettler, F. Kohler, J. S. Ordonez, and T. Stieglitz. Hermetic electronic packaging of an implantable brain-machine-interface with transcutaneous optical data communication. In *2012 Annual International Conference of the IEEE Engineering in Medicine and Biology Society*, pages 3886–3889. IEEE, 2012.

[93] H. A. Shah, S. R. Montezuma, and J. F. Rizzo III. In vivo electrical stimulation of rabbit retina: effect of stimulus duration and electrical field orientation. *Experimental eye research*, 83(2):247–254, 2006.

[94] C. Soci, A. Zhang, X.-Y. Bao, H. Kim, Y. Lo, and D. Wang. Nanowire photodetectors. *Journal of nanoscience and nanotechnology*, 10(3):1430–1449, 2010.

[95] D. Sterratt, B. Graham, A. Gillies, and D. Willshaw. *Principles of computational modelling in neuroscience*. Cambridge University Press, 2011.

[96] K. Stingl, R. Schippert, K. U. Bartz-Schmidt, D. Besch, C. L. Cottriall, T. L. Edwards, F. Gekeler, U. Greppmaier, K. Kiel, A. Koitschev, L. Kühlewein, R. E. MacLaren, R. J. D., J. Roider, A. Rothermel, H. Sachs, G. S. Schröder, J. Tode, N. Troelenbergh, and E. Zrenner. Interim results of a multicenter trial with the new electronic subretinal implant alpha ams in 15 patients blind from inherited retinal degenerations. *Frontiers in neuroscience*, 11:445, 2017.

[97] J. L. Stone, W. E. Barlow, M. S. Humayun, E. de Juan, and A. H. Milam. Morphometric analysis of macular photoreceptors and ganglion cells in retinas with retinitis pigmentosa. *Archives of Ophthalmology*, 110(11):1634–1639, 1992.

[98] H. C. Stronks and G. Dagnelie. The functional performance of the argus ii retinal prosthesis. *Expert review of medical devices*, 11(1):23–30, 2014.

[99] F. T. Sun, M. J. Morrell, and R. E. Wharen. Responsive cortical stimulation for the treatment of epilepsy. *Neurotherapeutics*, 5(1):68–74, 2008.

[100] K. Sun, A. Kargar, N. Park, K. N. Madsen, P. W. Naughton, T. Bright, Y. Jing, and D. Wang. Compound semiconductor nanowire solar cells. *IEEE Journal of Selected Topics in Quantum Electronics*, 17(4):1033–1049, 2011.

[101] E. Tolstosheeva, V. Gordillo-González, V. Biefeld, L. Kempen, S. Mandon, A. Kreiter, and W. Lang. A multi-channel, flex-rigid ecog microelectrode array for visual cortical interfacing. *Sensors*, 15(1):832–854, 2015.

[102] A. van der Ziel. Unified presentation of $1/f$ noise in electron devices: fundamental $1/f$ noise sources. *Proceedings of the IEEE*, 76(3):233–258, 1988.

[103] P. Walter and K. Heimann. Evoked cortical potentials after electrical stimulation of the inner retina in rabbits. *Graefe's archive for clinical and experimental ophthalmology*, 238(4):315–318, 2000.

[104] J. D. Weiland and M. S. Humayun. Retinal prosthesis. *IEEE Transactions on Biomedical Engineering*, 61(5):1412–1424, 2014.

[105] W. L. Wong, X. Su, X. Li, C. M. G. Cheung, R. Klein, C.-Y. Cheng, and T. Y. Wong. Global prevalence of age-related macular degeneration and disease burden projection for 2020 and 2040: a systematic review and meta-analysis. *The Lancet Global Health*, 2(2):e106–e116, 2014.

[106] Xiong Zhou, Qiang Li, S. Kilsgaard, F. Moradi, S. L. Kappel, and P. Kidmose. A wearable ear-EEG recording system based on dry-contact active electrodes. In *2016 IEEE Symposium on VLSI Circuits (VLSI-Circuits)*, pages 1–2, June 2016.

[107] N. Xue, S.-P. Chang, and J.-B. Lee. A su-8-based microfabricated implantable inductively coupled passive rf wireless intraocular pressure sensor. *Journal of Microelectromechanical Systems*, 21(6):1338–1346, 2012.

[108] Y. Yamauchi, L. M. Franco, D. J. Jackson, J. F. Naber, R. O. Ziv, J. F. Rizzo III, H. J. Kaplan, and V. Enzmann. Comparison of electrically evoked cortical potential thresholds generated with subretinal or suprachoroidal placement of a microelectrode array in the rabbit. *Journal of neural engineering*, 2(1):S48, 2005.

[109] Y. Yan, X. Sui, W. Liu, Y. Lu, P. Cao, Z. Ma, Y. Chen, X. Chai, and L. Li. Spatial characteristics of evoked potentials elicited by a mems microelectrode array for suprachoroidal-transretinal stimulation in a rabbit. *Graefe's Archive for Clinical and Experimental Ophthalmology*, 253(9):1515–1528, 2015.